

MANUFACTURE OF FUNCTIONALLY GRADIENT OBJECTS THROUGH WELD-DEPOSITION

SOMASHEKARA M A

A Dissertation Submitted to
Indian Institute of Technology Hyderabad
In Partial Fulfillment of the Requirements for
The Degree of Doctor of Philosophy



भारतीय प्रौद्योगिकी संस्थान हैदराबाद
Indian Institute of Technology Hyderabad

Department of Mechanical and Aerospace Engineering

January, 2016

Declaration

I declare that this written submission represents my ideas in my own words, and where others' ideas or words have been included, I have adequately cited and referenced the original sources. I also declare that I have adhered to all principles of academic honesty and integrity and have not misrepresented or fabricated or falsified any idea/data/fact/source in my submission. I understand that any violation of the above will be a cause for disciplinary action by the Institute and can also evoke penal action from the sources that have thus not been properly cited, or from whom proper permission has not been taken when needed.



(Signature)

Somashekara M A

(Student Name)

ME11P1007

(Roll No)

Approval Sheet

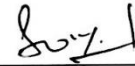
This thesis entitled “**Manufacture of Functionally Gradient objects through Weld-deposition**” by Mr. SOMASHEKARA M A is approved for the degree of Doctor of Philosophy from IIT Hyderabad.



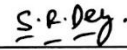
Prof. P. V. Madhusudhan Rao, IIT Delhi
Examiner



Dr. Abhay Sharma, IIT Hyderabad
Internal Examiner



Dr. Suryakumar S., IIT Hyderabad
Adviser



Dr. Suhas Ranjan Dey, IIT Hyderabad
Chairman

Acknowledgements

To visualize is possibly the most significant aspect of an Additive Manufacturing process designer and manufacturer. Most of the built work, design of additive manufacturing process and manufacturing of gradient object artifacts occupy our environment but few stir and shuffle the domains of knowledge in a way so fundamental to cultural reorientation. Without imagination, innovation cannot be nurtured. I would first like to thank my thesis adviser and mentor, **Dr. S. Suryakumar**, who taught me that what is not surrounded by uncertainty, cannot be genuine and true and who encouraged me to take risk in defining my search as I question the preconceptions of an era. Thank you, Prof, for guiding me in a journey so charged with curiosity, and thank you for your consistent insightful input. Your philosophical email has changed my life in many ways, though it's not a part of your job, you do it with concern for me, thank you a lot. There are days when I have left hopes on myself, but you always had confidence in me which drove me to work hard and go on and on.

In the journey of research we often believe that the goal will be reached without any obstacles, but, it's absolutely wrong, before crossing the bridge we need to have constructive criticism from research experts. In the journey of my research, at every stage of my progress seminars the inputs are invaluable from **Dr. Abhay Sharma** and **Dr. Suhas Ranjan Dey**, the Doctoral committee members. Constructive criticism also helped me improve my research knowledge.

I sincerely thanks **Dr. C Viswanath** for helping me in ANSYS APDL coding, one most friendly professor I ever met, thank you Sir.

I also sincerely thank **Dr. Subhradeep Chatterjee** for helping me in characterization part thank you Sir.

With immense pleasure I express my deep and sincere gratitude, regards and thanks to my M.Tech thesis advisor **Dr. Raja Banerjee**, HOD, MAE, for his excellent guidance, invaluable suggestions and continuous encouragement at all stages of my research

work. His wide expertise and logical thinking have been of great value to me. One most coolest and easy professor I ever met, thank you Sir.

My heartfelt thanks to **Prof. Vinayaka Eswaran**, who inspired me a lot in ways more than one during this journey.

The most important aspect of thesis completion is funding and facility, the investigator and author in this research gratefully recognize a financial support from IIT Hyderabad and the department of science and technology (DST). My heartfelt thanks to the Indian Institute of Technology, Hyderabad, which is a research hub nurturing young scientists with commendable infrastructure despite being one of the new IITs, especially the Department of Mechanical and Aerospace engineering. I would like to specially thank the resources that played a vital role in my research life: Manufacturing Lab, Workshop, Digital fabrication lab, CFD lab, Material Science lab and Chemistry lab.

I would like to acknowledge the individuals who helped me in carrying out research throughout my stay, Moulali Syed (Now Scientist C, at BARC), M Naveen Kumar, Yash Agarwal, Avinash Kumar, Mastanaiah M (Scientist E, at DRDO), Raj Kiran, Ramesh, Ramu, Suresh, Jaya Prakash, Yadgiri, Sheshi Ranjan, Mahendra, Basant Kumar, Krishna, Sushil, Harish and Muruges, Dr. Md. Doja (Now in GE).

Let me thank people who supported me in machine installation, experimental setup, spent effort for my work. Firstly, a special thanks to K. Satyanarayana workshop in-charge, who never let my work to be clogged. Thanks a lot Sir. Pages are not enough to write about the remaining people who have done my work but yes I can mention their names. Madhu babu, Bramha charry , Srinivas, Lingam, Kiran, A Praveen, M Praveen , Ashok, Jagadish, Velu murugen, I can't forgot sweepers Nagesh, Nandu , Laxman.

My close friends have been to me like a secret weapon to get through the hard times, with love and with emotional endurance that is rare to find. I am very thankful to my

friends. It would be impossible to name them all, but I would like to specially acknowledge, Hariprasad: your true friendship has earned me the recognition of what is truly important in life. Nice times like representative election, evening chit chat, car drive, weekend movies and those most are because of you. My special thanks to Bhagath Singh (Engineer at BHEL) who is my ex-roomie who taught many things, you inspired me in many ways, and Praneetha (Bhagath wife), special thanks for non-veg food every time I visit your place. Thanks to Seenaiah my roommate who always has a positive attitude and fun filled all the time, his friendship is so memorable. Sasanka Mouli and Vivekananda Study Circle (VCS) member who inspired me a lot in the weekly sessions. A special thanks to Manasa, Ph.D. friends Venkat, Sampath, Damodhar, Sri Harsha, Seenu (chem), Naidu, Syed M, Nilanjan, Jose, Hima sekhar, Vijay, Krishna, Balu and friends from Civil department with whom I always hangout Jaya Prakash, Mahesh, Bhagath, Raja sekhar, Chiranjivi, Sahit, Hanuman.

I also thanks to M.Tech friends Krishna, Goud, Madhav, Santhosh, Jenni, Bhanu, Alok, Raman, Praveen, Siddu, Teja, Sudhakar, Chandra, Nirala, Meena, Minesh, Mohan, Abhishek I can't forget days spent with you all.

Above all I was writing about who helped in professional, but other than that there is much more to tell while in research.

Firstly, I special thanks to the ODF campus, I just love campus like anything, from day one (December 29 2009) to till date, I was always happy to stay in the campus, Room 508 was always so special to me, what not evening bike riding was always awesome, Tuesday and Friday market, eating chats in complex, Amul fast food, Night canteen, Sarath stadium, South gate so on and on. I always dreamt of staying in the permanent campus of IITH which was under construction since my M.Tech. Finally it happened for three months towards the end of tenure, room no 416 C-Block also special to me.

Finally, my parents: I hereby thank my parents, Adinarayanappa M B, Shivamma for their patience and belief in me throughout my studies and I am blessed with such caring

parents. I extend my deepest gratitude, to my loving Sister and brother-in-law Manjula, Shivappa, elder brother's Shiva kumar, Jayachandra, younger brother Shiva Raj Kumar, and uncle and aunt Shivappa and Saraswathamma, cousin brothers and sisters for their invaluable love, affection, encouragement and support. Now, most loved life and lengthy career as a university student is now coming to happy end, and will be missing out many things including not limited, evening chit chat, friends parties, gossips, university elections, teasing's,.



Somashekara M.A

I dedicate this dissertation to my parents, Adinarayanappa M B & Shivamma

Abstract

Functionally Gradient Material (FGM) may have a controlled variation of the material matrix so as to obtain the desired distribution of the properties such as color, density, porosity, hardness, toughness etc. There is a growing interest in FGMs due to their ability to offer high toughness, high strength, machinability, better resistance to corrosion and oxidation effects, and facilitating bonding of metals without severe internal thermal stresses. However, actual realization of FGMs still remains a challenge. Most naturally occurring objects are gradient in nature; examples are bamboo, bone, stone etc. Most man-made objects on the other hand are uniform. This is mainly due to the complexity involved in their design and subsequent manufacturing.

The objects built through Additive Manufacturing techniques are inhomogeneous or non-uniform, i.e., they are inherently anisotropic. When this inherent nature is carefully exploited, the anisotropy transforms into the desired distribution of the properties. Weld-deposition based Additive Manufacturing techniques offer unique advantages on that front due to their ability to control the properties of the deposited matrix by controlling the process parameters like current, layer thickness etc. Preliminary experiments carried out this subject have shown that the hardness of the material is dependent on the weld-deposition current. Hence, online control of the same will help in manufacturing a metal matrix with variable hardness value. The variation possible through this method however will be limited in nature. A wider control of material properties can be obtained with the help of tandem weld-deposition setup like twin-wire. In twin-wire weld-deposition, two filler wires (electrodes) are guided separately and it is possible to control each filler wire individually. The present work focuses on obtaining a wide range of material properties by selecting filler wires with complementary properties and controlling the deposition rate of each of them separately.

The experimental setup of Twin-wire Weld-deposition based Additive Manufacturing (TWAM) are discussed in detail. Working principle of twin-wire weld-deposition process along with the individual attachments viz. welding torch, wire feeder and

power source are also presented. ER70S-6 and ER110S-G are the two filler wires used for the study; the former has lower hardness than the latter.

The range of process parameter for different combinations of these filler wires was determined and the operating range of the same was identified. A second order regression equation for predicting weld bead geometry of width and height as a function of wire speed and torch speed was generated based on a series of experiments and subsequently validated. Subsequently, the criterion for adapting the twin-wire welding from joining to weld-deposition of a complete layer like thermal steady-state condition, effect of torch direction and effect of overlapping beads have also been studied.

Having established the primary process parameters and the secondary operating condition for the TWAM process, various experiments carried out to identify the suitable process parameters at a given location for a desired variation of hardness have been presented. A predictive model for obtaining the wire speed of the filler wires required for a desired value of hardness was also created. The following four sample layers were fabricated to demonstrate the concept of realizing FGMs through TWAM (1) gradient in stepover direction (2) gradient in weld-deposition direction and (3) gradient in both the directions (4) gradient in three dimensions. The latter two as the hardness variation is occurring in every weld-bead, a given weld-bead has to be divided into multiple sub-programs and each sub-program representing the particular set of process parameters has to be called from the robot controller. The fabricated parts showed good match with the desired hardness values for a given location. Furthermore, to demonstrate the possible applications of TWAM, two illustrative examples were fabricated.

Once the methodology for fabrication of FGMs has been established, characterization of objects fabricated through TWAM have been undertaken. Specimen made with five different combinations of filler wires {100:0, 75:25, 50:50, 25:75, 0:100} were used for the analysis. These specimen were examined further by subjecting them to micro hardness, microstructural, X-Ray Fluorescence (XRF), Energy Dispersive X-ray analysis (EDAX) and X-Ray diffraction (XRD) analysis. Further on, the width of the

transition region while switching over from one set of parameters to another was also investigated. That will help in assessing the best possible resolution of the gradient matrix possible.

Modelling of the welding process is felt necessary to understand the evolution of the material properties and to better control the thermal and structural characteristics like residual stresses resulting from the process. With the help of Finite Element Analysis (FEA) and experimental methods, the effect of area filling paths on the residual stresses developed during weld-deposition have been investigated. Three area-filling patterns viz. raster, spiral-in and spiral-out were chosen. FEA for these three patterns was done using ANSYS Mechanical APDL. The twin-wire arc weld-deposition was modeled as a set of two moving heat sources separated at a fixed distance. The deposited material was activated by element birth method once the arc passes over a location, simulating the weld material deposition. The temperature gradient induced residual stresses produced during and post material deposition were predicted using passively coupled thermo-mechanical simulations. For validation, the residual stresses in the weld-deposition specimen were measured using an X-ray diffraction (XRD) system. Temperature distribution plays a critical role in the evolution of the residual stresses during weld-deposition. Hence, two metrics viz., thermal mismatch profile and secant-temperature rate were introduced to quantify preheat and conduction. It was observed that raster patterns had the lowest thermal mismatch and secant-rates resulting in lowest residual stresses of the three area-fill patterns. Residual stresses from experiments are of the same order as those obtained from elastic-FE simulations, however, with a low accuracy of the prediction. Hence, these cannot be directly used for investigating the residual stresses developed. Nevertheless, for comparing the various area-fill patterns, these simulations can provide preliminary insights.

With a combination of (1) process parameter study of twin wire deposition, (2) manufacturing of gradient objects, (3) characterization of gradient layers, (4) modelling of twin wire deposition process, this research attempt tries to establish twin-wire weld-deposition based additive manufacturing as the viable method for the manufacture of functionally gradient materials.

Abbreviations

CAD	Computer-Aided Design
GMAW	Gas Metal Arc Welding
FGMs	Functionally Gradient Materials/Matrix
LENS	Laser Engineered Net-Shaping
LM	Layered Manufacturing
MIG	Metal Inert Gas
MS	Mild Steel
STL	Stereo lithography
AM	Additive Manufacturing
RM	Rapid Manufacturing
RP	Rapid Prototyping
RT	Rapid Tooling
3D	Three Dimensional
DMD	Direct Metal Deposition
SLS	Selective Laser Sintering
LOM	Laminated Objective Manufacturing
TPS	Trans Plus Synergic
CNC	Computer Numerical Control

Contents

Declaration.....	ii
Approval Sheet	ii
Acknowledgements.....	iv
Abstract.....	ix
Abbreviations.....	xii
Contents	xiii
List of figures.....	xvii
List of Tables	xxv
Chapter 1: Introduction	
1.1 Background.....	1
1.2 Classification of Metallic AM Processes.....	2
1.2.1 Laminated manufacturing	3
1.2.2 Powder-bed technologies	3
1.2.3 Deposition processes.....	3
1.2.4 Hybrid processes	4
1.3 Functionally Gradient Materials	4
1.4 Motivation for the Project.....	5
1.5 Problem Definition	7
1.6 Organization of the report.....	8
Chapter 2: Literature Survey	
2.1 Introduction.....	10
2.2 Metallic Additive Manufacturing	10
2.2.1 Laminated Manufacturing.....	11

2.2.2	Powder-bed Technologies.....	14
2.2.3	Deposition Technologies.....	17
2.3	Functionally Gradient Materials (FGM).....	26
2.4	Functionally Gradient Objects through AM.....	29
2.4.1	Laminated Objective Manufacturing (LOM).....	29
2.4.2	Ultrasonic consolidation (UC)	31
2.4.3	Selective Laser Sintering (SLS).....	31
2.4.4	Zcorp’s 3D Printing	33
2.4.5	Laser Engineering Net Shaping (LENS).....	33
2.4.6	Shape Deposition Manufacturing.....	36
2.5	Modeling and process planning of gradient objects	37
2.6	Summary.....	37

Chapter 3: Experimental Setup

3.1	Introduction.....	39
3.2	Twin-wire weld-deposition.....	39
3.3	Position and movement control in robot.....	46
3.4	Robot programming for weld-deposition	49
3.5	Summary.....	52

Chapter 4: Preliminary Study of Parameters Effecting TWAM process

4.1	Introduction.....	53
4.2	Operating range of primary process parameters	53
4.3	Weld bead profile	60
4.4	Effect of deposition conditions on hardness	66
4.4.1	Thermal steady-state conditions.....	67
4.4.2	Effect of torch direction	69
4.4.3	Effect of bead overlap	71

4.4.4	Hardness variation along the cross-section of weld bead	73
4.5	Summary	74

Chapter 5: Manufacture of Functionally Gradient Objects

5.1	Introduction.....	76
5.2	Effect of ratio of filler wires	77
5.2.1	Effect of rate of melting on hardness	79
5.2.2	Effect of filler wire ratio on hardness	81
5.3	Fabrication of gradient layers	84
5.3.1	Gradient in step-over direction	84
5.3.2	Gradient in weld-deposition direction.....	85
5.4	Applications.....	90
5.5	Summary.....	94

Chapter 6: Characterization of Twin-wire Weld-Deposited Objects

6.1	Introduction.....	96
6.2	Experimental analysis for characterization of the specimen	96
6.2.1	Sample preparation	96
6.2.2	Micro hardness analysis	97
6.2.3	Microstructural analysis	99
6.2.4	X-Ray Fluorescence (XRF) analysis.....	100
6.2.5	Energy Dispersive X-ray analysis (EDAX).....	102
6.2.6	X-Ray diffraction (XRD) analysis	103
6.3	Results and Discussions.....	104
6.4	Resolution of the gradient structure.....	106
6.5	Summary.....	108

Chapter 7: FEA Modelling of Twin-wire Weld-Deposition

7.1	Introduction.....	109
-----	-------------------	-----

7.2	Finite Element Analysis of twin-wire weld-deposition	111
7.2.1	Governing equations and boundary conditions.....	111
7.2.2	Modeling of filler material and substrate	115
7.3	Modeling of twin-wire weld-deposition	116
7.4	Validation of FEA Model	121
7.5	Results and discussion	124
7.6	Summary	135
Chapter 8: Conclusion and Future Scope		
8.1	Conclusion	137
8.2	Significant Contributions	140
8.3	Future scope	141
	References.....	142
	Publications based on This Thesis	151

List of figures

Figure 1.1. Additive manufacturing build process.	1
Figure 1.2. Approximate revenues in AM from various industry sectors (Wohlers Associates 2016).	2
Figure 1.3. Methods to achieve functionally gradient matrix by weld-deposition.	6
Figure 2.1. Classification of metallic additive manufacturing methods.	11
Figure 2.2. (a) The CAD model of BMW cowl tool showing conformal cooling.(b) Finished tool cavities (Wimpenny, Bryden, and Pashby 2003).	12
Figure 2.3. Schematic of ultrasonic consolidation (Gibson et al. 2010).	12
Figure 2.4. Fabrication process for a honeycomb assembly using Ultrasonic consolidation (Gibson et al. 2010).	13
Figure 2.5. Selective Laser Sintering process (SLS) (Gibson et al. 2010).	15
Figure 2.6. Principle of Selective Laser Melting (SLM) process. (Hinduja and Li 2013).	15
Figure 2.7. Current applications of SLM (from left: tooling insert with conformal cooling channels, dental restorations (CoCr), hip implant (titanium), pneumatic valve (Hinduja and Li 2013).	16
Figure 2.8. Schematic of an EBM apparatus (Arcam 2015).	16
Figure 2.9. Laser Engineering Net Shaping process (a) Schematic of Lens process, (b) Optomec LENS 750 system (Optomec 2016).	18
Figure 2.10. Manufacturing of parts by using LENS process (a) Processing the blade by using LENS process. (b) H13 tooling and (c) Fixtures produced by LENS process (Sandia National Lab 2016).	18
Figure 2.11. Functional Aerospace Components AeroMet Corporation.	19
Figure 2.12. Laser Aided Manufacturing Processes (LAMP LAB 2016).	20
Figure 2.14. Schematics of Direct Metal Deposition (Mazumder et al. 2000).	20
Figure 2.14. Examples of parts fabricated at NASA Langley using the EBF 3 process (Taminger and Hafley 2006).	21
Figure 2.16. Creation of a layer using SDM (Merz et al. 1994).	22
Figure 2.17. ArcHLM Machine at IIT Bombay (Suryakumar et al. 2011).	23

Figure 2.18. An injection mold manufactured using the 3-axis HLM. (a)CAD models of the part egg template and its injection molds. (b) Near-net molds (c) Finished molds (Suryakumar et al. 2011).	23
Figure 2.18. MPAW process (a) plasma arc (b) Schematic experimental set up (Aiyiti et al. 2006).	24
Figure 2.19. Flowchart of hybrid Plasma Deposition and Milling processes (Xiong, Zhang, and Wang 2009).	25
Figure 2.20. Metal vase manufactured by HPDM. (a) Plasma deposition process scene; (b) milling process scene; (c) metal vase post-processing. (Xiong, Zhang, and Wang 2009)	25
Figure 2.21. Process principle of 3D Welding and Milling (Song et al. 2005; Song, Park, and Chae 2005).	26
Figure 2.22. Various forms of material composition (a) homogeneous (b) coated or joint type (c) FGM (Hopkinson, Hague, and Dickens 2006).	27
Figure 2.23. Example of different requirements of material properties in different locations within a part (Hopkinson, Hague, and Dickens 2006).	27
Figure 2.24. Three ways of material gradient change (a) 1-D gradient (b) 2-D gradient (c) 3-D gradient (Wang and Shang 2009).	28
Figure 2.25. Three representations of laser rapid prototyping material gradient change (a) face gradient (b) line gradient (c) point gradient (Wang and Shang 2009).	28
Figure 2.26. SHS experimental equipment (Yumin Zhang et al. 2001).	30
Figure 2.27. Examples of unidirectional glass fiber /epoxy composite parts built with LOM. The part on the right has been post-cured (Klosterman et al. 1998).	30
Figure 2.28. Cross-sectional photomicrograph of unidirectional fiber glass/epoxy composite, built with LOM. Prepreg layers have staggered 0/90 orientation (Klosterman et al. 1998)	31
Figure 2.29. FGM component produced by UC machine (a) 6 frontal view of an FGM sample made using a UC machine and figure (b) Side view of the FGM sample (Kumar 2010).	31
Figure 2.30. Schematic of an FGM compression test (Chung and Das 2006).	32
Figure 2.31. Schematic description of a compliant gripper and the corresponding FGM component fabricated by SLS.(Chung and Das 2006).	32

Figure 2.32. Rotator cuff scaffold and the corresponding FGM component fabricated by SLS (Haseung and Das 2008; Chung and Das 2006).....	32
Figure 2.33. Schematics of color parts fabricated with ZCorp’s 3D printer (Printers 2015).....	33
Figure 2.34. Cracks observed in the homogeneous deposits: (a) full TiC deposit; (b) Ti 80vol%TiC composite deposit; (c) a schematic showing the originating position of the crack in the composite deposit (Liu and DuPont 2003).....	34
Figure 2.35. LENS samples produced from Ti-6-4 and Inconel 718 powders (Domack and Baughman 2005).....	34
Figure 2.36. Typical appearance of the flat wire welded samples, illustrating: (a) three layers; (b) solidification fronts along the three wires in each layer; and (c) cracking at the base of the Ti-6-4 deposits (Domack and Baughman 2005).	35
Figure 2.37. Schematic diagram showing the formation of porosity during LENS™ processing (Bandyopadhyay et al. 2009).....	35
Figure 2.38. FGM component fabricated by using LENS process (a) sample with total porosity > 50 vol.% are fabricated using tool path based porosity (b) Net shape, functional hip stems with designed porosity fabricated using LENS (Bandyopadhyay et al. 2009).	36
Figure 2.39. Composition of chromo and Nickel versus location for a sharp interface between Invar and 316L stainless steel (Fessler, Nickel, and Link 1997).	37
Figure 3.1. Schematic representation of the metal transfer and welding-current time-curves for Twin-wire (a) & (b) both electrodes in the pulsed electric arc (c) in pulsed/standard (d) in standard/pulsed (Fronius 2016)	40
Figure 3.2. Schematic representation of the metal transfer and welding-current time-curves for single wire (a) pulsed leading power source (b) standard leading power source (c) pulsed trailing power source (d) standard trailing power source (Fronius 2016).....	41
Figure 3.3. Tilt angle of the welding torch	42
Figure 3.4. Stick-out and spacing of the wire electrodes.....	42
Figure 3.5. Complete welding system based on the power source Time Twin Digital 5000.	43
Figure 3.6. Functional principle of Time Twin Digital welding	43

Figure 3.7. Welding torch Robacta Twin Compact.	44
Figure 3.8. VR1500 robot wire feeder.	45
Figure 3.9. (a) Simple drawing of integrated robot and weld set up (b) complete experimental set up of TWAM.	46
Figure 3.10. Robot arm motion in point to point (PTP) mode (Kuka 2016).	47
Figure 3.11. Inline form robot motions (a) point to point (PTP) (b) linear (LIN) (c) Circular (CIRC)	47
Figure 3.12. Robot movement in linear (LIN) motion (Kuka 2016)	48
Figure 3.13. Robot movement in circular (CIRC) motion (Kuka 2016).	48
Figure 3.14. Kuka robot control panel.....	49
Figure 3.15. Schematic representation of weld-deposition of two seams.	50
Figure 3.16. Inline program of seam 1.....	50
Figure 3.17. Inline program of seam 1 and seam 2.....	50
Figure 3.18. Schematic representation of weld path for multi-bead deposition of one layer.	51
Figure 3.19. Various steps in the fabrication of gradient objects	52
Figure 4.1. The representation of the classification of filler wire combinations	54
Figure 4.2. Current vs wire speed graph for 1.2mm Mild Steel	55
Figure 4.3. Some sample weld-bead illustrating the selection of suitable weld beads based on geometry and continuity in bead	59
Figure 4.4. Operating range of current and torch speed of two wires (a) ER70S-6 (b) ER110S-G (c) ER70S-G and ER110S-G for weld-deposition.	59
Figure 4.5. Operating range of current and torch speed of two wires and shaded area is feasible region with any combination of filler.	60
Figure 4.6. Weld bead of boundary points for each of the three combinations of filler wires (a) Representation of boundary points and weld beads path of (b) ER70S-6+ER70S-6 (c) ER110S-G+ER70S-6 (d) ER110S-G+ER110S-6.	61
Figure 4.7. Cross section of a weld-bead used to measuring the profile.	62
Figure 4.8. Predicted vs. measured cross-sectional areas of the weld bead for the three combination of filler wires, (a) ER70S-6+ER70S-6 (b) ER110S-G+ER110S-G and (c) ER110S-G+ER70S-6.....	64

Figure 4.9. Surface plots of weld bead shapes (a)-(b) ER70S-6+ER70S-6 (c)-(d) ER110S-G+ER110S-G (e)-(f) ER110S-G+ ER70S-6.....	66
Figure 4.10. Identifying steady state condition of hardness values (a)-(c) ER70S-6+ER70S-6 (d)-(f) ER110S-G+ER110S-G(g)-(i) ER110S-G+ ER70S-6.....	68
Figure 4.11. Hardness values of deposited weld bead for identification of steady-state condition.	69
Figure 4.12. Schematic representation of weld torch direction and wire speed.	70
Figure 4.13. Weld bead was deposited in the two directions (a)-(c) ER70S-6+ER70S-6 (d)-(f) ER110S-G+ER110S-G(g)-(i) ER110S-G+ ER70S-6.....	70
Figure 4.14. Effect of different torch direction.....	71
Figure 4.15. Weld beads of (a) Two overlap beads (b) Three overlap beads (c) Five overlap beads.	72
Figure 4.16. Effect of hardness on number of beads deposited of filler wire combination (ER110S-G+ER70S-6).	73
Figure 4.17. Hardness variation along cross-section of bead in vertical direction ...	74
Figure 5.1. Representation of parameter setting for achieving gradient in different directions (a) weld direction, X (b) step-over direction, Y.....	77
Figure 5.2. Weld-deposition torch path	78
Figure 5.3. (a) Deposited multi weld beads on MS plate (b) EDM cut weld sample after deposition (c) polished sample for micro-hardness testing.	79
Figure 5.4. Effect on melting rate on the hardness of deposited material. R is the ratio of the wire speeds of the two weld-deposition units.....	80
Figure 5.5. Predicted vs. measured hardness values of combination of ER110S-G+ ER70S-6 filler wires	83
Figure 5.6. Surface plot of hardness for various values of wire speeds	84
Figure 5.7. One dimensional gradient across the step-over direction (a) representation of desired gradient (b) sample prepared with varying wire speed ratios.	85
Figure 5.8. Desired and measured hardness along the step-over direction (Y)	85
Figure 5.9. Gradient in weld-deposition direction (a) representation of desired gradient (b) deposited weld beads (c) polished sample for micro-hardness testing. .	86
Figure 5.10. Desired and measured hardness along the weld-deposition direction (X)	86

Figure 5.11. Two dimensional gradient in both step-over and weld-deposition directions (a) the desired hardness (b) the wire speeds ($v_{ER110S-G}$, $v_{ER70S-6}$) used to obtain the same	87
Figure 5.12. Deposited weld beads of two dimensional gradient.....	88
Figure 5.13. Two dimensional gradient of predicted vs. average measured hardness values for various proportion of wire speeds.....	89
Figure 5.14 Two dimensional layer w.r.t. wire speed.....	90
Figure 5.15 Fabrication of three dimensional gradient object.....	90
Figure 5.16. Component of gradient (a) Schematic representation of two dimensional gradient layer (b) CAD model.	91
Figure 5.17. Deposited gradient part (a) Sample of first layer (b) Finished part.....	92
Figure 5.18. (a) Schematic representation gradient layers for gradient mold; (b) CAD model of punch-cavity pair.	93
Figure 5.19. (a) Layers deposited by 100% ER110S-G, b) layer after milling process	93
Figure 5.20. Finished gradient mold for the punch-cavity pair of a die at two different orientations.	94
Figure 6.1. Specimen preparation (a) weld-deposition (b) cross-sectional cut weld specimen (c) a cut-specimen with polished top surface for hardness measurement.	97
Figure 6.2. Micro-hardness indentations of composition (a) 100% of ER70S-6 (b) 75% of ER70S-6+25% of ER110S-G (c) 50% of ER70S-6+50% of ER110S-G (d) 25% of ER70S-6+75% of ER110S-G (e) 100% of ER110S-G.....	98
Figure 6.3. Hardness variation with respect to filler wire proportion. F1 and F2 are filler wires.....	98
Figure 6.4. Microstructural variation with respect different proportion of filler wire (a) 100% of ER70S-6 (b) 75% of ER70S-6+25% of ER110S-G (c) 50% of ER70S-6+50% of ER110S-G (d) 25% of ER70S-6+75% of ER110S-G (e) 100% of ER110S-G.	100
Figure 6.5. XRF analysis of weld-deposited parts of composition of element (a) Fe (b) Ni (c) Mo (d) Mn (e) Cu (f) Cr (F1 and F2: filler wires ER70S-6 and ER110S-G).	101

Figure 6.6. X-Ray Fluorescence (XRF) spectrum (a) 100% of ER70S-6 (b) 75% of ER70S-6+25% of ER110S-G (c) 50% of ER70S-6+50% of ER110S-G (d) 25% of ER70S-6+75% of ER110S-G (e) 100% of ER110S-G.	102
Figure 6.7. Edax Spectra from a different composition part (a) 100% of ER70S-6 (b) 75% of ER70S-6+25% of ER110S-G (c) 50% of ER70S-6+50% of ER110S-G (d) 25% of ER70S-6+75% of ER110S-G (e) 100% of ER110S-G.....	103
Figure 6.8. XRD phase of different filler wires combinations.	104
Figure 6.9. Deposited sample of switching over from one welding parameter to another of torch direction (a) forward (b) backward.	107
Figure 6.10. Measured hardness variation along the weld-deposition direction with two different weld parameter in forward and backward direction of welding torch.	107
Figure 7.1. Boundary condition for thermal analysis: 1- Heat Source; 2- Convection and Radiation.	112
Figure 7.2. Boundary conditions for structural analysis.....	113
Figure 7.3. Schematic of double ellipsoidal heat source for twin-wire (arc-arc distance = 6mm).....	115
Figure 7.4. Schematic representation of (a) Filler material deposition (b) Geometry of weld and substrate analysed (Nodes 1, 2, 3, 1A, 2A, 3A, 1B, 2B & 3B used in pre-processing).....	116
Figure 7.5. Twin-wire (a) heat density (b) temperature distribution at a given point.	117
Figure 7.6. (a) Thermal material properties; (b) Structural material properties as a function of temperature (Karlsson and Josefson 1990).	118
Figure 7.7. Three types of patterns used in weld-deposition (a) Raster (b) Spiral-in (c) Spiral-out.	118
Figure 7.8. Detailed sequentially coupled thermo-mechanical ANSYS analysis...	119
Figure 7.9. 3D finite element mesh.....	120
Figure 7.10. Fixture dimensions (a) two dimensional drawing (b) substrate fitted in fixture.....	122
Figure 7.11. Setup used for spiral-in deposition pattern (a) Before weld-deposition (b) After weld-deposition: top view (c) After weld-deposition: bottom view.	122

Figure 7.12. X-Ray Diffraction residual stress measurement setup.	123
Figure 7.13. The profile for XRD measurements of residual stress (a) Top side (b) Bottom side of substrate (axial direction: green line; diagonal direction: yellow line)	123
Figure 7.14. Temperature distribution for various area-filling patterns, viz., raster (a)-(c); spiral-in (d)-(f); spiral-out (g)-(i) at different instance of weld-deposition.	125
Figure 7.15. Temperature profile of spiral in pattern (a) Nodal temperature history (2, 2A, 2B); (b) Mismatch temperature between the deposition and the substrate (top (A) and bottom surface (B))	126
Figure 7.16. Average mismatch temperature at the (a) top and (b) bottom of substrate; Secant rate at the (c) top and (d) bottom of substrate.	128
Figure 7.17. Residual stresses for various area-filling patterns, viz., raster (a)-(c); spiral-in (d)-(f); spiral-out (g)-(i) at different instance of weld-deposition.	129
Figure 7.18. Residual stress history at Nodes (2, 2A, & 2B) for (a) Raster; (b) Spiral-in and (c) Spiral-out patterns.	130
Figure 7.19. Residual stress at the end of cooling cycles at selected nodes on (a) The deposition (b) Top of Substrate (c) Bottom of substrate.	131
Figure 7.20. Residual stress from FEA model and experimental on top of substrate along diagonally(line1) and axially(line 2) for the raster (a)-(b); spiral-in (c)-(d); Spiral-out (e)-(f); patterns.....	132
Figure 7.21. Comparison between FEA model and experimental residual stress on bottom of the substrate plate axially and diagonally raster (a) –(b) spiral-in (c)-(d) spiral-out (e)-(f).	134

List of Tables

Table 2.1. Comparison of EBM and SLM (Gibson et al. 2010).	17
Table 4.1. Chemical composition of ER 70S-6 and ER 110S-G filler wires [AWS A5.18 and AWS 5.28].	54
Table 4.2. Values of the parameters used for experiments.	54
Table 4.3 Weld bead suitability for various values of current and torch speed (ER70S-6+ER70S-6).	56
Table 4.4 Weld bead suitability for various values of current and torch speed (ER110S-G+ER110S-G).	57
Table 4.5. Weld bead suitability for various values of current and torch speed (ER110S-G+ER70S-6).	58
Table 4.6. Comparison of predicted and measured cross-sectional areas of the weld bead with twin-wire combination of ER70S-G+ER70S-G for various current and torch speed.	62
Table 4.7. Comparison of predicted and measured cross-sectional areas of the weld bead with twin-wire combination of ER110S-G+ER110S-G for various current and torch speed.	63
Table 4.8. Comparison of predicted and measured cross-sectional areas of the weld bead with twin-wire combination of ER110S-G+ER70S-G for various current and torch speed.	63
Table 4.9. Regression coefficient of area, width and height of weld beads for all combination of fillers.	65
Table 4.10. Hardness values of steady state condition for three combination of two filler wires.	68
Table 4.11. Hardness values of different torch direction.	71
Table 4.12. Hardness values of single and overlap beads.	72
Table 4.13. Hardness variation along cross-section of weld bead in vertical direction.	73
Table 5.1. Process parameters used for experimentation.	78
Table 5.2. Measured hardness values for various combinations of wire speeds while using ER70S-6 in both weld-deposition units.	80

Table 5.3. Measured hardness values for various combinations of wire speeds while using ER110S-G in both weld-deposition units.	81
Table 5.4. Measured hardness values for various combinations of wire speeds while using dissimilar filler wires.	83
Table 5.5. Hardness values in two dimensional gradients for various proportion of wire speed.	88
Table 7.1. Process Parameters used in experiments for validation.	122

Chapter 1

Introduction

1.1 Background

In today's competitive market novel product design and manufacturing are more essential to sustain, in the process it is equally important to reduce cost, increase productivity, and quality, response from the customer or customer satisfaction. To tackle competitive market and accelerate the product manufacturing and development, additive manufacturing (AM) technologies have emerged extensively over the last 20 years. Various methods of additive manufacturing process will be discussed in the literature survey section.

ASTM introduced its abbreviated on Additive Manufacturing (AM) defines it as a process of joining materials to make objects from CAD data, usually layer upon layer, as opposed to subtractive manufacturing methodologies, such as traditional machining. Stereolithography file format (STL) has been a standard method of input to any additive manufacturing machine. STL format contains only surface mesh information and it cannot store color, material variety and other gradient properties. Although, some of AM processes managed to fabricate the color or gradient parameters by controlling the machine settings, mirroring the same in STL was still a bottleneck. Hence, in 2012, ASTM adopted a standard format called Additive Manufacturing Format (AMF) capable of storing color or gradient properties, although the format is still under development (ASTM F2915 2015).

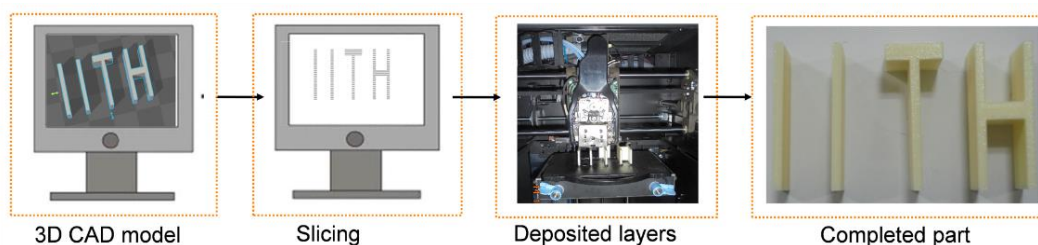


Figure 1.1. Additive manufacturing build process.

Figure 1.1 shows additive manufacturing build process in which the manufacturing of any object begins with the CAD model. The data can be generated in number of ways such as CAD software, reverse engineering, and so on. In the next step, the process planner does the slicing of CAD model and calculates the number of layers required for a given model. This information is sent to the deposition machine to obtain physical part.

Most significant advantage of additive technologies is that the manufacturing process chain of given product/component can be minimized over conventional machining process. Additionally, the process is fully automatic, less human intervention between the processes, hence, accuracy of parts also increases. Today wide variety of applications are using AM process, Figure 1.2 shows a survey conducted by Wohlers associates on the approximate revenue from various segments each in percentage.

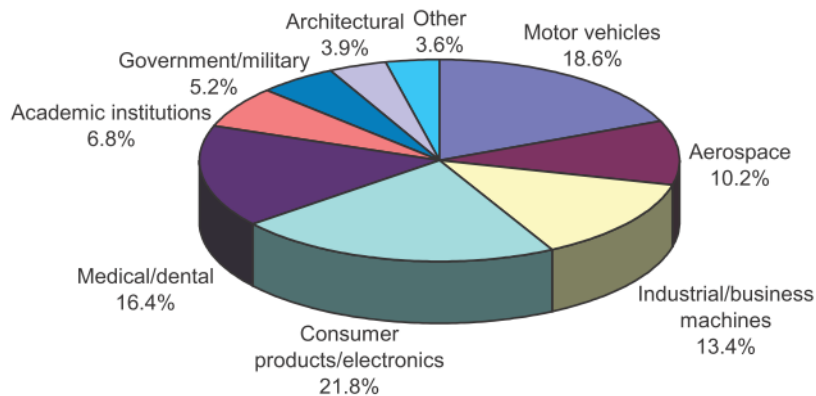


Figure 1.2. Approximate revenues in AM from various industry sectors (Wohlers Associates 2016).

1.2 Classification of Metallic AM Processes

To cater to the vast variations of the manufacturing environment, a number of multi-faceted and hybrid approaches are employed for AM. All these approaches to AM can be grouped into the following four groups of technologies for metallic objects:

1. Laminated manufacturing
2. Powder-bed technologies
3. Deposition technologies
4. Hybrid technologies

1.2.1 Laminated manufacturing

Laminated manufacturing is the simplest additive method. *Laminated Object Manufacturing (LOM)* is the first commercial RP process to produce objects by gluing the suitably profiled paper laminates automatically. LOM deviated from the conventional wisdom of “cut-then-paste” and adopted “paste-then-cut” approach which resulted in an inherent support mechanism and simplified the handling of the laminates. For obvious reasons, only cut-then-paste approach is suitable for laminated tools. As injection moulding, pressure die casting or forging involve liquid or semi-solid material which may ooze into the laminates, tying the laminates is not suitable for these applications. Therefore, there have been many attempts to develop other joining methods such as adhesive bonding, brazing, ultrasonic welding and diffusion bonding. Efforts were also made to minimize the stair step effect through 4-axis machining/laser cutting of the edges of the laminates or finish-machining the assembled dies.

1.2.2 Powder-bed technologies

A powder-bed technology is an AM process in which each layer is realized by first spreading a layer of powder and then joining the particles constituting the desired cross section of the object using a focused tool. Most powder-bed technologies for metallic objects require post-processing in a furnace for removing the binder and/or completing the sintering. Another furnace process for copper-impregnation is required in some processes to close the surface voids. This is essential in dies and moulds to improve the polishability and hardly densifies the object; densification can be achieved through *Hot Iso-static Pressing (HIP)*. The size of the powder particles limits the layer thickness and hence the accuracy.

1.2.3 Deposition processes

In a deposition technology, the layer is woven with the help of a nozzle through which the desired material comes out. The layer weaving will generally have two parts, the boundary profiles and the interiors. FDM is the most popular process of this type for thermoplastics. Subsequently this concept has been extended for building metallic

objects using weld-deposition. Perhaps, “plastic welding” using a coil of filament adopted in FDM was itself inspired from GMA welding. The weld-deposition may be done using laser, electron beam or arc. Ability to build fully dense as well as gradient objects makes the deposition technologies more attractive. The only problem with the deposition technologies is the need for a sacrificial support mechanism required to build overhanging features.

1.2.4 Hybrid processes

A hybrid process is additive process augmented with material removal. Hybrid approach is not new to RP. While LOM used laser to cut the contours of the layers, *Solid Ground Curing (SGC)* and Sander’s ModelMaker-II used milling to achieve vertical accuracy. A hybrid RM process uses laminated manufacturing, powder-bed technology or deposition technology for building the near-net shape and CNC machining to finish it to the required final dimensions. This two-level approach focuses on material integrity during material addition and geometric quality during material subtraction. One may subject the near-net shape to stress relieving or heat treatment as required before finishing.

1.3 Functionally Gradient Materials

They are heterogeneous objects with material composition and microstructure that change in a designed manner in the parts. The concept of FGM was originally proposed to develop materials thermally and mechanically resistant in propulsion systems and for applications like directionally conductive materials. Material distribution allows choosing distribution of properties to achieve the desired features. Thus, it is possible to change properties of the materials.

Since then evolution of this concept in the 1990’s, various works have been done to develop processes for manufacturing of FGMs. However, the majority of FGM parts which are manufactured with these processes are not functional. They are test-parts, with simple morphology and discrete multi-material distribution. These samples are manufactured to study material properties and mechanical or biocompatibility characteristics. As most of the actual applications today assume the fabrication of only

a homogeneous material matrix possible, real case studies in FGMs being used are indeed rare. It is hoped that with the new possibilities being opened by AM, designers will be empowered to contemplate more complex parts with varying properties.

There are many techniques available today to fabricate the functionally gradient material, some of the prominent being vapor deposition, powder metallurgy, centrifugal method in addition to additive manufacturing. Vapor deposition technique is mainly used for very thin surface coatings where microstructure and other properties can change. In powder metallurgy techniques, different forms of powder material are used for achieving gradient objects. Centrifugal techniques, as the name implies, are based on centrifugal force; the material will get dispersed and bulk material will be controlled to form gradient in the object. The above three techniques have limitations in the extent of gradient nature or flexibility of the process as they rely upon manual process planning. Due to its ability to tackle the above limitations, Additive Manufacturing was looked by many researchers as a better alternative to realize gradient structure as it is based on selective addition of material at required location.

Among the AM processes available today FGMs are possible through binder jetting, directed energy deposition, material jetting, powder deposition and sheet lamination. Amongst these, except deposition methods all other methods are either limited to non-metal or provide only unidirectional gradience.

1.4 Motivation for the Project

Based on the energy source used, AM techniques can be classified as those using laser, electron beam or arc. Arc based weld-deposition techniques offer unique advantages over laser and electron beam due to higher deposition rates and material utilization ratio; deposition rate in arc based additive manufacturing reported 50-130g/min for single wire whereas deposition rate in laser and beam is in order of 2-10g/min (Suryakumar et al. 2011). Although the surface finish of arc is inferior to that possible with electron beam or laser, the finish machining operation common to all the three compensates for the loss. Arc based weld-deposition also has the ability to control the

properties of the deposited gradient matrix through the control of process parameters like current, layer thickness, torch orientation, etc. Due to these advantages, arc based weld-deposition has been selected for the present work. Weld-deposition can be automated by attaching the weld-torch to a robot. The current research uses Twin-wire welding for arc deposition and a kuka robot machine to control the position of welding torch.

The following are the various approaches for realizing functionally gradient matrix:

1. Varying process parameters in weld-deposition
2. Controlling the proportion of individual wires in Twin-wire weld process

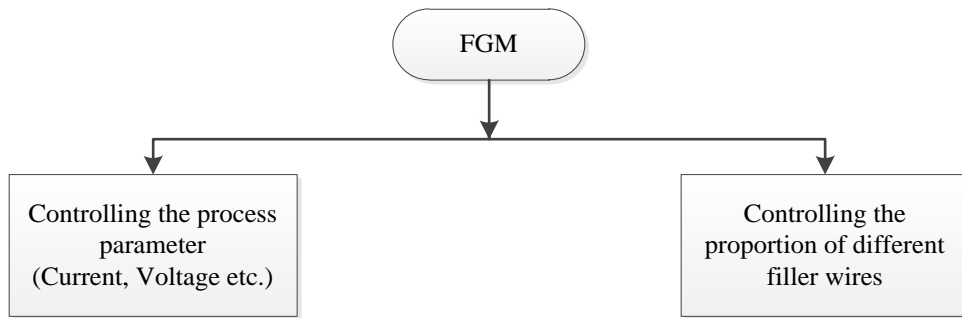


Figure 1.3. Methods to achieve functionally gradient matrix by weld-deposition.

It is possible to build gradient matrix objects by varying parameters like weld-deposition current, voltage, weld direction. The yield and ultimate strength are the two important mechanical properties desired to be controlled. These can be inferred by carrying out tensile tests. Earlier experiments by various researchers studied the influence of current on the tensile properties (Suryakumar et al. 2011) from the study, it is clear that mechanical properties of the object are dependent on the weld-deposition parameters. Hence it is possible to achieve desired mechanical properties at a point through the careful control of the weld-deposition parameters. These studies were done with single welding wire.

A wider control of material properties can be obtained by using two different welding wires. A time-twin weld-deposition setup is quite suitable for the same. A significant advantage of time-twin weld-deposition is that each electrode has a separate contact

tube, the contact tubes are electrically insulated from each other. It is thus possible that the two electrodes have different electrical potentials. Time-twin welding set is used at IIT Hyderabad. Two electrodes, two electric arcs are generated that can be adjusted and improved independent of one another.

1.5 Problem Definition

The aim of this thesis is “to develop a generic Twin-wire Weld-deposition based Additive Manufacturing (TWAM) facility capable of manufacturing functionally gradient materials/objects/components of metals and applications”. This involves:

- 1 Preliminary study of parameters affecting TWAM process
 - i. Finding range of process parameter like welding current, torch speed, stepover increment, for smooth weld bead.
 - ii. Finding effects on weld bead geometry by varying weld process parameters.
 - iii. Finding relation between process parameters with mechanical properties like hardness.

- 2 Manufacture of Functionally Gradient objects through TWAM
 - i. To identify suitable process parameters for desired variation of hardness.
 - ii. Developing a predicted model for manufacturing of gradient object.
 - iii. Fabrication of FGMs through TWAM in step-over direction, weld-deposition direction and thickness direction.
 - iv. Demonstrate applications of TWAM.

- 3 Characterization of Twin-wire weld-deposited objects
 - i. Characterization and examination of the specimens by X-Ray Fluorescence (XRF), Energy Dispersive X-ray analysis (EDAX) and X-Ray diffraction (XRD) analysis.
 - ii. Assessing the best possible resolution of the gradient matrix possible ensuring stability in TWAM process.

4 FEA Modelling of Twin-wire Weld-Deposition

- i. A finite element model was implemented to predict the residual stresses.
- ii. FE analysis was carried out to obtain the temperature distributions.
- iii. Residual stresses measured using X-ray diffraction were compared with those from the FE simulations.

1.6 Organization of the report

The work presented in this dissertation falls into four broad categories: (1) process parameter study of twin-wire deposition, (2) manufacturing of gradient objects, (3) characterization of gradient layers, (4) modelling of twin-wire deposition process.

Chapter 1 an introduction to the work is presented. It starts with emphasizing the Additive Manufacturing process principle, motivation of project, problem definition and organization of report.

Chapter 2 discusses extensive literature survey of various methods of metallic AM, various methods are available to fabricate the gradient objects through AM and comparison of energy sources available.

Chapter 3 presents the experimental set up of TWAM, with details of twin wire process, robot programming, and setup integrating weld-deposition unit, kuka robot.

Chapter 4 discusses studies into weld-deposition process parameters, establishing the range of process parameter that can be varied/acceptable for TWAM process.

Chapter 5 discusses the manufacturing of gradient layers in various combinations and directions. Two demonstrative case studies are also presented.

Chapter 6 discusses the characterization of TWAM samples followed by investigations into the best possible resolution of the gradient matrix that can be obtained in TWAM.

Chapter 7 discusses the FEA modelling of twin-wire weld-deposition and evolution of residual stress for various filling patterns in AM process.

Chapter 8 concludes the work done followed by the future scope of the work.

Chapter 2

Literature Survey

2.1 Introduction

This review section provides an insight into additive manufacturing process and functionally gradient material/objects. The early origins of the additive manufacturing process dating back to 1980's were primarily meant for prototyping applications, it has matured today to the stage of directly producing functional components. Rapid Prototyping, Rapid Manufacturing, Direct Manufacturing, Direct Digital Manufacturing, Additive Digital Manufacturing, Additive Layer Manufacturing, Freeform Fabrication, Solid Freeform Fabrication, Desktop Manufacturing, 3D printing are few names of this approach, which also signify the various phases of development of the process. While the early stages of AM focused only on polymers, the demands from the industry led to the development of processes capable of handling metallic, ceramic and gradient materials. There are many engineering, biomedical etc. applications which require gradient or multiple materials opening potential research frontiers for the research community that will be discussed in the subsequent sections.

2.2 Metallic Additive Manufacturing

Various energy sources are available for sintering and/or depositing the material in additive manufacturing for metallic objects. These can be mainly categorized as laser based, electron beam based and arc based (discussed in the subsequent section). While laser and electron beam offer better surface finish, it is possible to achieve high deposition rates in arc based weld-deposition. The inferior surface finish of arc can be compensated by going for a hybrid system, combining deposition and machining. Due to these reasons, hybrid approaches have evolved as attractive methodology: creation of near-net shape with weld-deposition and using machining to obtain the final geometry.

Spencer et al. developed a process named three-dimensional welding for creating metallic components using GMAW (Gas Metal Arc Welding) process (Spencer, Dickens, and Wykes 1998). Subsequently, many researchers have combined the weld-deposition with machining to overcome the problems of accuracy of subsequent layers and oxide layer formation on top of weld-deposition (Song and Park 2006). Karunakaran et al., integrated CNC and weld-deposition to create the near-net shape (using weld-deposition) and final component (using machining) in the same station (Akula and Karunakaran 2006; K. P. Karunakaran et al. 2010; Suryakumar et al. 2011). These earlier studies on process planning, operating parameters, accuracy, surface finishing etc., helped in establishing the use of weld-deposition as a viable means of creating homogenous metallic components. However, the potential of weld-deposition to also vary the material properties and create functionally gradient materials was not probed.

Based on material deposition method, additive manufacturing for metallic object can also be classified into Laminated Manufacturing, Powder bed technology and deposition technologies as shown in Figure 2.1.

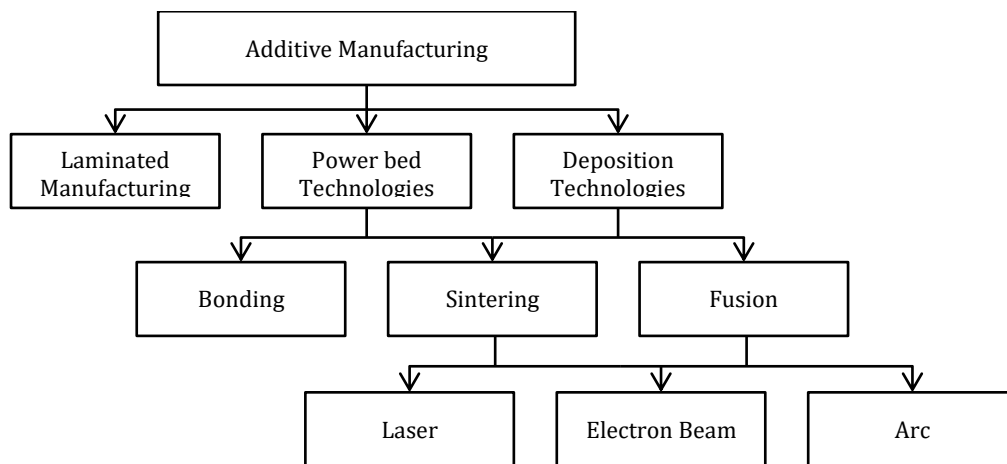


Figure 2.1. Classification of metallic additive manufacturing methods.

2.2.1 Laminated Manufacturing

Laminated manufacturing also known solid laminated process, is one of the early technologies in the additive manufacturing process. This process uses paper sheet or metal foils in continuous rolls as raw material and a laser as a profile cutting tool. In

this method, Nakagawa et al. fabricated tools using sheet metal. Later Wimpenny et al. also developed various forms of rapid tooling; Figure 2.2 shows some such cavities fabricated through rapid tooling (Wimpenny, Bryden, and Pashby 2003; Nakagawa 2000).

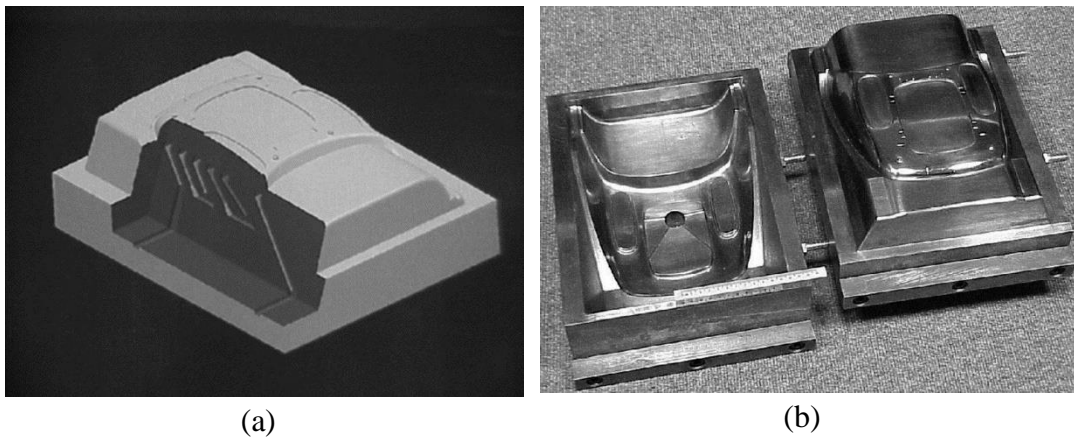


Figure 2.2. (a) The CAD model of BMW cowl tool showing conformal cooling.(b) Finished tool cavities (Wimpenny, Bryden, and Pashby 2003).

Ultrasonic Consolidation, This process, originally developed and later commercialized by Solidica Inc USA in 2000 is also known as Ultrasonic Additive Manufacturing (UAM). UC involves sequential ultrasonic welding of metal foils. It uses a rotating cylindrical sonotrode to join two layers of metal foil (Figure 2.3). It employs applied pressure and ultrasonic vibrations to create friction between two layers, thus resulting in a solid-state weld between the foils.

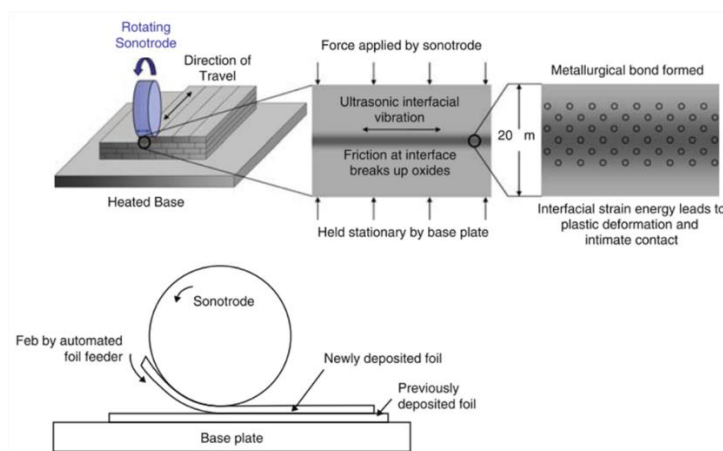


Figure 2.3. Schematic of ultrasonic consolidation (Gibson et al. 2010).

This occurs due to the unique feature in ultrasonic processing wherein a high level of the plastic flow of metal is obtained at low temperatures and pressures. Figure 2.4 (a–f) illustrates the steps utilized to fabricate a honeycomb object by using this process.

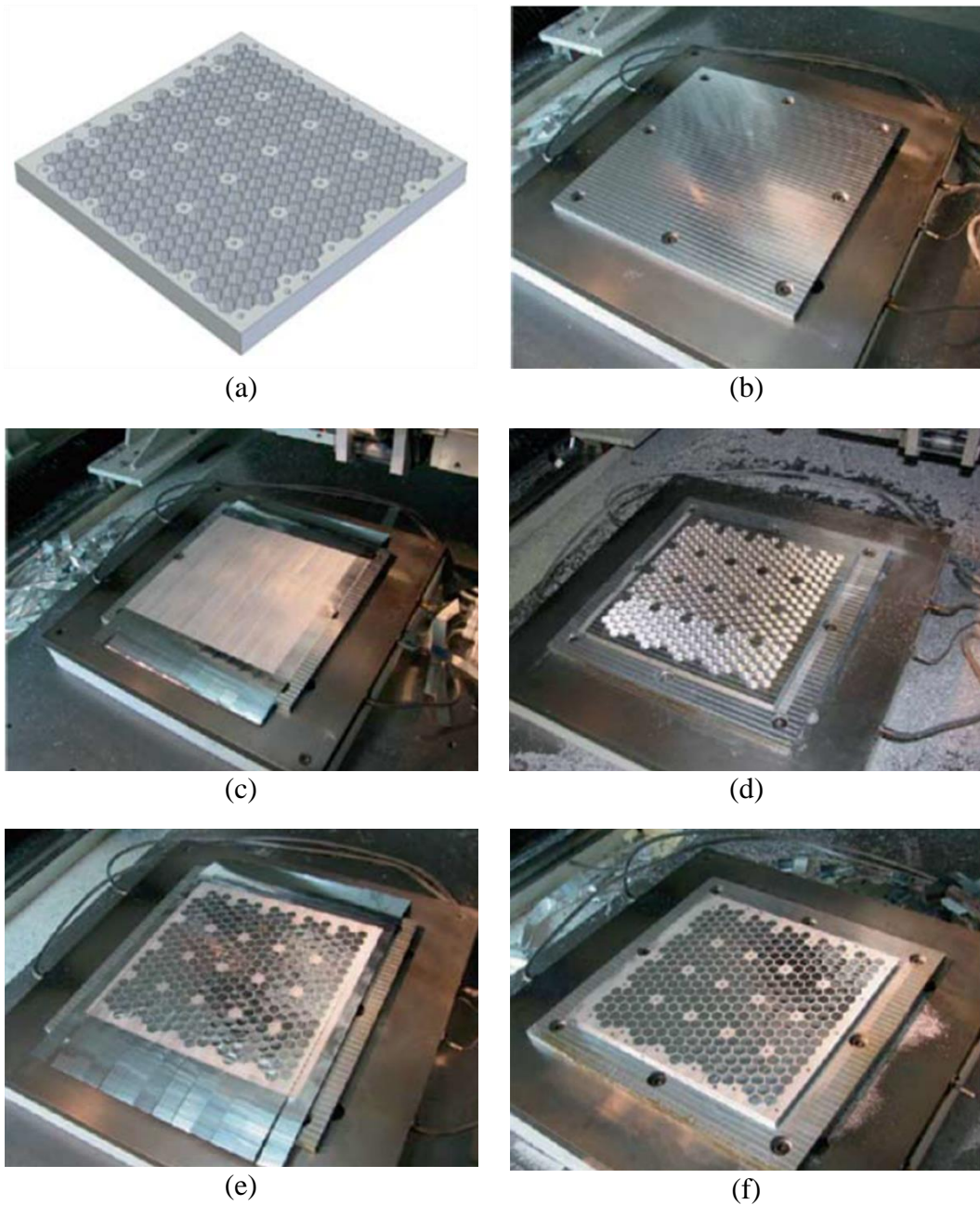


Figure 2.4. Fabrication process for a honeycomb assembly using Ultrasonic consolidation (Gibson et al. 2010).

2.2.2 Powder-bed Technologies

Powder-bed technologies generally use fine powders of sizes approximately ranging from 5-50 μm , in a layer by layer manner to build object while sintering/melting each layer with power source such as laser or electron beam. Figure 2.5 shows one such method in which the setup comprises of a powder spreader, a build platform, and a power source. The powder spreader spreads a thin layer of powder on the build platform, power source traces the region to build the layer. Once a layer is completed, build platform moves downward by the thickness of each layer. This process is repeated for the rest of the component. There are four common approaches of powder bed fusion processes in the creation of complex metal components: full melting, liquid-phase sintering, indirect processing, and pattern methods. The following are some of the powder bed methods based on laser, electron beam and binder as the agent for forming the metal powder.

Selective Laser Sintering, developed at the University of Texas at Austin, USA, was the first commercialized powder bed fusion process. A counter-rotating powder leveling roller fuses thin layers of powder which is spread across the build area. To minimize the oxidation and degradation of powdered material, the enclosed chamber filled with nitrogen gas is used for part building process. The powder in the build platform is maintained at an elevated temperature just below the melting point and/or glass transition temperature of the powdered material. Elevated temperature around the part being formed is maintained by placing infrared heaters above the build platform and above the feed cartridges to pre-heat the powder prior to spreading over the build area. After the powder is spread across the bed and pre-heated, a laser beam is focused onto the powder bed fusing the material thermally and thus creating a new layer. The un-melted powder, acts as a support material for the subsequent layers eliminating the need of secondary support material.

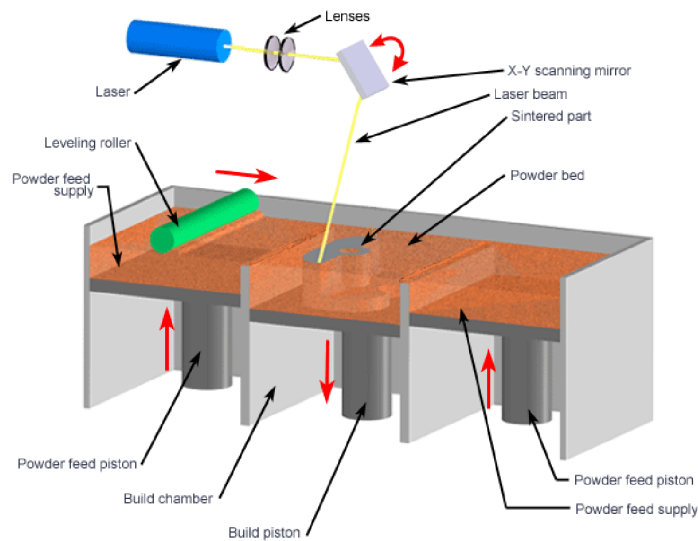


Figure 2.5. Selective Laser Sintering process (SLS) (Gibson et al. 2010).

Selective Laser Melting (SLM), Selective laser sintering discussed in the previous section uses low laser power which results in partial melting during laser scanning creating parts with relatively low strength. Selective laser melting (SLM) process on the other hand melts the powder creating stronger parts. The SLM process is very similar to SLS with the exception of usage of a high power laser to achieve complete melting of powder. Figure 2.6 illustrates the principle of the process and Figure 2.7 shows some of the fabricated parts.

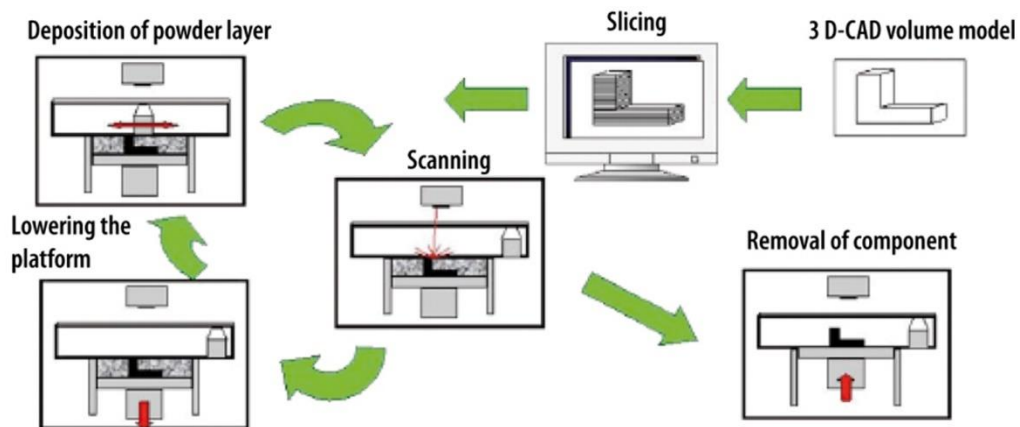


Figure 2.6. Principle of Selective Laser Melting (SLM) process (Hinduja and Li 2013).

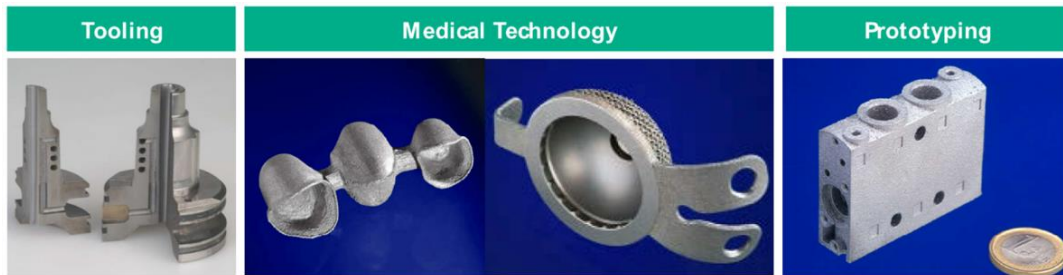


Figure 2.7. Current applications of SLM (from left: tooling insert with conformal cooling channels, dental restorations (CoCr), hip implant (titanium), pneumatic valve (Hinduja and Li 2013).

Electron Beam Melting (EBM), is another approach in powder bed technology which uses a high-energy beam to induce fusion between metal powder particles. This technology was developed at Chalmers University of Technology, Sweden. Table 2.1 shows the comparison of electron beam and SLM process.

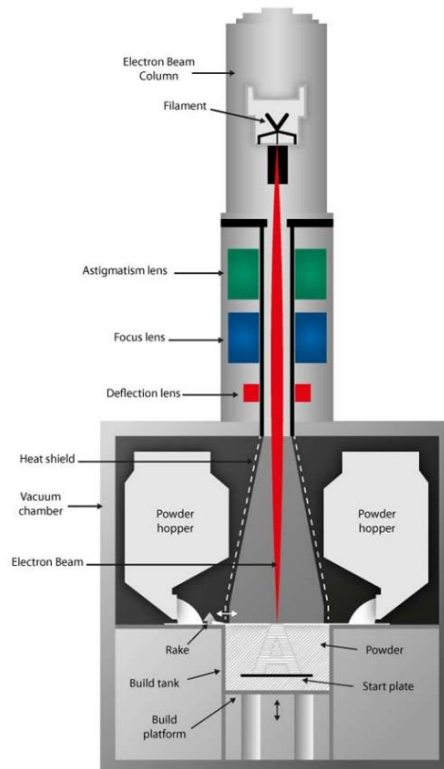


Figure 2.8. Schematic of an EBM apparatus (Arcam 2015).

Characteristic	Electron beam melting	Selective laser melting
Thermal source	Electron beam	Laser
Atmosphere	Vacuum	Inert gas
Scanning	Deflection coils	Galvanometers
Energy absorption	Conductivity-limited	Absorptivity-limited
Powder pre-heating	Use electron beam	Use infrared heaters
Scan speeds	Very fast, magnetically-driven	Limited by galvanometer inertia
Energy costs	Moderate	High
Surface finish	Moderate to poor	Excellent to moderate
Features resolution	Moderate	Excellent
Materials	Metals(conductors)	Polymers, metals and ceramics

2.2.3 Deposition Technologies

Deposition technology works on the principle of a partially or fully melted material from a design head dropping/splashing to the bed through nozzle, as it is solidified to form a three dimensional object. Like the powder-bed, in this case too, the energy can be supplied through use of laser, EB or arc.

Laser Engineered Net Shaping (LENS), was introduced by Sandia National Laboratories, USA, and marketed by Optomec Design Company, USA. In 1997, Optomec's launched "LENS 750" the commercial version of the process. Figure 2.9 shows the LENS process in which material is enclosed in an inert gas chamber. A number of materials with various combinations of laser type and at various atmospheric conditions can be effectively processed making LENS machines highly flexible platforms for beam deposition. Bandyopadhyaya et al. have applied LENS to manufacture porous and functionally graded structures for load bearing implants which will be elaborated in the upcoming sections (Bandyopadhyay et al. 2009). Various researches fabricated the metal parts by LENS process using different materials of stainless steel alloys, tool steel alloys, gradient materials and also was used for repairing the metal parts. Figure 2.10 (a) shows the processing blade, Figure

2.10 (b) shows complete set of fixtures (fixtures) and Figure 2.10 (c) shows tool for injection molding.

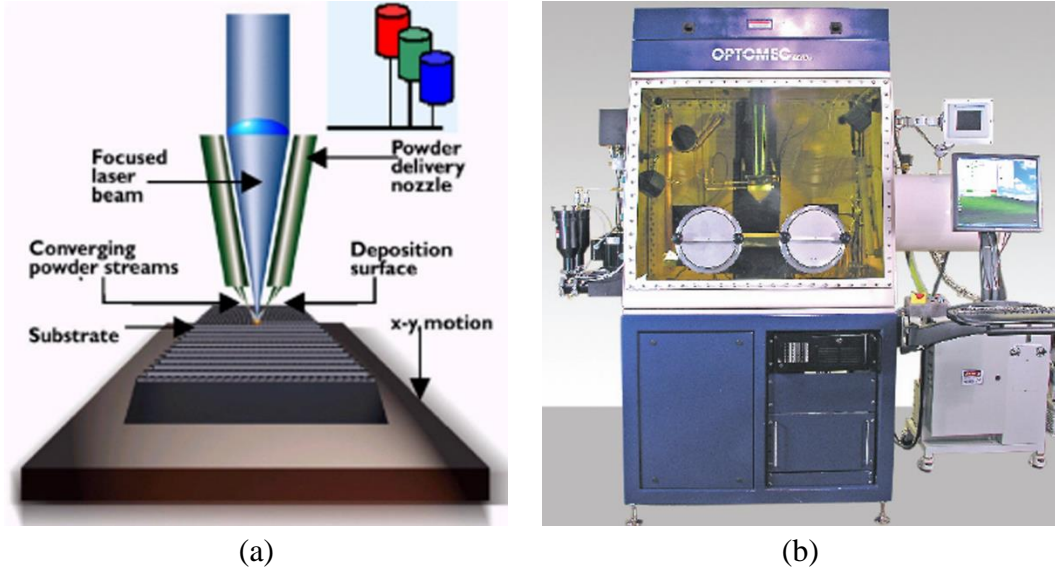


Figure 2.9. Laser Engineering Net Shaping process (a) Schematic of LENS process, (b) Optomec LENS 750 system (Optomec 2016).

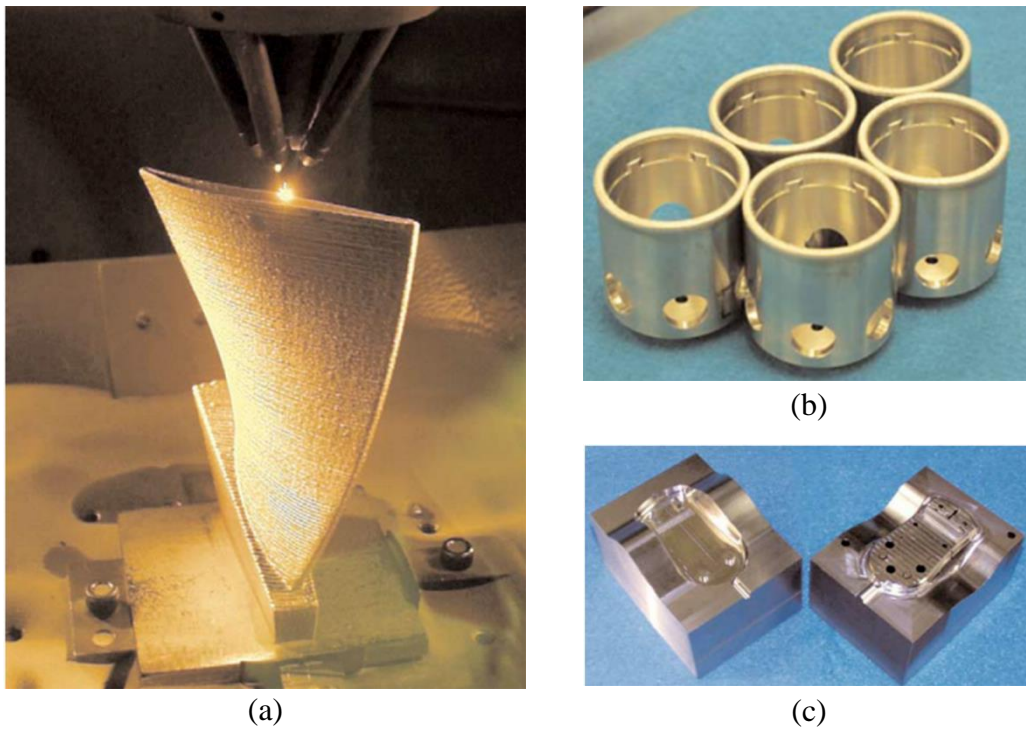


Figure 2.10. Manufacturing of parts by using LENS process (a) Processing the blade by using LENS process. (b) H13 tooling and (c) Fixtures produced by LENS process (Sandia National Lab 2016).

Laser Augmented Manufacturing (LAM), was introduced by Aeromet, USA, for building Ti components for Boeing (kobryn et al. 2002). A 18kW laser with 2.5 axis machine is used for deposition of near-net shape, which is later stress relieved and heat treated and finished using 5 axis CNC machine. Figure 2.11 (b) & (c) shows some of the components fabricated using the same.

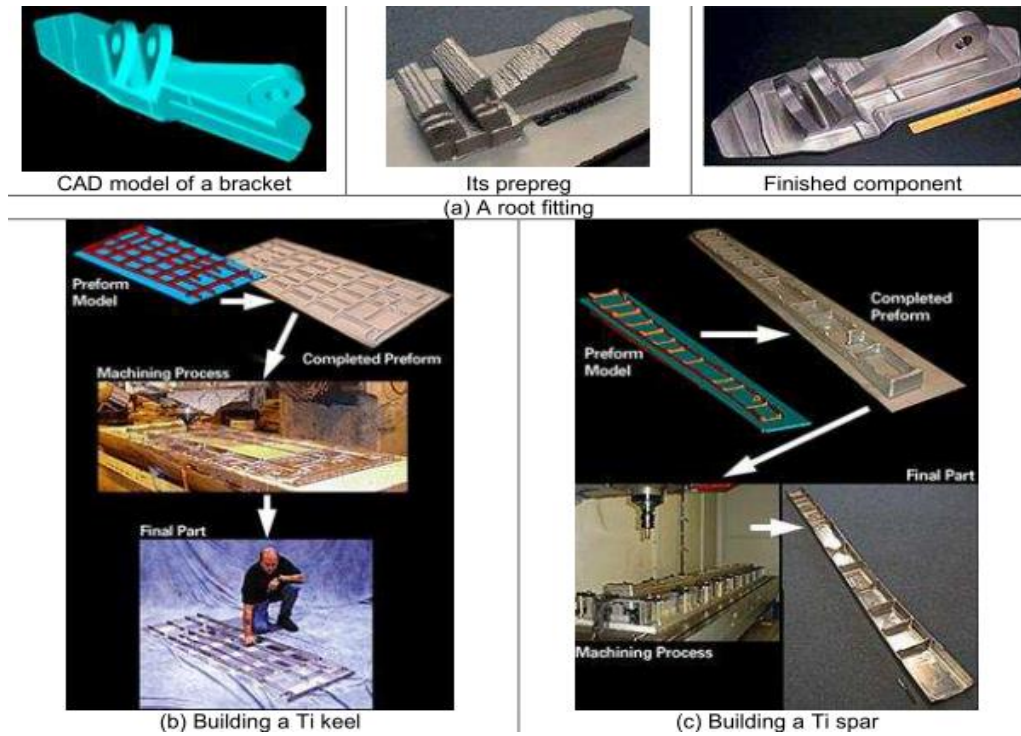


Figure 2.11. Functional Aerospace Components AeroMet Corporation.

Laser Aided Manufacturing Process (LAMP), LAMP process was developed at University of Missouri-Rolla. LAMP is hybrid process which combines laser deposition and machining processes. It has multi-axis which is used during fabrication to minimize the support structure. The optimization of weld parameters was done by monitoring the deposition process using a closed loop controller (Figure 2.12).

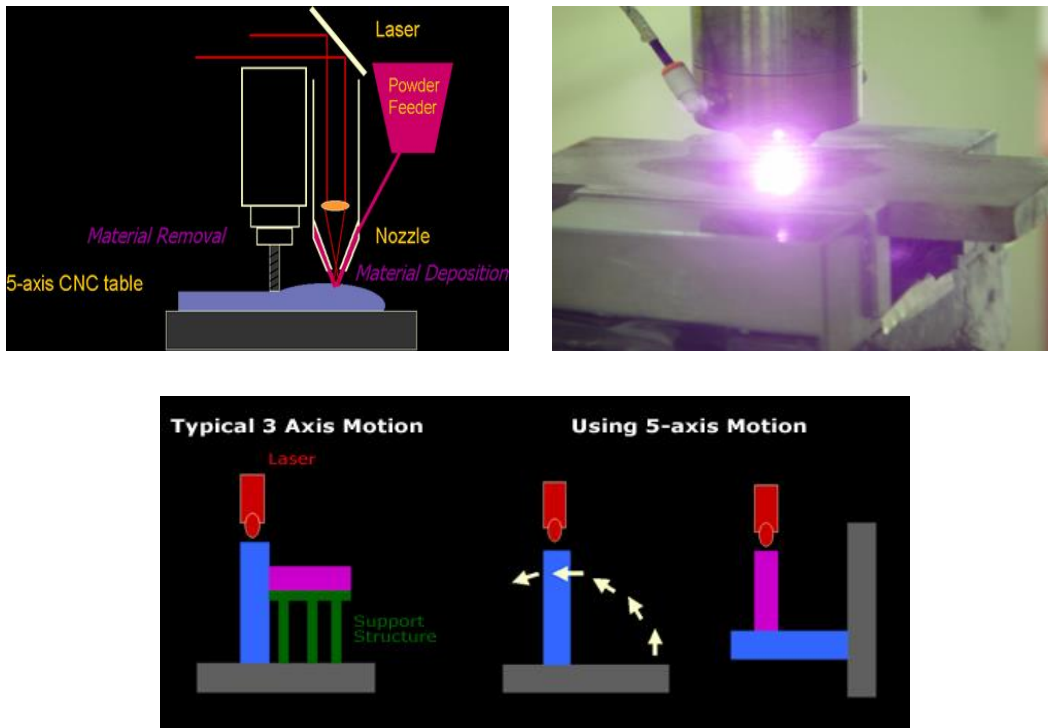


Figure 2.12. Laser Aided Manufacturing Processes (LAMP LAB 2016).

Direct Metal Deposition (DMD), Developed at University of Michigan, comprises of co-axial powder feed and a machine with 5 axes and a closed loop control for controlling the deposition velocity, powder flow rate and laser power. The complete setup is shown in Figure 2.13.

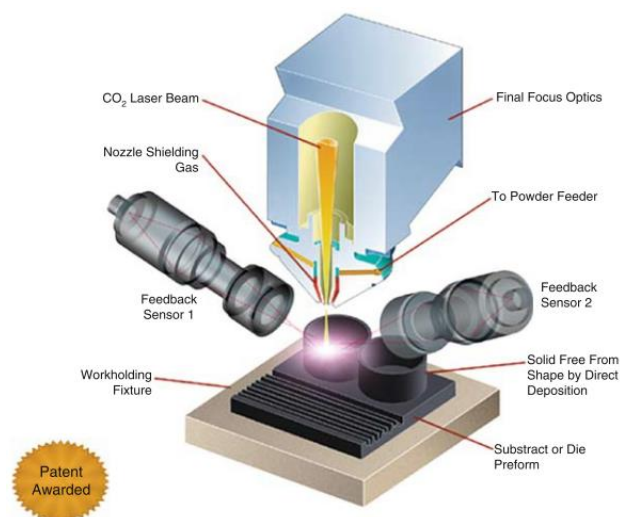


Figure 2.13. Schematics of Direct Metal Deposition (Mazumder et al. 2000).

Electron Beam Freeform Fabrication (EBF³), was developed at NASA Langley Research Centre. This process pushed a metal wire into a molten pool while using electron beam as a power source to fabricate metal parts. Figure 2.14 shows some of the components fabricated by this process (Taminger and Hafley 2006).

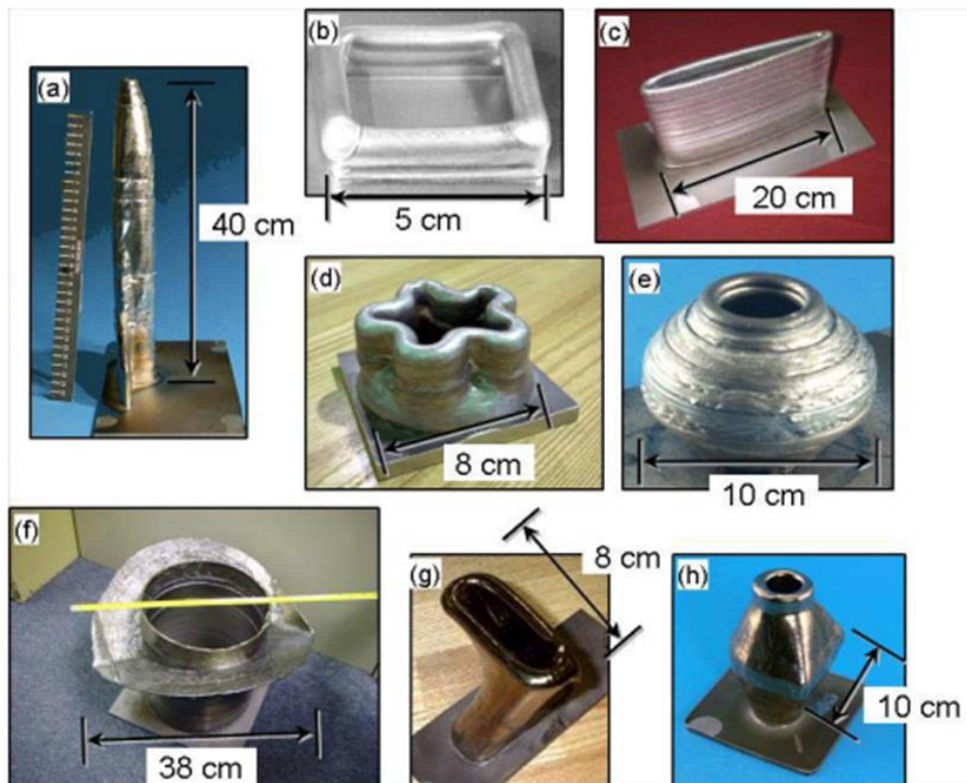


Figure 2.14. Examples of parts fabricated at NASA Langley using the EBF 3 process (Taminger and Hafley 2006).

Shape Deposition Manufacturing (SDM), is an arc based deposition process which makes use of deposition and milling (Merz et al. 1994). It uses a pair of materials, one for model and the other for support. Copper is used as the support material for steel models. Unlike the uniform slicing used in 3D welding, it uses very thick segments. These segments are obtained by splitting the object wherever its normal just becomes horizontal. In any slice, all regions of the slice where the normals are downward, support is required. This near-net shape is then finished for the deposition of the model material. Thus each slice is built by deposition and machining of support and model materials alternately until the entire slab of the slice is complete. Figure 2.15 shows the stages of the process.

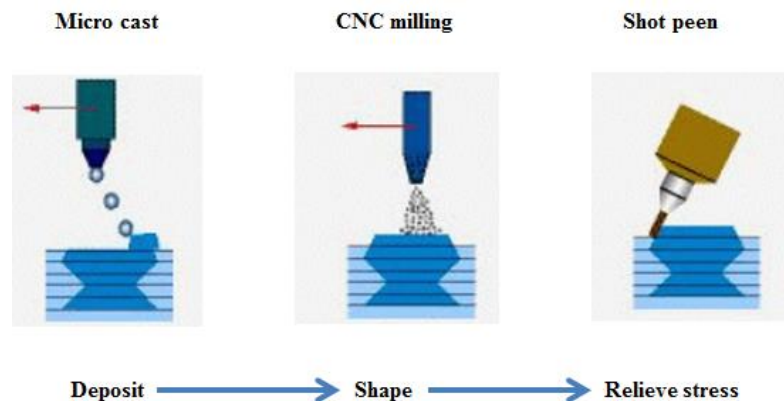


Figure 2.15. Creation of a layer using SDM (Merz et al. 1994).

Hybrid Layer Manufacturing (HLM), welding can be used to produce near-net shapes fast by depositing metal in layers. This near-net shape can be machined fast to obtain the desired geometric quality. Research groups at Nottingham University, Stanford University, Southern Methodist University, Fraunhofer Institute of Production Technology, Aachen, Korea Institute of Science and Technology, Indian Institute of Technology Bombay etc. are developing metallic AM processes using this principle (Spencer, Dickens, and Wykes 1998; Merz et al. 1994; K. P. Karunakaran et al. 2012). They are at different levels of success and some are more focused on specific applications. Some of them make use of laser welding and some prefer arc welding. Electron beam welding also has been used for deposition. While the researchers using arc welding prefer the raw material in wire form, the laser-based processes favour powder form. Gas Metal Arc Welding (GMAW), Gas Tungsten Arc Welding (GTAW) and Plasma Arc Welding (PAW) are the popular arc welding processes used for this application.

A hybrid Rapid Manufacturing process using arc welding developed at IIT Bombay is called Arc Hybrid Layered Manufacturing (ArcHLM). A significant advantage of ArcHLM is its availability as a retrofitment to any existing CNC machine. Figure 2.16 shows a 3-axis arc HLM machine by integrating a 3-axis CNC machine and a Fronius TPS 4000 pulsed synergic MIG welding equipment. The integration was achieved through the relay responsible for the coolant function of the CNC machine.

In other words, M08/M09 in the NC program does welding on/off in arcHLM (K. Karunakaran et al. 2009).

Figure 2.17 shows an injection mold built using ArcHLM. The near-net shapes of these monolithic injection molds were made by alternately weld-depositing a layer and face milling (Suryakumar et al. 2011). The arcHLM approach for this case study of an egg-template was cheaper by 22.3% and faster by 37.5% over the traditional CNC approach (K. Karunakaran et al. 2009).



Figure 2.16. ArcHLM Machine at IIT Bombay (Suryakumar et al. 2011).

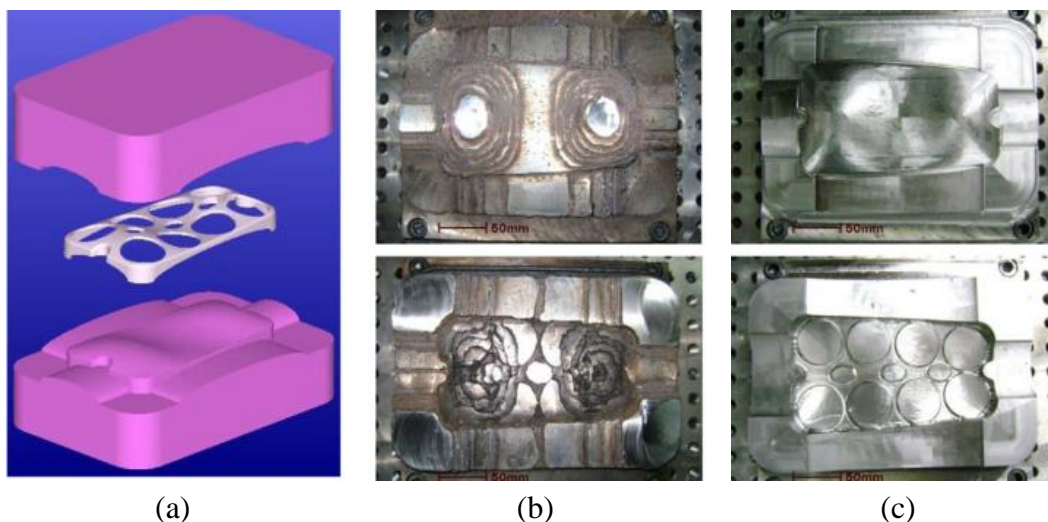


Figure 2.17. An injection mold manufactured using the 3-axis HLM, (a) CAD models of the part egg template and its injection molds, (b) near-net molds, (c) finished molds (Suryakumar et al. 2011).

Micro-Plasma Arc Welding (MPAW), in this process a substrate is fixed on the base plate of the worktable as shown in Figure 2.18 (a) and plasma arc melts the substrate and produces a molten pool, simultaneously filler wire is fed into the molten pool smoothly. As the worktable moves away from the arc, the molten material is solidified and forms the fully dense metallic component. Figure 2.18 (b) illustrates the experimental RP system is a 3.5-axis CNC system composed of a power source (micro plasma-welding machine), a PC-control subsystem, a worktable, an adaptive wire feeding subsystem and a follow-up water-cooled subsystem (Aiyiti et al. 2006).

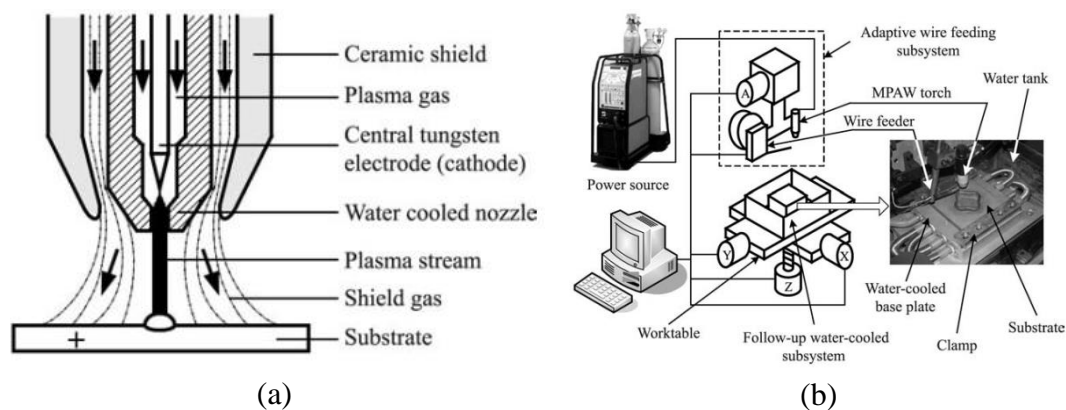


Figure 2.18. MPAW process (a) plasma arc (b) schematic experimental set up (Aiyiti et al. 2006).

Plasma Deposition and Milling (HPDM), this process uses plasma deposition for additive and conventional milling for subtractive phases, which synthesizes the advantages of both processes to fabricate parts. Simultaneously, the precision of the manufactured parts is ensured by the compounding CNC process which assists to remove the staircase caused by the layered manufacturing principle and the allowance of the near-net shape deposited by plasma deposition, the procedural steps are shown in Figure 2.19. Xiong 2009 et al. studied dimensional accuracy as well as the surface quality of the metallic parts and tools manufactured using this process. Figure 2.20 shows a metal vase manufactured by HPDM process (Xiong, Zhang, and Wang 2009).

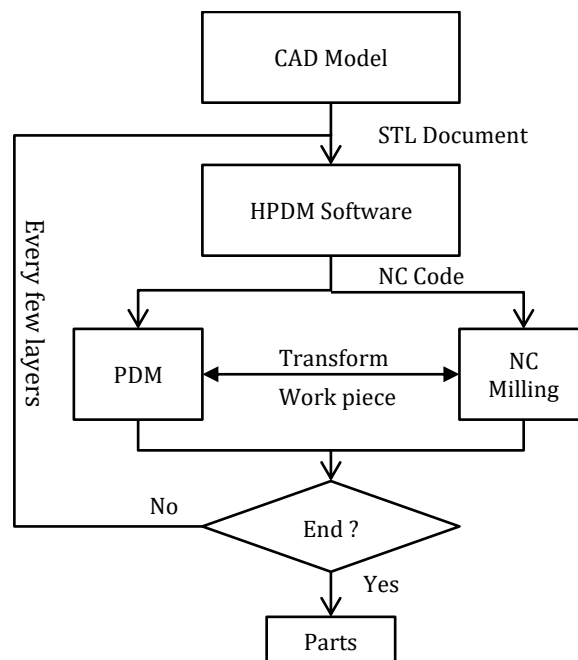


Figure 2.19. Flowchart of hybrid Plasma Deposition and Milling processes (Xiong, Zhang, and Wang 2009).

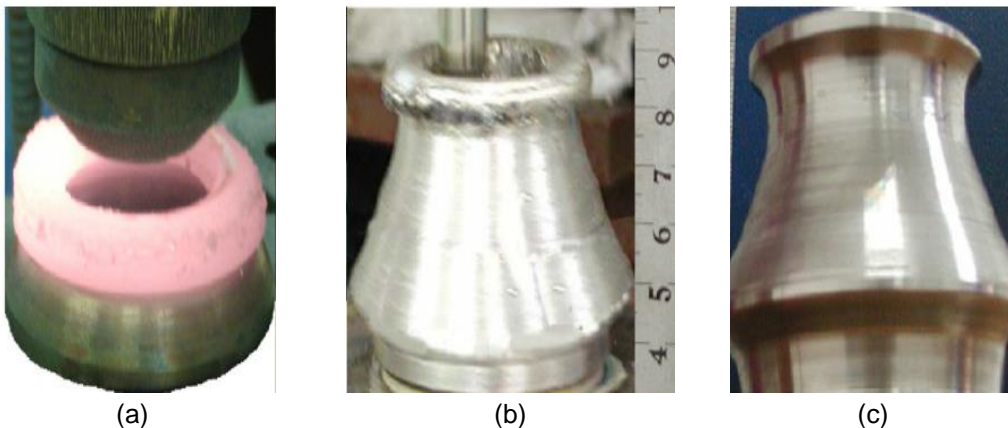


Figure 2.20. Metal vase manufactured by HPDM. (a) Plasma deposition process scene; (b) milling process scene; (c) metal vase post-processing (Xiong, Zhang, and Wang 2009).

3D Welding and Milling, process comprises of gas metal arc welding for deposition and milling as a subtractive technique. Figure 2.21 shows the principle of this process. This work by Y.A song et.al is based on a 3-axis milling machine with two welding guns that are vertically attached to the spindle housing. A simple retrofitting of a common 3-axis milling machine is required in order to carry out the process, thus eliminating any need to buy special equipment such as linear axes. The two welding guns allow switching between two different wire materials or between two different wire material sizes (Song et al. 2005; Song, Park, and Chae 2005).

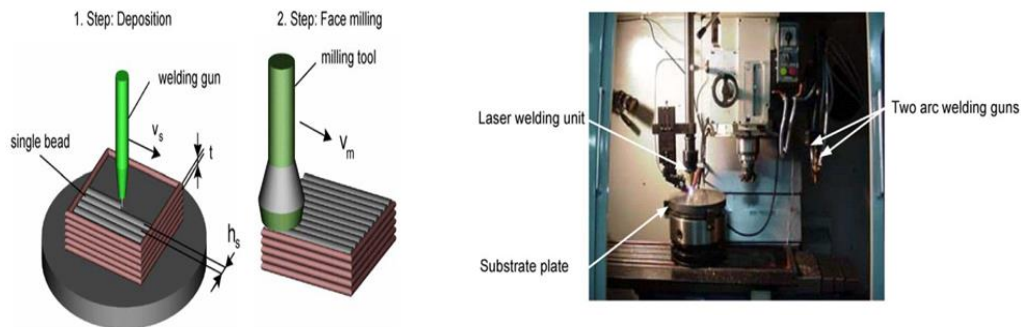


Figure 2.21. Process principle of 3D Welding and Milling (Song et al. 2005; Song, Park, and Chae 2005).

2.3 Functionally Gradient Materials (FGM)

Functionally Gradient Materials (FGM) has a controlled variation of the material matrix so as to obtain the desired distribution of the properties such as color, density, porosity, hardness, toughness etc. There is a growing interest in FGMs due to their ability to offer high toughness, high strength, machinability, better resistance to corrosion and oxidation effects, and facilitating bonding of metals without severe internal thermal stresses. However, actual realization of FGMs still remains a challenge. Most naturally occurring objects are gradient in nature; examples are bamboo, bone, stone etc. Most man-made objects on the other hand are uniform. This is mainly due to the complexity involved in their design and subsequent manufacturing.

In late 1980s, Niino et.al proposed the concept of Functionally Gradient Material, in which the gradient of the material can be adjusted by coating and controlling powder material (Niino et al. 1988). There are many techniques available today to fabricate the functionally gradient material, some of the prominent one's being vapor deposition, powder metallurgy, and centrifugal method in addition to additive manufacturing. Vapor deposition technique is mainly used for very thin surface coatings where microstructure and other properties can change. In powder metallurgy techniques, different form of powder material is used for achieving gradient objects. Centrifugal techniques, as the names implies, are based on centrifugal force; the material will get dispersed and bulk material will be controlled to form gradient in the object. The above three techniques have limitations in the extent of gradient nature or

flexibility of the process as they rely upon manual process planning. Due to its ability to tackle the above limitations, additive manufacturing was looked by many researchers as a better alternative to realize gradient structure as it is based on selective addition of material at required location.

Figure 2.22 illustrates various forms of materials composition possible. Figure 2.22 (a) shows a homogeneously distributed material across the object. Figure 2.22 (b) shows an object with requirements which is more difficult to meet completely through the approach of composite materials or conventional material processing methods. Figure 2.22 (c) shows an regulated spread meant for application of research interest (Hopkinson, Hague, and Dickens 2006).

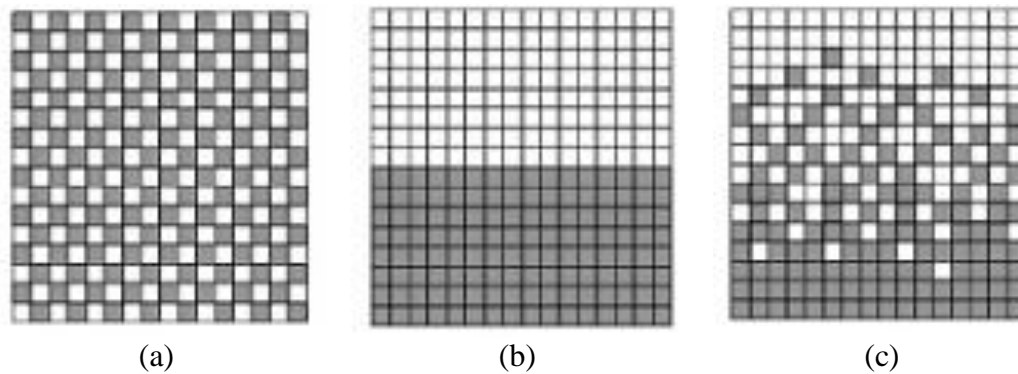


Figure 2.22. Various forms of material composition (a) homogeneous (b) coated or joint type (c) FGM (Hopkinson, Hague, and Dickens 2006).

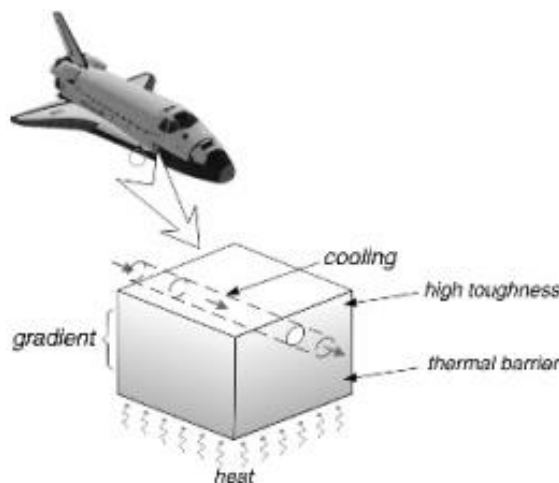


Figure 2.23. Example of different requirements of material properties in different locations within a part (Hopkinson, Hague, and Dickens 2006).

Gradient also known as gradient of material can be classified as one-dimensional, two-dimensional, and three-dimensional gradients, which is shown in Figure 2.24. Figure 2.24 (a) shows the gradient varying along the Z axis direction, yet not along X and Y, and therefore called one-dimensional gradient change. Figure 2.24 (b) shows that gradient varies along both X and Y axis, yet not along Z, therefore called two-dimensional gradient change. Figure 2.24 (c) shows gradient varying along three axis directions, which is called three-dimensional gradient change.

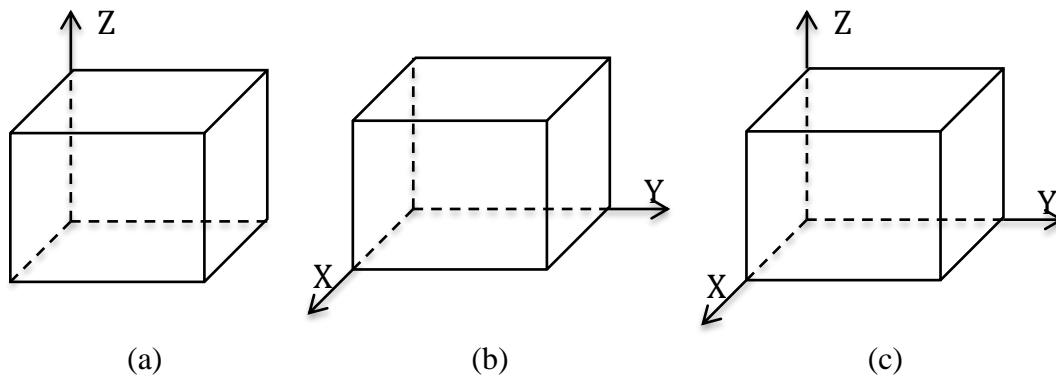


Figure 2.24. Three ways of material gradient change (a) 1-D gradient (b) 2-D gradient (c) 3-D gradient (Wang and Shang 2009).

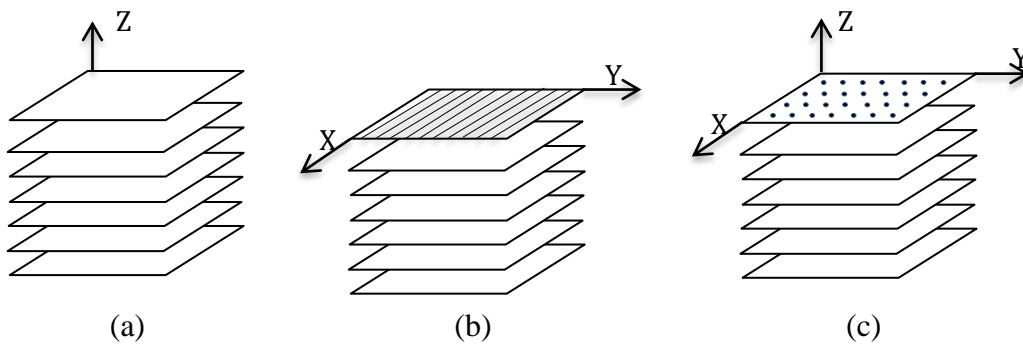


Figure 2.25. Three representations of laser rapid prototyping material gradient change (a) face gradient (b) line gradient (c) point gradient (Wang and Shang 2009).

FGM Gradient in the component can be distributed based on layer slicing and scanning fill, face, line, and point. Figure 2.25 (a) shows face gradient which is gradient change between two layers, but not in every layer. Figure 2.25 (b) shows line gradient which is gradient change across layers and within every layer. Figure 2.25 (c) shows point gradient which is gradient change in every point position (Wang and Shang 2009).

2.4 Functionally Gradient Objects through AM

Among the AM processes available today, FGMs are possible through binder jetting, directed energy deposition, material jetting, powder deposition and sheet lamination. Binder jetting, which creates an object by jetting of a binder on a layer of powder, achieves FGM by using different binders of suitable colors. Material jetting printers achieve the gradient by micro jetting different colors and materials, a process very similar to the traditional paper printers. In powder-bed deposition technique, the powder material is sintered to form the final component. Using this technology, Chung et al. explored creation of different layers by employing different volume fractions of glass beads in Nylon-11 composites. Sheet lamination deposition processes like Laminated Object Manufacturing (LOM) and Ultrasonic Consolidation (UC) combines different foil or layered sheet to obtain the desired component. Zhang et al. and Kumar explored different combinations of amorphous graphite, titanium powder and stainless steel Al and Cu foils used for gradient component for sheet lamination processes like Laminated Object Manufacturing (LOM) and Ultrasonic Consolidation (UC) respectively (Yumin Zhang et al. 2001) (Kumar 2010). Directed energy deposition melts the target area using laser or electron beam as the energy source to create the final component. Laser Net Shaping Engineering (LENS), has been the most popular of these processes for achieving FGM due to its ability to feed separate powders through the different nozzles. Using LENS process Bandyopadhyay et al. explored the FGM components for implant application, the details of which will be discussed in the subsequent section.

2.4.1 Laminated Objective Manufacturing (LOM)

Fabrication of FMGs using LOM was carried out in two steps: forming and synthesizing process. Forming process is mixing the powder of amorphous graphite and titanium powder, in addition to Ni powder from 10 to 50 wt% (Figure 2.26). The mixed powder is ball milled up to 12h and kept in vacuum for drying. After some time, a green tape of 0.5 thicknesses and a mixture of Ti, C and Ni is formed through the roll forming process with Polyvinyl Alcohol as binder. RPMS-II system they were used for manufacture of FGM green part by using LOM process. RPMS-II model of

LOM, system can manufacture green FGM part according to 3D CAD model. FGM green part is kept in vacuum chamber and heated up to 300°C for removing the binder. Mechanical properties of TiC/Ni FGM part vary based on contents of Ni; if the Ni was 20% wt, FGM has the highest strength (Yumin Zhang et al. 2001).

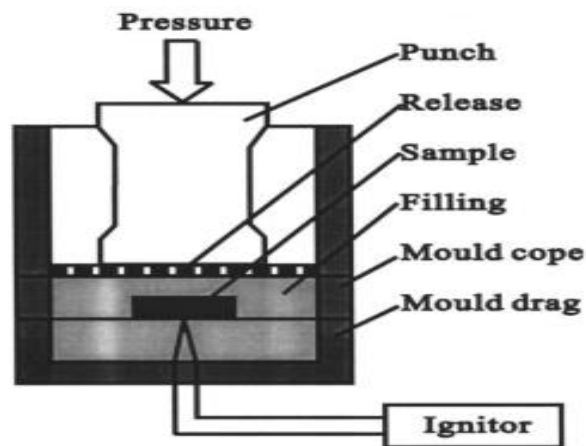


Figure 2.26. SHS experimental equipment (Yumin Zhang et al. 2001).

Zhang et al. reported thickness of the product was about half that of the green part, which meant that the density of FGM increased after combustion synthesis process (Yumin Zhang et al. 2001). Klosterman et al. Studied fabricating ceramic (SiC/SiC) and polymer matrix (glass/ epoxy) composites using a novel, fully automated process. Examples are shown in Figure 2.27 & Figure 2.28 (Klosterman et al. 1998).



Figure 2.27. Examples of unidirectional glass fiber /epoxy composite parts built with LOM. The part on the right has been post-cured (Klosterman et al. 1998).

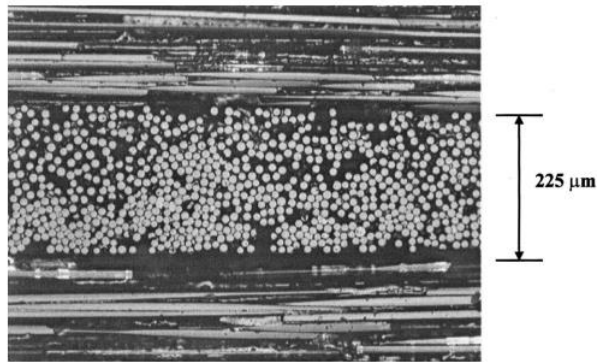


Figure 2.28. Cross-sectional photomicrograph of unidirectional fiber glass/epoxy composite, built with LOM. Prepreg layers have staggered 0/90 orientation (Klosterman et al. 1998).

2.4.2 Ultrasonic consolidation (UC)

S Kumar studied manufacturing of functionally graded materials by using UC, Stainless steel, Al and Cu foils being used for gradient. The additive parts are laminated layer by layer from bottom to top and excess materials were removed by using CNC machine. A gradient component was achieved by different metal foils stacked by ultrasonic welding, Figure 2.3 and Figure 2.29 illustrate the ultrasonic consolidation process (Kumar 2010).

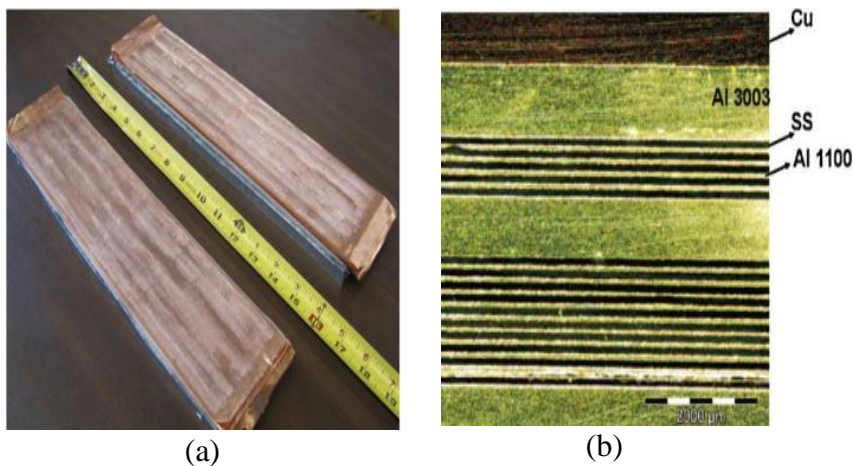


Figure 2.29. FGM component produced by UC machine (a) Frontal view of an FGM sample made using a UC machine and figure (b) Side view of the FGM sample (Kumar 2010).

2.4.3 Selective Laser Sintering (SLS)

Chung et al. studied and developed particulate-filled functionally graded Nylon-11 composites using this process filled with different volume fractions of glass beads (0–

30%). Figure 2.30 shows the specimens fabricated using this process (Chung and Das 2006). Similarly, Chun and Das also have studied the compliant gripper and the corresponding FGM as show in Figure 2.31 and rotar scaffold in Figure 2.31.

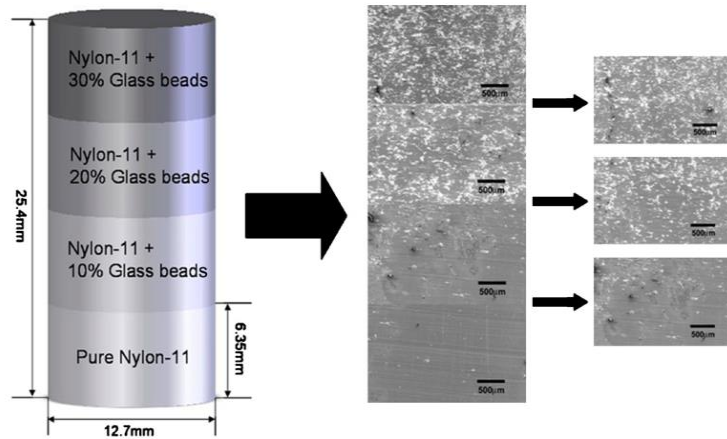


Figure 2.30. Schematic of an FGM compression test (Chung and Das 2006).

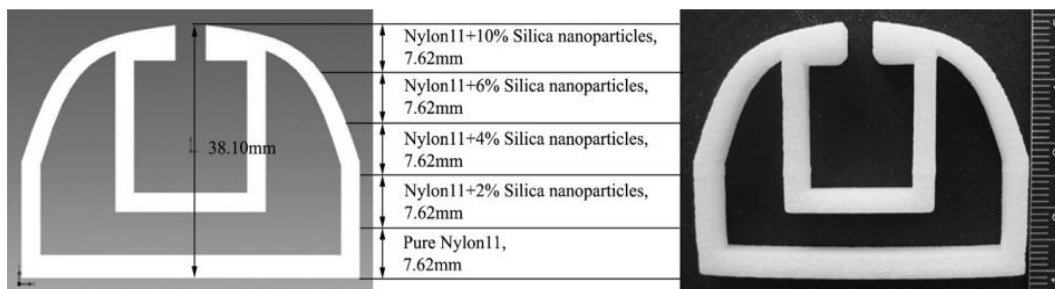


Figure 2.31. Schematic description of a compliant gripper and the corresponding FGM component fabricated by SLS.(Chung and Das 2006).

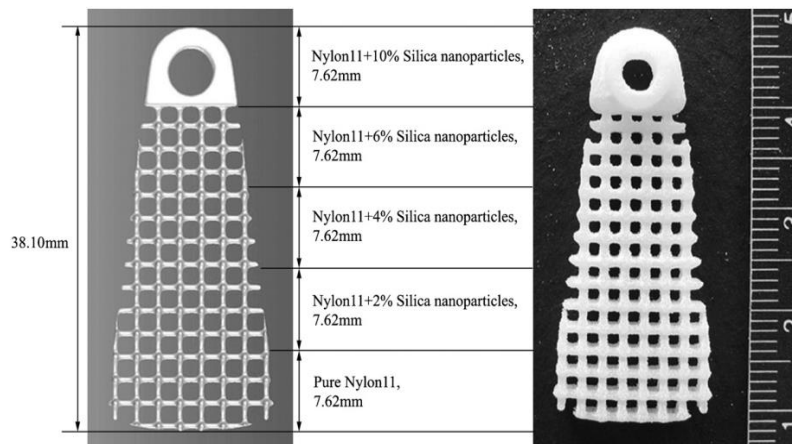


Figure 2.32. Rotator cuff scaffold and the corresponding FGM component fabricated by SLS (Haseung and Das 2008; Chung and Das 2006).

2.4.4 Zcorp's 3D Printing

Zcorp's 3D printing represents FGM of mechanical properties using the color information. The object in which the mechanical properties vary gradually based on the concentration of the binders is referred to as a "functionally graded" material. Figure 2.33 illustrates color model produced by using ZPrinter® 650 machine.

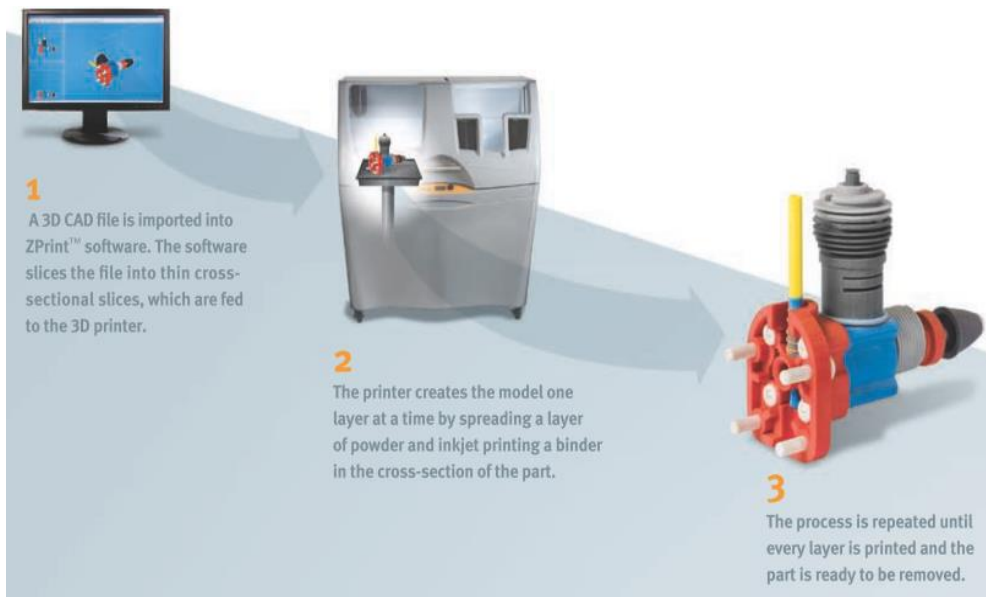


Figure 2.33. Schematics of color parts fabricated with ZCorp's 3D printer (Printers 2015).

2.4.5 Laser Engineering Net Shaping (LENS)

With material being deposited from four different nozzles, LENS is one of the most popular RM process capable of producing variety of FGMs including those with Ti alloys. Liu et al. reported that using LENS process crack-free functionally graded TiC/Ti composite materials are possible to fabricate with compositions changing from

pure Ti to approximately 95 vol% TiC. Figure 2.34 shows the crack observed in the homogenous deposit (Liu and DuPont 2003).

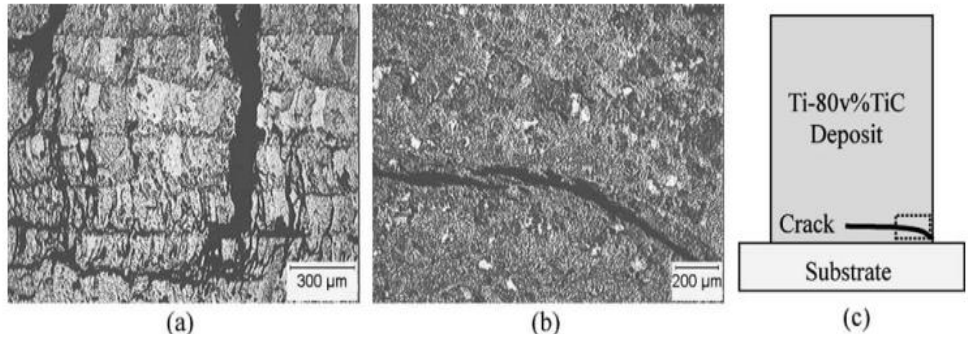


Figure 2.34. Cracks observed in the homogeneous deposits: (a) full TiC deposit; (b) Ti 80vol%TiC composite deposit; (c) a schematic showing the originating position of the crack in the composite deposit (Liu and DuPont 2003).

Domack et al. studied and reported a bulk material of composition gradient from Ti-6-4 to Inconel 718. Fabricated samples are shown in Figure 2.35 and Figure 2.36 (Domack and Baughman 2005).

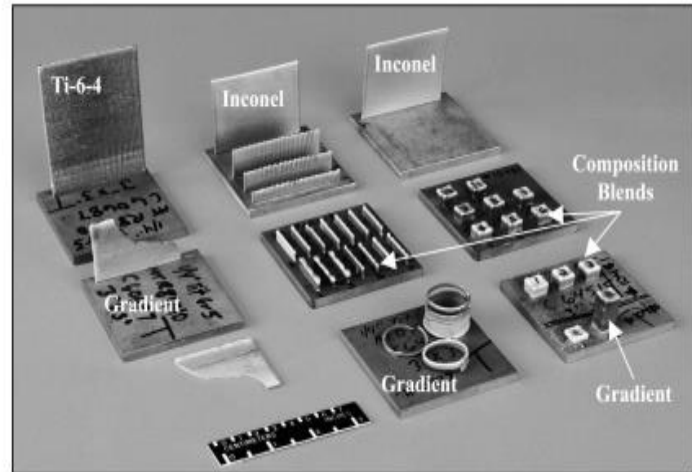


Figure 2.35. LENS samples produced from Ti-6-4 and Inconel 718 powders (Domack and Baughman 2005).

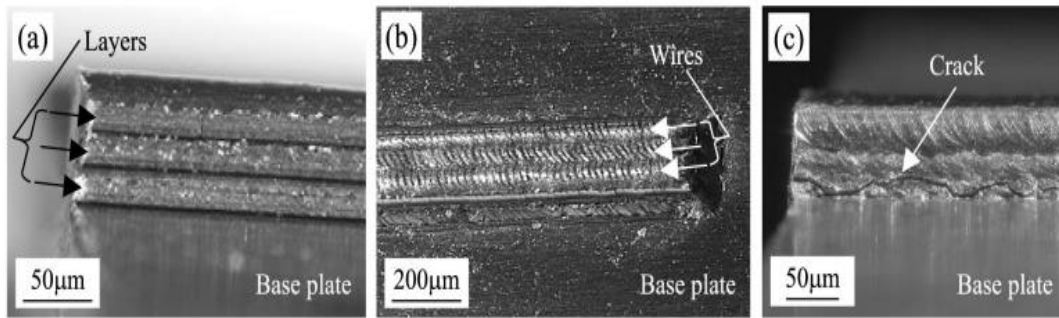


Figure 2.36. Typical appearance of the flat wire welded samples, illustrating: (a) three layers; (b) solidification fronts along the three wires in each layer; and (c) cracking at the base of the Ti-6-4 deposits (Domack and Baughman 2005).

Bandyopadhyay et al reported using LENS process fabrication of net shape for load bearing implants of complex metallic implants shapes with designed porosities up to 70 vol.%, process schematic is shown in Figure 2.37 and Figure 2.38 (Bandyopadhyay et al. 2009).

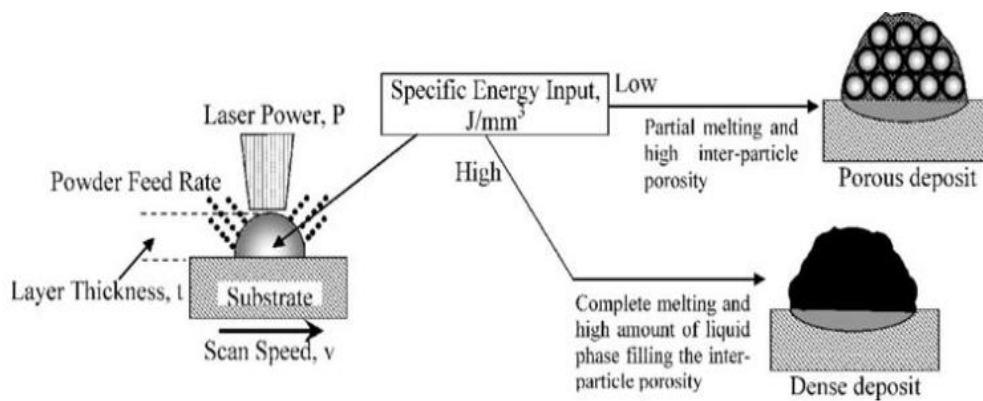


Figure 2.37. Schematic diagram showing the formation of porosity during LENS™ processing (Bandyopadhyay et al. 2009).

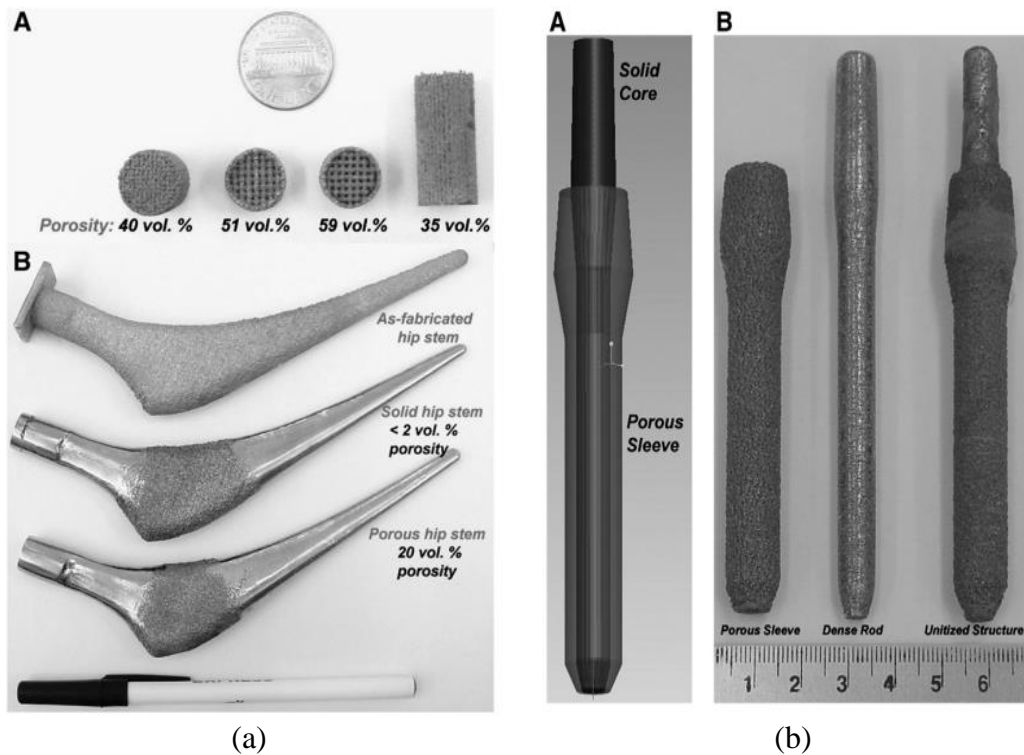


Figure 2.38. FGM component fabricated by using LENS process (a) sample with total porosity > 50 vol.% are fabricated using tool path based porosity (b) Net shape, functional hip stems with designed porosity fabricated using LENS (Bandyopadhyay et al. 2009).

2.4.6 Shape Deposition Manufacturing

SDM laser deposition system developed at Stanford University, is capable of producing functionally graded metals through the use of powder mixing. While Shape Deposition Manufacturing has always had the capability to produce multi material artifacts, powder mixing enables the deposition of single layers in which material properties can be smoothly varied without discrete interfaces between dissimilar materials. J Fessler et.al studied functional gradient material deposition which has been exploited to construct an advanced injection molding tool which transitions from Invar at the center to stainless steel on the outside, Figure 2.39 illustrates composition of chrome and nickel (Fessler, Nickel, and Link 1997).

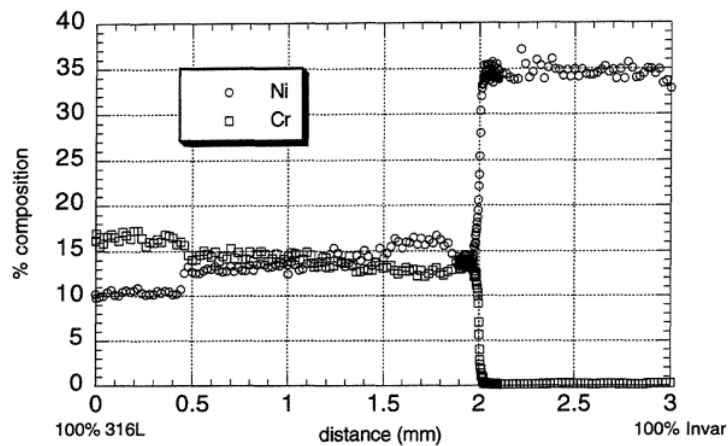


Figure 2.39. Composition of chromo and Nickel versus location for a sharp interface between Invar and 316L stainless steel (Fessler, Nickel, and Link 1997).

2.5 Modeling and process planning of gradient objects

Additive Manufacturing processes are characterized by their boundless degree of automation. Objects are produced by taking data from computer aided design (CAD) and must be made without much effort when programming the manufacturing steps. To be able to produce FGM parts by these technologies, it is necessary to receive and process data that carry the information about the gradients. One reason for the great success of AM was the use of a common and easy way to transfer data from CAD systems to the computer aided manufacture (CAM) systems of the different Additive Manufacturing technologies. The STL (Standard Triangulation Language) format was accepted as a standard for the industry. In the same way, enhancement of the STL format to store material properties is also needed. STL format contains only surface mesh information and it cannot store color, material variety and other gradient properties. Although, some of AM processes managed to fabricate the color or gradient parameters by controlling the machine settings, mirroring the same in STL was still a bottleneck. Hence, in 2012, ASTM adopted a standard format called Additive Manufacturing Format (AMF) capable of storing color or gradient properties, although the format is still under development (ASTM F2915 2015).

2.6 Summary

Extensive literature survey in the area of metallic additive manufacturing is presented. The following are some of the inferences made: Laminated manufacturing is not a

commercial success because it has only limited application due to inability to support for adaptive slicing and difficulty in joining the laminates properly. Powder-based RP processes such as SLS and SLM suffer from porosity. Both require extensive and time-consuming post-processing. Fabrication components from arc process have bad finishing and also its beads are of lower quality than laser with respect to accuracy and surface quality. Since a post-processing step like surface machining is required for most of the parts built by direct deposition approaches, the relatively low accuracy and surface quality of arc-welded beads is acceptable.

AM methods through which manufacture of FGMs have been possible have also been studied in the subsequent part. Although a certain degree of functional gradience is possible in laminated and powder bed technologies, it is rather very limited as the raw material is laminated/spread at one go for a complete layer, making only vertical gradience possible. Deposition methods on the other hand add the material in limited quantities at desired location, making it ideally suitable for manufacture of FGMs.

Chapter 3

Experimental Setup

3.1 Introduction

Twin-wire welding based Additive Manufacturing (TWAM) is a unique process which uses Gas metal arc welding (GMAW) comprising of twin-wire setup for deposition and 6 axis kuka robot for controlling the torch speed to fabricate Functionally Gradient objects/Materials (FGM). Twin-wire weld-deposition setup comprises of two wires fitted into one torch. It has two controllable digital power sources that can work independently with two separate filler wires feeding two different nozzles into a single weld pool. While the system synchronizes the frequency of the pulsing current to ensure a stable arc deposition, the current and the wire feed rate of each wire feeder can be independently controlled. Weld-deposition unit has to be integrated to the robot in such a way as to not hinder the robot movement during interpolation. A detailed description of the TWAM setup and the systems comprising the same have been presented in this chapter.

3.2 Twin-wire weld-deposition

In twin-wire, the two electrodes which are electrically insulated from each other, can be adjusted and optimized independent of one another. Both the performance and additional parameters - for instance, the lengths of the two electric arcs can be controlled separately. This means that it is possible to achieve a stable electric arc and perfect drop release for both electric arcs. Either of the electrodes can be classified as the master or the slave. This means that the electrode which has the leading role in the welding process is not defined explicitly. As a result of that, both welding directions are possible and this in turn enables a reduction in the cycle time.

Metal transfer in twin-wire: Combination of standard or pulsed electric arc is possible with the two electrodes independently. In essence, there are four possible variants viz., pulse-pulse, pulse-standard and standard-pulse and standard-standard. Figure 3.1 (a) & (b) illustrate pulsed electric arcs from both electrodes, at a phase difference of 180°.

Figure 3.1 (c) shows pulsed electric arc from one electrode and standard electric arc from the other electrode (for achieving maximum welding speed and gap bridging). The vice versa for deep penetration, is shown in Figure 3.1 (d). Standard electric arc in both the electrodes leads to irregular droplet detachment, high spatter due to the arc interference effect. Apart from these, it is also possible to employ one active electrode and perform single-wire welding. Figure 3.2 illustrates the metal transfer in such a single wire setup.

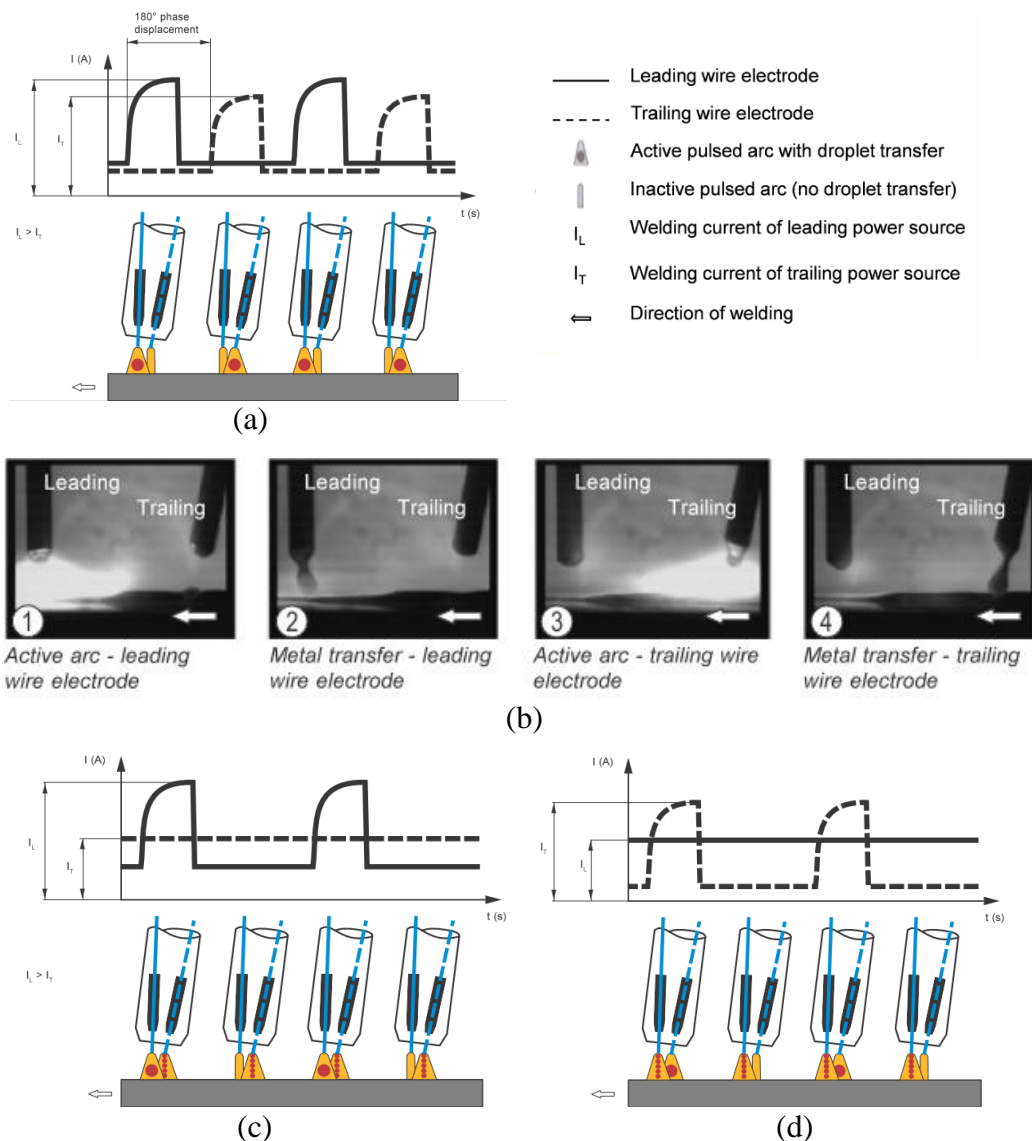


Figure 3.1. Schematic representation of the metal transfer and welding-current time-curves for Twin-wire (a) & (b) both electrodes in the pulsed electric arc (c) in pulsed/standard (d) in standard/pulsed (Fronius 2016).

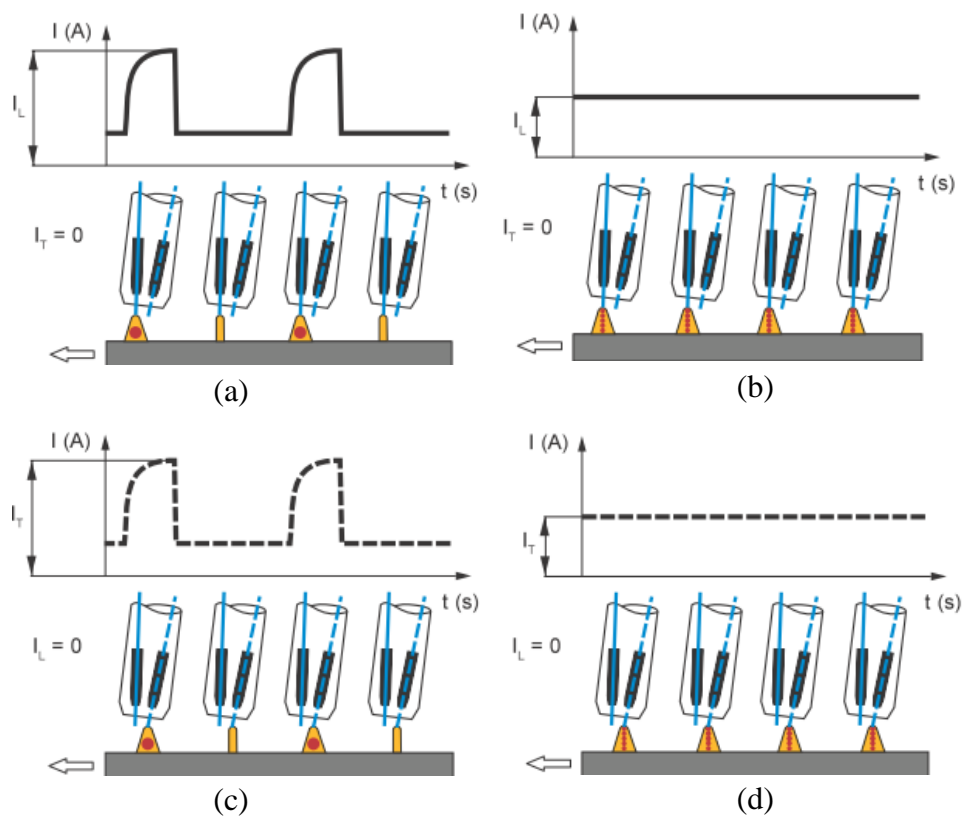


Figure 3.2. Schematic representation of the metal transfer and welding-current time-curves for single wire (a) pulsed leading power source (b) standard leading power source (c) pulsed trailing power source (d) standard trailing power source (Fronius 2016).

In the twin-wire digital process the two power sources are referred to as the “leading” power source and the “trailing” power source, respectively. Depending on the direction of welding, one of the two power source will be defined as the leading power source. The decision of which is the leading power source can be made by means of “Parameter t-c” (twin Control). On the leading power source, “Parameter t-c” is set to “On”. The leading power source specifies the frequency for the trailing power source. Figure 3.3 shows the tilt angle of the welding torch. The wire electrode of the leading power source is the “front” wire electrode which becomes the trailing power source when the direction of welding is reversed.

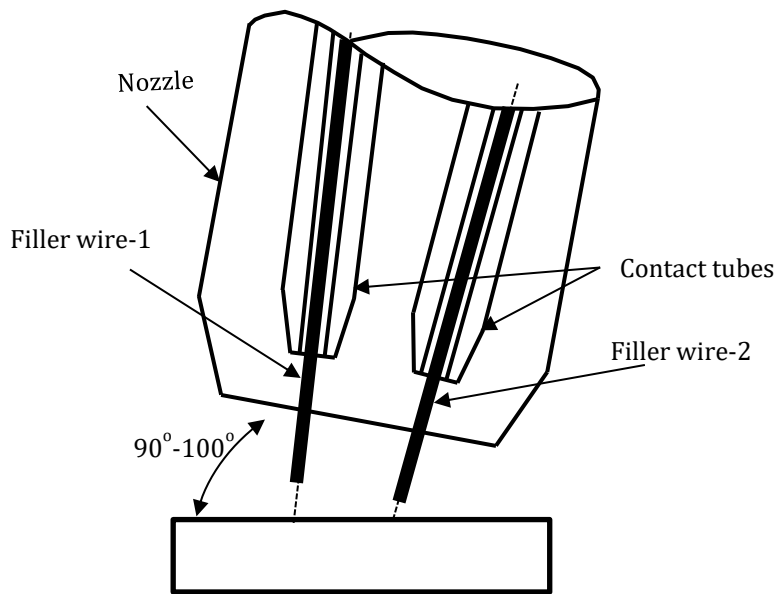


Figure 3.3. Tilt angle of the welding torch.

Figure 3.4 illustrates tilt angle and stick-out of the welding torch so that the leading wire electrode (i.e. the wire electrode of the leading power source) is held neutral to slightly leading position, depending on the direction of welding.

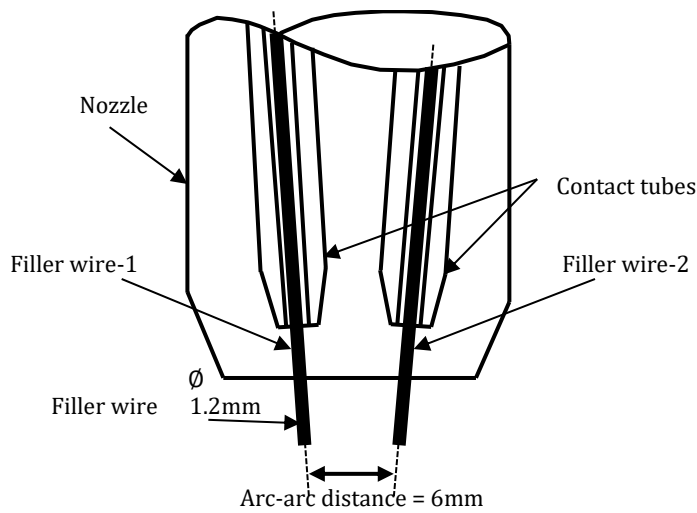


Figure 3.4. Stick-out and spacing of the wire electrodes.

Power source: There are two separate power sources for each of the electrode wires. Equipped with a Digital Signal Processor (DSP) control, these power sources makes it possible to control the welding process in a completely digital/programmable manner.



Figure 3.5. Complete welding system based on the power source Time Twin Digital 5000.

Apart from that, it is vital that the two power sources communicate with each other. This is essential for the synchronization of the two electric (Figure 3.6). This is ensured with the help of a data bus on which data transmission rates of up to 10 Mbits per second are possible. The two power sources for this process are standard power sources which have an installation set for the data bus and the appropriate software; in other words they can also be used as separate power sources. Figure 3.5 shows the power source Time Twin Digital 5000.

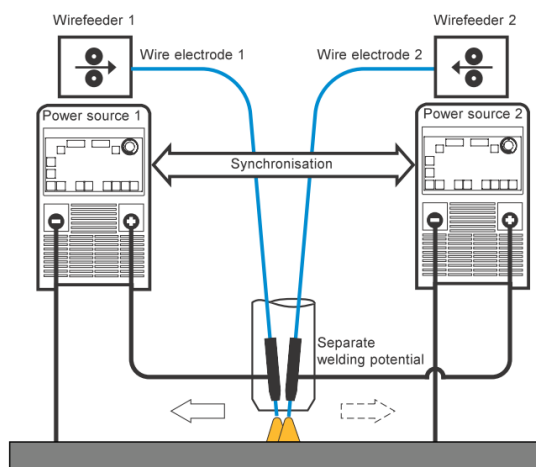


Figure 3.6. Functional principle of Time Twin Digital welding.

Welding torch: In the twin-wire process, the two wire electrodes must be converging to a single torch for the welding process. Although in this process the contact tubes of the two electrodes are electrically insulated from one another, they also run through a common gas nozzle which entails that the two electrodes must share a common welding torch. Figure 3.7 shows a schematic representation of the foremost section of the torch. Here, the electrical insulation of the two contact tubes can be seen very clearly. Because a lot of heat is generated in this process and this heat must be subsequently dissipated, the gas nozzle is cooled all the way to the front and good heat dissipation is also ensured in the area of the contact tubes.



Figure 3.7. Welding torch Robacta Twin Compact.

Twin-wire feeder: As time-wire system uses two welding wire electrodes, it also requires two wire advancing mechanisms with each advancing one electrode. The wire feeder (model: VR 1500) is usually mounted on the third robot axis, which results in a relatively short separation distance between the wire advancing mechanism and the torch. The weight of the wire advancing mechanism must be supported by the robot and that must be taken into account when dimensioning the robot, schematics shown in Figure 3.8.

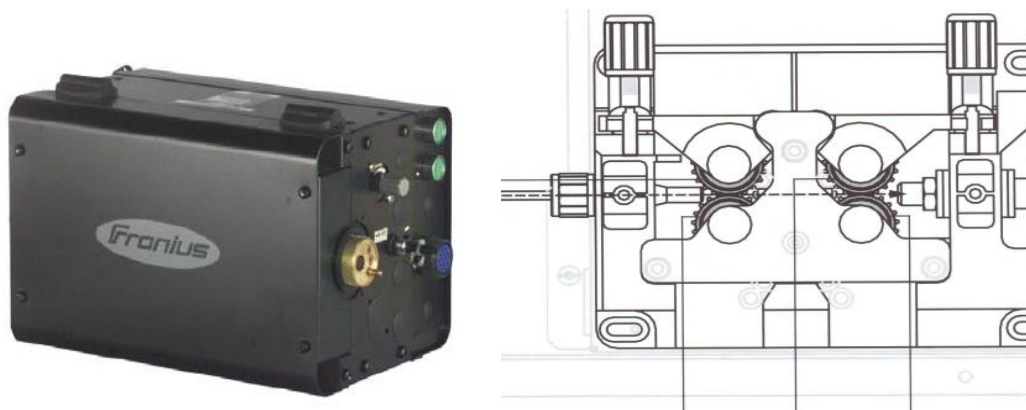


Figure 3.8. VR1500 robot wire feeder.

Welding speed and deposition rate: Using the twin-wire, it is possible to achieve considerable increase in the deposition rate compared to the conventional electric arc welding processes due to the presence of two filler wires. The user can convert this higher deposition rate either into a higher welding speed or into a greater cross-sectional area of the seam. In most applications, the increase in welding speed is of chief significance. The exact factor by which the welding speed can be increased depends on the material, the thickness of the sheet metal, the geometry of the seam, the welding positions etc.

Integration of robot and weld-deposition unit: As fabrication of FGMs demand the localized control of weld-deposition parameters, the location of the torch (controlled through robot position) and the weld-deposition parameters (controlled through power sources) should be simultaneously regulated in a synchronized manner. This is achieved with the help of a single robot controller which coordinates both the aspects. The complete robot set up is illustrated in Figure 3.9.

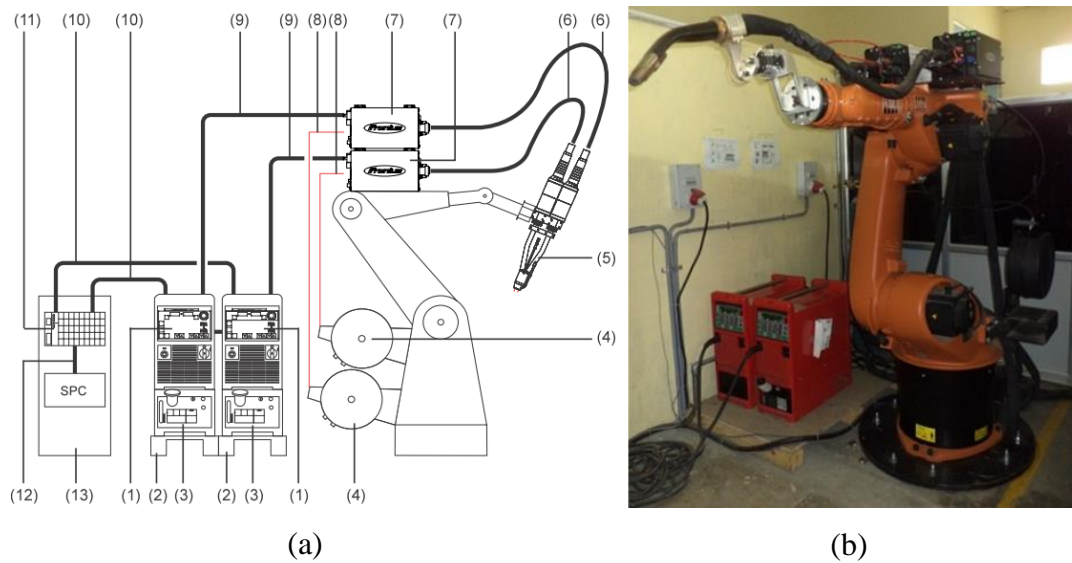


Figure 3.9. (a) Simple drawing of integrated robot and weld set up (b) complete experimental set up of TWAM.

- | | |
|-------------------------------------------------------------------------|-------------------------------------------------|
| (1) TPS 5000 power source(2x) | (8) Wire feed hose(2x) |
| (2) Base stand(2x,bolted) | (9) Standard interconnecting cable(2x) |
| (3) FK 4000R cooling unit(2x),each with optional rate of floe watch god | (10) Remote-control cable(LocalNet,2x) |
| (4) Wires pool holder on robot(2x) | (11) Twin Standard I/O job robot interface (1x) |
| (5) Robacta Twin 500 welding torch(1x) | (12) Cable connector to robot control(1x) |
| (6) Robacta drive Twin torch hose pack (1x) | (13) Robot control(1x) |
| (7) VR 1500 robot wire feeder(2x) | |

3.3 Position and movement control in robot

The torch is attached to the kuka robot for movement control. The robot arm can move from one location to the other in three main ways viz., rapid motion, linear motion and circular motion.

Rapid motion: Rapid motion also called point to point (PTP) motion is used to move as fast as possible from one point to other point, minimizing the non-productive time during the operating cycle. In this, fastest path is necessarily the shortest path; instead it is a resultant of each axis reaching the destination independently at maximum speed. The robot axes are rotational and curved path can be executed faster than straight path. The command PTP is usually programmed in a robot to initiate point to point in rapid motion Figure 3.10 & Figure 3.11 (a) shows the inline command, robot motion.

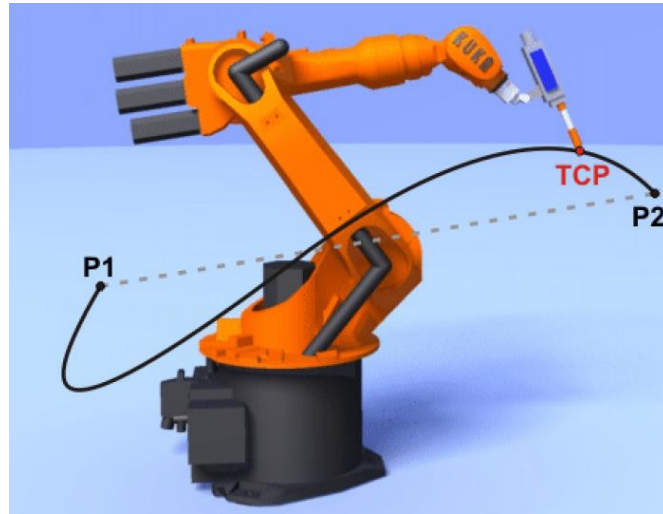
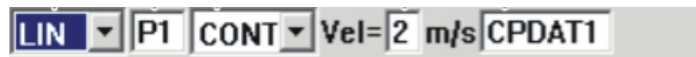


Figure 3.10. Robot arm motion in point to point (PTP) mode (Kuka 2016).



(a)



(b)



(c)

Figure 3.11. Inline form robot motions (a) point to point (PTP) (b) linear (LIN) (c) Circular (CIRC).

Linear motion: Linear motion, also called straight line motion, is a type of motion which allows the end pointer straight line movements. For this movement to happen, two or three axes will move together, and robot end wrist will be moved in linear manner. LIN is the syntax used to specify the linear motion Figure 3.11 (b) & Figure 3.12 shows the inline command and path for the linear motion.

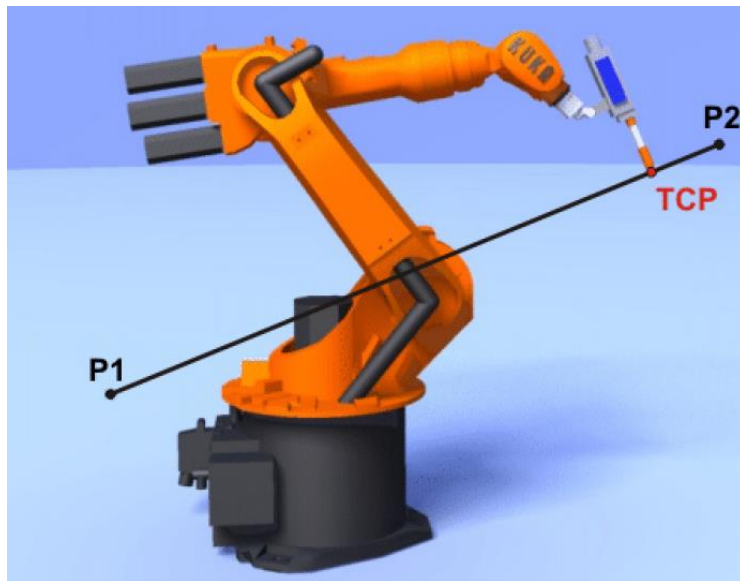


Figure 3.12. Robot movement in linear (LIN) motion (Kuka 2016) .

Circular motion: This path motion can be defined as start, auxiliary and end point, and is used to generate radii, which is used to move the robot end wrist in a circular path. During this movement, the robot guides the tool center point to move in clockwise or anti-clockwise direction. CIR is the syntax used to specify the circular motion Figure 3.11 (c) & Figure 3.13 shows the inline command and path for the circular motion. In the subsequent section we will discuss how to use this syntax in welding deposition.

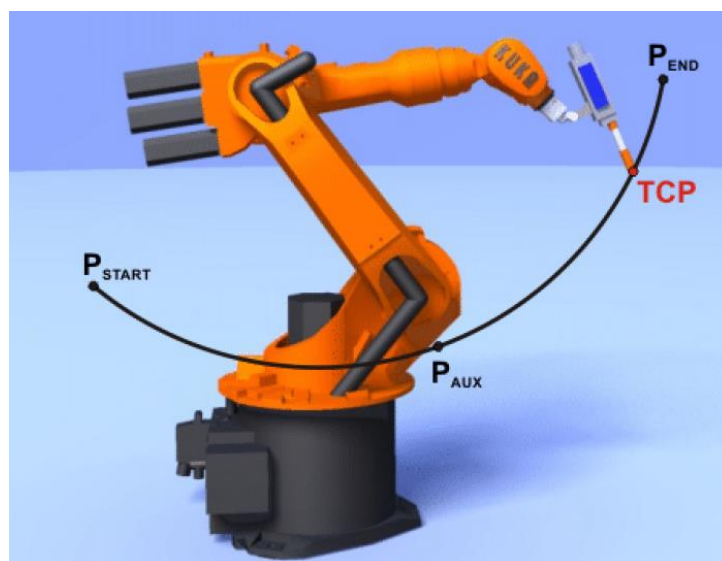


Figure 3.13. Robot movement in circular (CIRC) motion (Kuka 2016).

3.4 Robot programming for weld-deposition

Single bead deposition: Weld commands can be defined in the arc tech digital in robot control panel (Figure 3.14.). Figure 3.15 shows a simple example having all motions available in robot weld-deposition; deposition of two seams in which seam-1 consists of point-to-point (PTP) and linear motion and seam-2 having a circular arc. The end interpolator comes in PTP mode up to P1, and after it reaches to P1 welding triggers and gets on with parameter S1 set in program number 1. From there, it moves in linear motion to P2 and switch off is triggered. An inline program is shown in Figure 3.16. Similarly, for seam-2, in PTP motion, move the torch upto the clearance place to avoid hitting the workpiece. Again, move to the start point of seam-2, P4 (Figure 3.17) via the auxiliary point P3 to do complete the circular (CIR) motion with parameters S2. Once reaches to P7, then it will be commence linear motion.



Figure 3.14. Kuka robot control panel.

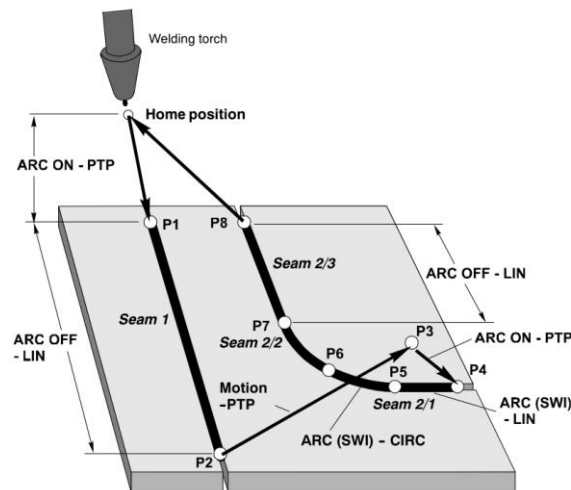


Figure 3.15. Schematic representation of weld-deposition of two seams.

```

1  INI
2  PTP HOME Vel= 100 % DEFAULT
3
4  PTP P1 Vel= 100 % PDAT1 ARC_ON Pgno= 1 S1 Seam1
5  LIN P2 CPDAT1 ARC_OFF Pgno= 1 E1 Seam1
6  PTP HOME Vel= 100 % DEFAULT
7  END

```

Figure 3.16. Inline program of seam 1.

```

1  INI
2  PTP HOME Vel= 100 % DEFAULT
3
4  PTP P1 Vel= 100 % PDAT1 ARC_ON Pgno= 1 S1 Seam1
5  LIN P2 CPDAT1 ARC_OFF Pgno= 1 E1 Seam1
6  PTP P3 CONT Vel= 100 % PDAT2
7  PTP P4 Vel= 100 % PDAT3 ARC_ON Pgno= 1 S2 Seam2
8  LIN P5 CONT CPDAT2 ARC Pgno= 1 W1
9  CIRC P6 P7 CONT CPDAT3 ARC Pgno= 1 W2
10 → LIN P8 CPDAT4 ARC_OFF Pgno= 1 E2 Seam2
11 PTP HOME Vel= 100 % DEFAULT
12 END

```

Figure 3.17. Inline program of seam 1 and seam 2.

Multi-bead deposition: The earlier section discussed how to achieve similar weld beads with different kind of motion in process. This section will focus on how to use those commands and create multi-bead deposition with different parameters. Figure 3.18 shows the one such representation of multi-bead deposition using only linear motion. P1, P2 and W1, W1 are the path of deposition and different weld parameter respectively. The weld-deposition process parameters required at a given location are archived by calling the corresponding program number. Figure 3.18 shows the

schematic representation of welding path and discrete segment points between the weld beads.

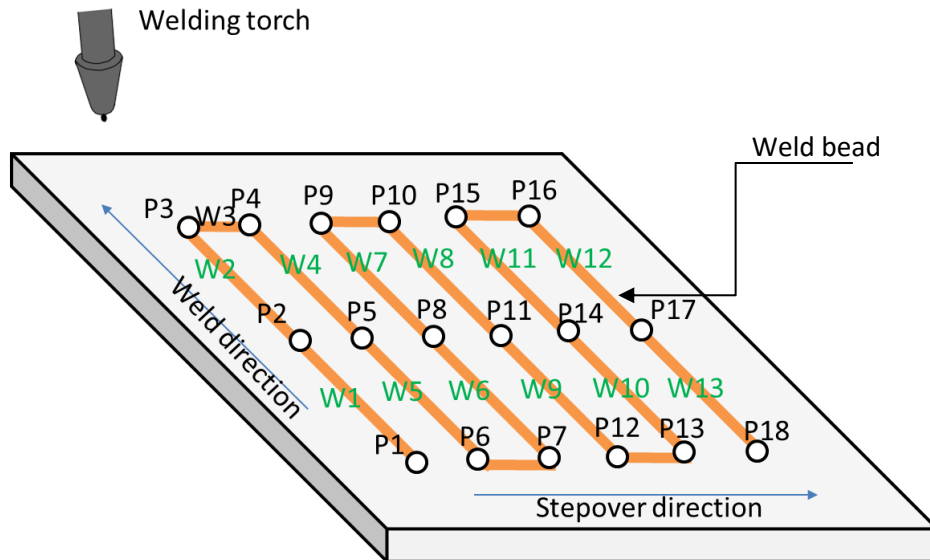


Figure 3.18. Schematic representation of weld path for multi-bead deposition of one layer.

Generation of tool paths in robot format: Figure 3.19 illustrates the various steps followed in the fabrication of gradient objects. In the first step, the CAD model is sliced into 2D layers and area filling paths for a given layer generated with the help of any slicing and path planning software (like Slic3r). The tool paths are then converted to the robot format in the next step. This will involve a simple change in the syntax of the program. The gradient material deposition is obtained by independently controlling the proportion of two different filler wires in the twin-wire welding setup. Depending on the nature of the gradient matrix, the program for calling the particular weld-deposition process parameters may be varied accordingly. The details of how to achieved gradient in weld, stepover and thickness are elaborated in chapter 5.

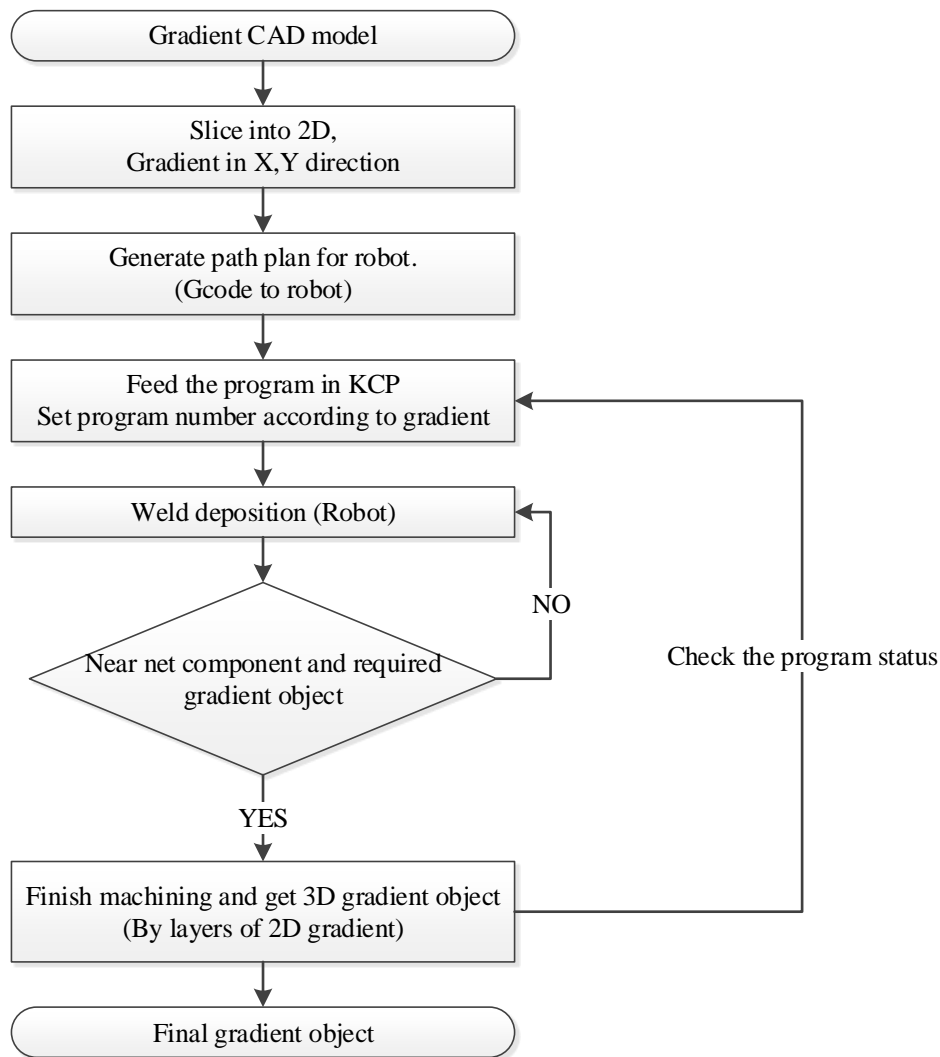


Figure 3.19. Various steps in the fabrication of gradient objects.

3.5 Summary

The experimental setup of Twin-wire Welding based Additive Manufacturing (TWAM) has been described in detail in this chapter. Working principle of twin-wire weld-deposition process along with the individual attachments viz. welding torch, wire feeder and power source have been described. The robot programming syntax and methodology for simple movements and also for single and multi-bead deposition has been described. This discussion on the experimental setup and its operational procedures sets the tone for the study of process parameters effecting the TWAM process, to be presented in the next chapter.

Chapter 4

Preliminary Study of Parameters

Effecting TWAM process

4.1 Introduction

In weld based deposition major process parameters like welding current, torch speed, voltage, wire feed, etc. effect the nature of the final component. Hence it is essential to study the operating range and effects of each of these process parameter. Since, pulse-synchronous mode of weld-deposition is used in this setup, the process parameters to be studied boils down to current, torch speed and step over increment. For this study two filler wire of ER70S-6, ER110S-G in their three possible combinations of ER70S-6+ER70S-6, ER110S-G+ER110S-G and ER110S-G+ER70S-6 were used. To find the operating range of process parameter for these three combinations, a set of single-bead deposition experiments carried out with various welding current and torch speed are presented in this chapter. Upon finding the operating range of process parameter, the feasible region of the complete system has been calculated. In this feasible region any combination of current, wire and torch speed can be used. Beyond the process parameters, the properties of the objects may also be effected by secondary conditions like torch direction, number of beads deposited, length of weld-deposition etc. Experiments carried to investigate the effect of such secondary parameters have also been discussed in this chapter.

4.2 Operating range of primary process parameters

The various possible combinations of the process parameters of twin-wire weld-deposition with two different filler wires of ER70S-6 and ER110S-G can be divided into the following three cases, as shown in Figure 4.1:

1. Case-1: ER70S-6+ER70S-6
2. Case-2: ER110S-G+ER110S-G
3. Case-3: ER110S-G+ER70S-6

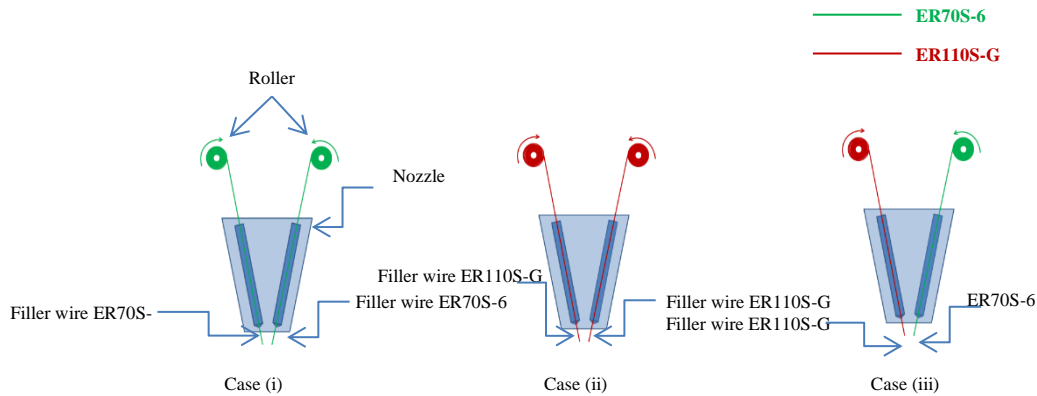


Figure 4.1. The representation of the classification of filler wire combinations.

Table 4.1. Chemical composition of ER 70S-6 and ER 110S-G filler wires [AWS A5.18 and AWS 5.28].

Elements	C	Mn	Si	P	S	Al	Ni
Composition of ER70S-6 in (%)	0.22	0.3	0.3	0.012	0.007	1.3	-
Composition of ER110S-6 in (%)	0.06	1.59	0.5	0.005	0.005	-	3.56

Table 4.2. Values of the parameters used for experiments.

Parameter	Value
Wire speed (m/min)	2-5m/min.
Torch Speed (m/min)	0.1-5m/min
Nozzle gap (base plate to torch) (mm)	16
Shielding gas flow rate (L/min)	12
Shielding gas used	82% Argon+18% CO ₂
Wire Diameter	1.2mm
Filler materials	ER 70S-6, ER110G-S

Weld-deposition in single beads of length 120mm each was carried out on a 28mm thick MS plate, shown in Figure 4.3. The minimum current permissible is 70A, 75A and 75A for cases 1, 2 and 3 respectively. The maximum current was fixed at 250A as the bead is too thick and undesirable beyond that point. The current was varied in this range in increments 5A. The torch speed was varied from 0.1 to 5m/min in increments of 0.1m/min. The remaining process parameters were maintained at the constant values mentioned in Table 4.2. Table 4.3, Table 4.4 and Table 4.5. Depict the weld quality matrix for the above cases. The red colour matrix indicate unsuitable weld beads either due to discontinuity in weld beads or a very high value of bead

width to be feasible for consecutive weld-deposition. The green indicates the suitable weld beads; these were decided based on visual inspection, taking parameters like weld bead continuity, stable arc, low spatter, narrow bead shape etc. in to consideration. The yellow matrix refers to weld-beads showing inconsistent behaviour with some trails being suitable and some being unsuitable. Based on this matrix, the feasible region of each combination was identified, as shown in Figure 4.5. The shaded area in the figure is the overlapping region of all the three cases and hence, adopted as the working region as all the possible combinations will be feasible here. It may also be noted that, sometimes use of wire-speed as a parameter may be more convenient than use of current. Due to the synchronous mode of the weld-deposition, there is a one-to-one mapping possible for current and wire-speed parameters, as shown in Figure 4.2. Hence, these parameters have been used in interchangeable manner suiting to the context.

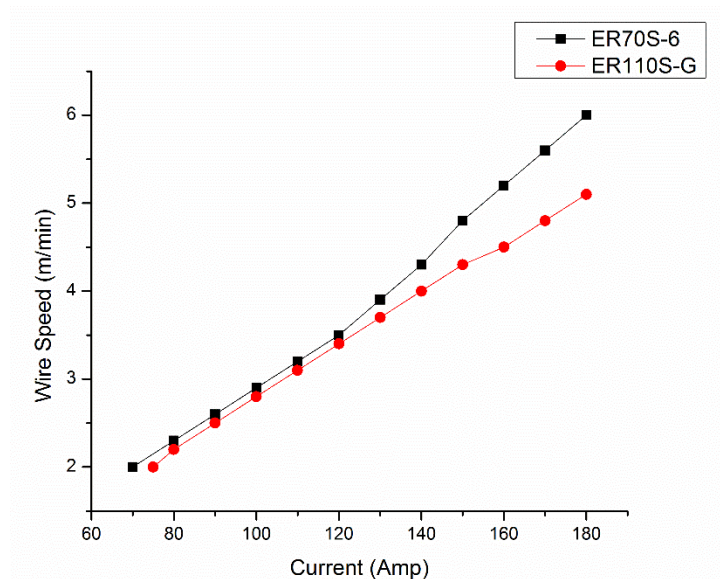


Figure 4.2. Current vs wire speed graph for 1.2mm Mild Steel.

Table 4.3 Weld bead suitability for various values of current and torch speed (ER70S-6+ER70S-6).

		Current in amp																
		70	75	80	85	90	95	100	105	110	115	120	125	130	135	140	145	150
Torch speed in m/min	0.1	x	x	x	x	x	x	x	x	x	x	x	x	x	x	x	x	x
	0.2	x	x	x	x	x	x	x	x	x	x	x	x	x	x	x	x	x
	0.3	x	x	x	x	x	x	x	x	x	x	x	x	x	x	x	x	x
	0.4	x	x	x	x	x	x	x	x	x	x	x	x	x	x	x	x	x
	0.5	✓	✓	✓	-	-	-	x	x	x	x	x	x	x	x	x	x	x
	0.6	✓	✓	✓	✓	✓	✓	-	-	x	x	x	x	x	x	x	x	x
	0.7	✓	✓	✓	✓	✓	✓	✓	✓	✓	-	-	x	x	x	x	x	x
	0.8	✓	✓	✓	✓	✓	✓	✓	✓	✓	✓	✓	-	-	x	x	x	x
	0.9	✓	✓	✓	✓	✓	✓	✓	✓	✓	✓	✓	✓	✓	-	x	x	x
	1.0	✓	✓	✓	✓	✓	✓	✓	✓	✓	✓	✓	✓	✓	✓	-	-	x
	1.1	✓	✓	✓	✓	✓	✓	✓	✓	✓	✓	✓	✓	✓	✓	✓	✓	✓
	1.2	✓	✓	✓	✓	✓	✓	✓	✓	✓	✓	✓	✓	✓	✓	✓	✓	✓
	1.3	✓	✓	✓	✓	✓	✓	✓	✓	✓	✓	✓	✓	✓	✓	✓	✓	✓
	1.4	✓	✓	✓	✓	✓	✓	✓	✓	✓	✓	✓	✓	✓	✓	✓	✓	✓
	1.5	✓	✓	✓	✓	✓	✓	✓	✓	✓	✓	✓	✓	✓	✓	✓	✓	✓
	1.6	✓	✓	✓	✓	✓	✓	✓	✓	✓	✓	✓	✓	✓	✓	✓	✓	✓
	1.7	✓	✓	✓	✓	✓	✓	✓	✓	✓	✓	✓	✓	✓	✓	✓	✓	✓
	1.8	✓	✓	✓	✓	✓	✓	✓	✓	✓	✓	✓	✓	✓	✓	✓	✓	✓
	1.9	✓	✓	✓	✓	✓	✓	✓	✓	✓	✓	✓	✓	✓	✓	✓	✓	✓
	2.0	x	✓	✓	✓	✓	✓	✓	✓	✓	✓	✓	✓	✓	✓	✓	✓	✓
	2.1	x	x	x	✓	✓	✓	✓	✓	✓	✓	✓	✓	✓	✓	✓	✓	✓
	2.2	x	x	x	x	x	-	✓	✓	✓	✓	✓	✓	✓	✓	✓	✓	✓
	2.3	x	x	x	x	x	x	-	-	✓	✓	✓	✓	✓	✓	✓	✓	✓
	2.4	x	x	x	x	x	x	x	x	-	✓	✓	✓	✓	✓	✓	✓	✓
	2.5	x	x	x	x	x	x	x	x	x	-	-	✓	✓	✓	✓	✓	✓
	2.6	x	x	x	x	x	x	x	x	x	x	x	-	-	✓	✓	✓	✓
	2.7	x	x	x	x	x	x	x	x	x	x	x	x	-	✓	✓	✓	✓
	2.8	x	x	x	x	x	x	x	x	x	x	x	x	x	-	-	✓	✓
	2.9	x	x	x	x	x	x	x	x	x	x	x	x	x	x	x	-	✓
	3.0	x	x	x	x	x	x	x	x	x	x	x	x	x	x	x	x	✓
	3.1	x	x	x	x	x	x	x	x	x	x	x	x	x	x	x	x	x
	3.2	x	x	x	x	x	x	x	x	x	x	x	x	x	x	x	x	x

Table 4.4 Weld bead suitability for various values of current and torch speed (ER110S-G+ER110S-G).

		Current in amp															
		75	80	85	90	95	100	105	110	115	120	125	130	135	140	145	150
Torch speed in m/min	0.1	x	x	x	x	x	x	x	x	x	x	x	x	x	x	x	x
	0.2	x	x	x	x	x	x	x	x	x	x	x	x	x	x	x	x
	0.3	x	x	x	x	x	x	x	x	x	x	x	x	x	x	x	x
	0.4	✓	-	x	x	x	x	x	x	x	x	x	x	x	x	x	x
	0.5	✓	✓	-	-	-	x	x	x	x	x	x	x	x	x	x	x
	0.6	✓	✓	✓	✓	✓	-	-	-	x	x	x	x	x	x	x	x
	0.7	✓	✓	✓	✓	✓	✓	✓	✓	-	-	-	x	x	x	x	x
	0.8	✓	✓	✓	✓	✓	✓	✓	✓	✓	✓	✓	-	-	-	x	x
	0.9	✓	✓	✓	✓	✓	✓	✓	✓	✓	✓	✓	✓	✓	✓	-	✓
	1.0	✓	✓	✓	✓	✓	✓	✓	✓	✓	✓	✓	✓	✓	✓	✓	✓
	1.1	✓	✓	✓	✓	✓	✓	✓	✓	✓	✓	✓	✓	✓	✓	✓	✓
	1.2	✓	✓	✓	✓	✓	✓	✓	✓	✓	✓	✓	✓	✓	✓	✓	✓
	1.3	✓	✓	✓	✓	✓	✓	✓	✓	✓	✓	✓	✓	✓	✓	✓	✓
	1.4	✓	✓	✓	✓	✓	✓	✓	✓	✓	✓	✓	✓	✓	✓	✓	✓
	1.5	✓	✓	✓	✓	✓	✓	✓	✓	✓	✓	✓	✓	✓	✓	✓	✓
	1.6	✓	✓	✓	✓	✓	✓	✓	✓	✓	✓	✓	✓	✓	✓	✓	✓
	1.7	✓	✓	✓	✓	✓	✓	✓	✓	✓	✓	✓	✓	✓	✓	✓	✓
	1.8	x	-	✓	✓	✓	✓	✓	✓	✓	✓	✓	✓	✓	✓	✓	✓
	1.9	x	x	-	-	✓	✓	✓	✓	✓	✓	✓	✓	✓	✓	✓	✓
	2.0	x	x	x	x	x	✓	✓	✓	✓	✓	✓	✓	✓	✓	✓	✓
	2.1	x	x	x	x	-	✓	✓	✓	✓	✓	✓	✓	✓	✓	✓	✓
	2.2	x	x	x	x	x	-	✓	✓	✓	✓	✓	✓	✓	✓	✓	✓
	2.3	x	x	x	x	x	x	-	-	✓	✓	✓	✓	✓	✓	✓	✓
	2.4	x	x	x	x	x	x	x	x	-	✓	✓	✓	✓	✓	✓	✓
	2.5	x	x	x	x	x	x	x	x	x	x	✓	✓	✓	✓	✓	✓
	2.6	x	x	x	x	x	x	x	x	x	x	-	-	✓	✓	✓	✓
	2.7	x	x	x	x	x	x	x	x	x	x	x	x	✓	✓	✓	✓
	2.8	x	x	x	x	x	x	x	x	x	x	x	x	x	-	✓	✓
	2.9	x	x	x	x	x	x	x	x	x	x	x	x	x	x	-	✓
	3.0	x	x	x	x	x	x	x	x	x	x	x	x	x	x	x	-
	3.1	x	x	x	x	x	x	x	x	x	x	x	x	x	x	x	x
	3.2	x	x	x	x	x	x	x	x	x	x	x	x	x	x	x	x

Table 4.5. Weld bead suitability for various values of current and torch speed (ER110S-G+ER70S-6).

		Current in amp															
		75	80	85	90	95	100	105	110	115	120	125	130	135	140	145	150
Torch speed in m/min	0.1	x	x	x	x	x	x	x	x	x	x	x	x	x	x	x	x
	0.2	x	x	x	x	x	x	x	x	x	x	x	x	x	x	x	x
	0.3	x	x	x	x	x	x	x	x	x	x	x	x	x	x	x	x
	0.4	-	-	x	x	x	x	x	x	x	x	x	x	x	x	x	x
	0.5	✓	✓	-	-	-	x	x	x	x	x	x	x	x	x	x	x
	0.6	✓	✓	✓	✓	✓	-	-	-	x	x	x	x	x	x	x	x
	0.7	✓	✓	✓	✓	✓	✓	✓	✓	-	-	-	x	x	x	x	x
	0.8	✓	✓	✓	✓	✓	✓	✓	✓	✓	✓	✓	✓	-	x	x	x
	0.9	✓	✓	✓	✓	✓	✓	✓	✓	✓	✓	✓	✓	✓	-	-	-
	1.0	✓	✓	✓	✓	✓	✓	✓	✓	✓	✓	✓	✓	✓	✓	✓	✓
	1.1	✓	✓	✓	✓	✓	✓	✓	✓	✓	✓	✓	✓	✓	✓	✓	✓
	1.2	✓	✓	✓	✓	✓	✓	✓	✓	✓	✓	✓	✓	✓	✓	✓	✓
	1.3	✓	✓	✓	✓	✓	✓	✓	✓	✓	✓	✓	✓	✓	✓	✓	✓
	1.4	✓	✓	✓	✓	✓	✓	✓	✓	✓	✓	✓	✓	✓	✓	✓	✓
	1.5	✓	✓	✓	✓	✓	✓	✓	✓	✓	✓	✓	✓	✓	✓	✓	✓
	1.6	✓	✓	✓	✓	✓	✓	✓	✓	✓	✓	✓	✓	✓	✓	✓	✓
	1.7	✓	✓	✓	✓	✓	✓	✓	✓	✓	✓	✓	✓	✓	✓	✓	✓
	1.8	x	-	✓	✓	✓	✓	✓	✓	✓	✓	✓	✓	✓	✓	✓	✓
	1.9	x	x	-	✓	✓	✓	✓	✓	✓	✓	✓	✓	✓	✓	✓	✓
	2.0	x	x	x	✓	✓	✓	✓	✓	✓	✓	✓	✓	✓	✓	✓	✓
	2.1	x	x	x	-	-	✓	✓	✓	✓	✓	✓	✓	✓	✓	✓	✓
	2.2	x	x	x	x	x	-	-	✓	✓	✓	✓	✓	✓	✓	✓	✓
	2.3	x	x	x	x	x	x	x	✓	✓	✓	✓	✓	✓	✓	✓	✓
	2.4	x	x	x	x	x	x	x	-	-	-	✓	✓	✓	✓	✓	✓
	2.5	x	x	x	x	x	x	x	x	x	x	-	✓	✓	✓	✓	✓
	2.6	x	x	x	x	x	x	x	x	x	x	x	✓	✓	✓	✓	✓
	2.7	x	x	x	x	x	x	x	x	x	x	x	✓	✓	✓	✓	✓
	2.8	x	x	x	x	x	x	x	x	x	x	x	x	-	-	✓	✓
	2.9	x	x	x	x	x	x	x	x	x	x	x	x	x	x	-	✓
	3.0	x	x	x	x	x	x	x	x	x	x	x	x	x	x	x	x
	3.1	x	x	x	x	x	x	x	x	x	x	x	x	x	x	x	x
	3.2	x	x	x	x	x	x	x	x	x	x	x	x	x	x	x	x

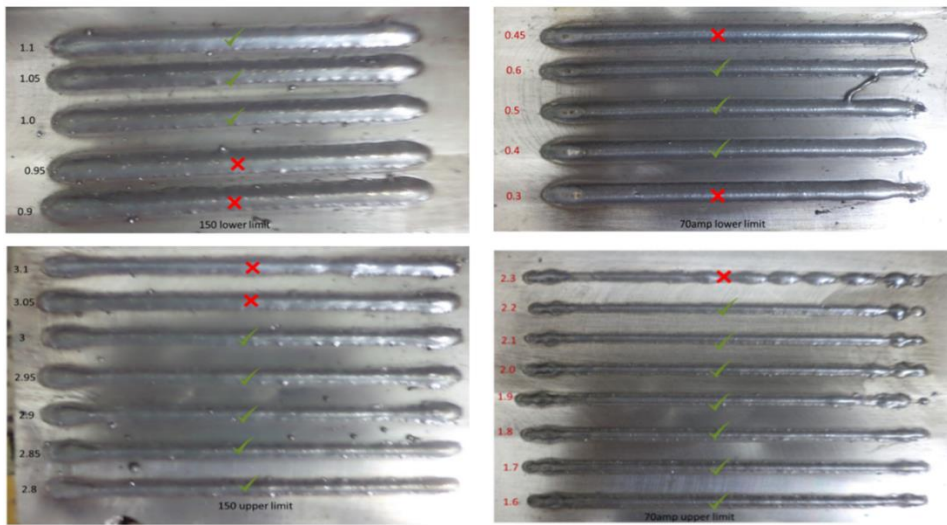


Figure 4.3. Some sample weld-bead illustrating the selection of suitable weld beads based on geometry and continuity in bead.

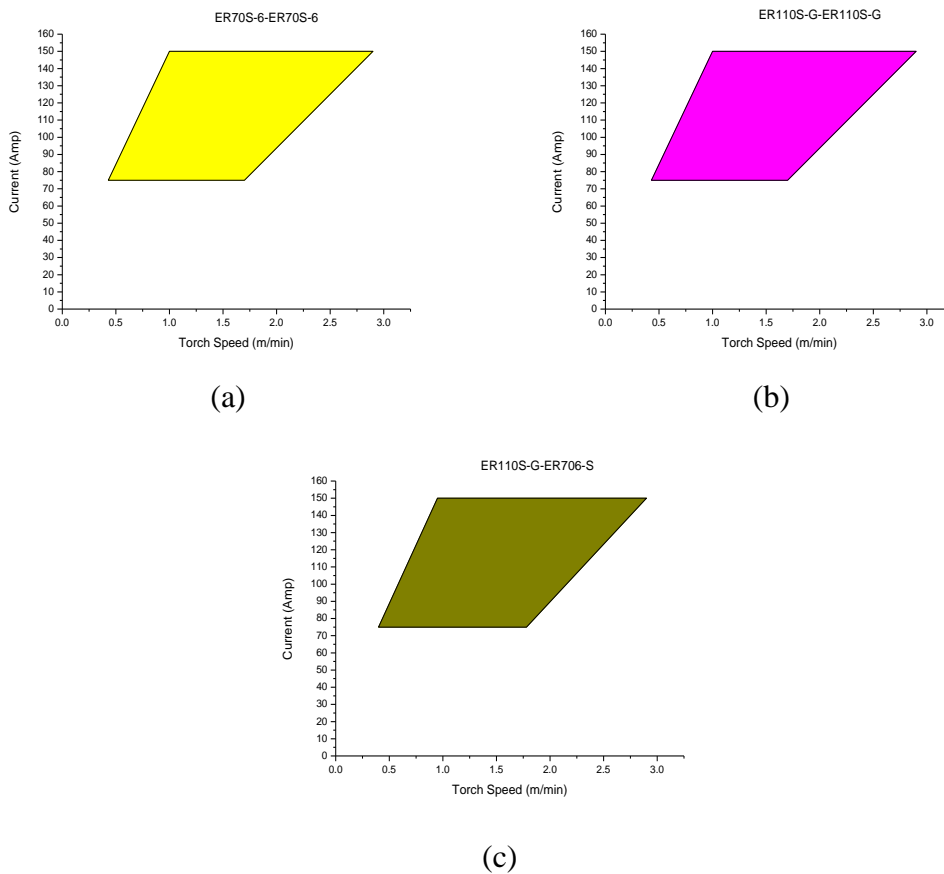


Figure 4.4. Operating range of current and torch speed of two wires (a) ER70S-6 (b) ER110S-G (c) ER70S-G and ER110S-G for weld-deposition.

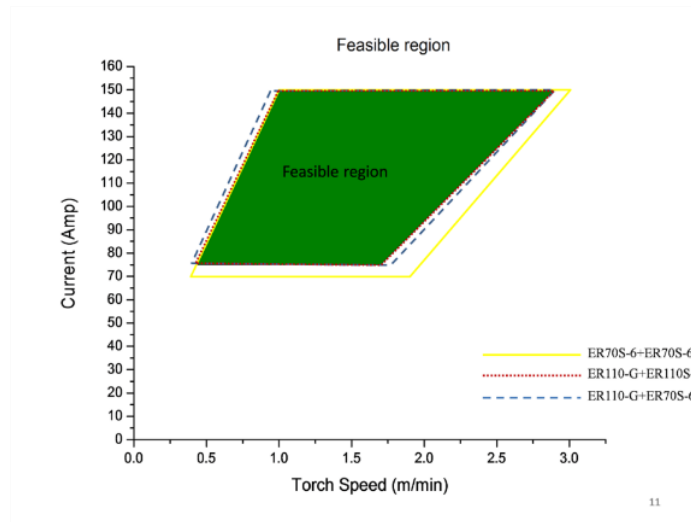


Figure 4.5. Operating range of current and torch speed of two wires and shaded area is feasible region with any combination of filler.

4.3 Weld bead profile

To identify the parameters required to obtain a desired layer thickness or optimal step-over increment (distance between two passes during weld-deposition), a geometry based model for predicting the weld bead properties based on current and torch speed used is very important. Literature suggests that the weld bead cross section follows a parabolic profile and that the optimal step-over increment is obtained when the step over increment is two-third of the weld bead width (Suryakumar et al. 2011). Experiments were carried out to confirm the suitability of this model for twin-wire deposition. As shown in the Figure 5a, a set of nine points for different values of current and torch speed were chosen for each of combination of filler wires. The deposited weld beads of the same are shown in Figure 4.6 (b)-(d).

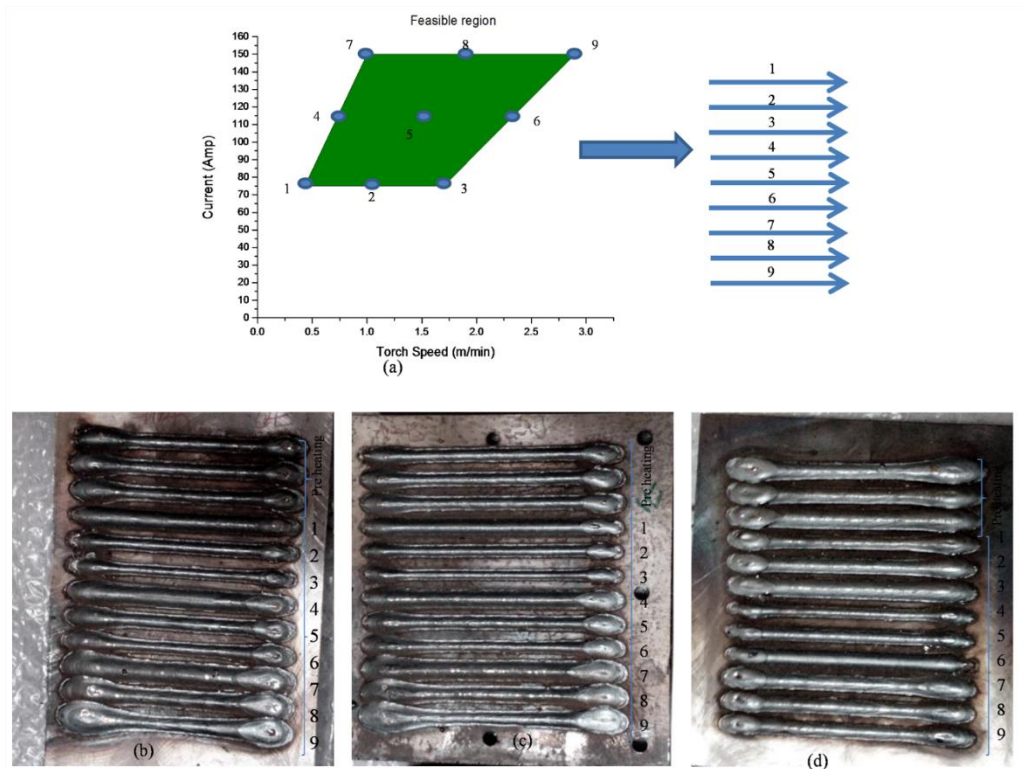


Figure 4.6. Weld bead of boundary points for each of the three combinations of filler wires
 (a) Representation of boundary points and weld beads path of (b) ER70S-6+ER70S-6 (c)
 ER110S-G+ER70S-6 (d) ER110S-G+ER110S-6.

The weld beads were sectioned with the help of EDM machine and the boundary points on the same were measured with the help of a profile projector. Figure 4.7 shows one such cross section profile of a weld bead. The boundary points were then curve fitted to a symmetrical parabola and the geometrical parameters like width, height and area was calculated. Based on the parabolic assumption of the weld bead, the area of the weld bead cross-section would be given by,

$$A_m = \frac{2wh}{3}$$

Where, A_m Area (measured from the bead cross section) (mm²)
 w Weld bead width (mm)
 h Weld bead height (mm)

The area of the weld bead cross-section can also be predicted based in the rate of filler wire coming out of the nozzle (wire speed, V_r) and speed of the weld-deposition torch (torch speed, V_t). The area of the weld bead thus predicted is given by,

$$A_p = \frac{\pi d^2}{4V_t} [V_{r1} + V_{r2}]$$

- Where A_p Area of bead predicated (mm^2)
 V_{r1} Wire speed of filler wire 1 (ER70S-6 for cases-1 & 3, ER110S-G for case-2) (m/min)
 V_{r2} Wire speed of filler wire 2 (ER70S-6 for case-1, ER110S-G for cases 2 & 3) (m/min)
 d Diameter of filler wire (mm)
 V_t Torch Speed in (m/min)

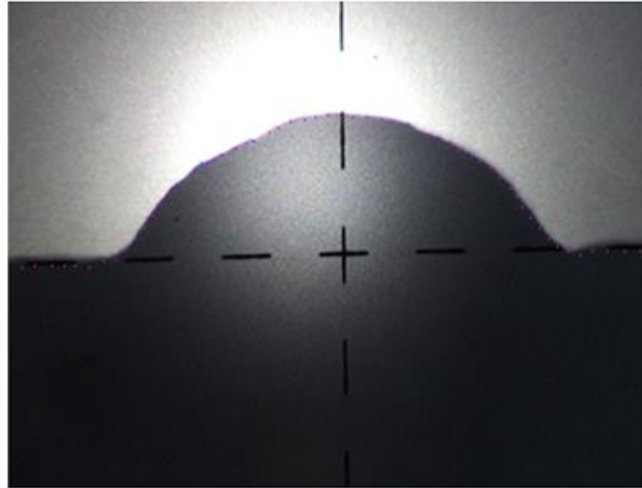


Figure 4.7. Cross section of a weld-bead used to measuring the profile.

Table 4.6. Comparison of predicted and measured cross-sectional areas of the weld bead with twin-wire combination of ER70S-G+ER70S-G for various current and torch speed.

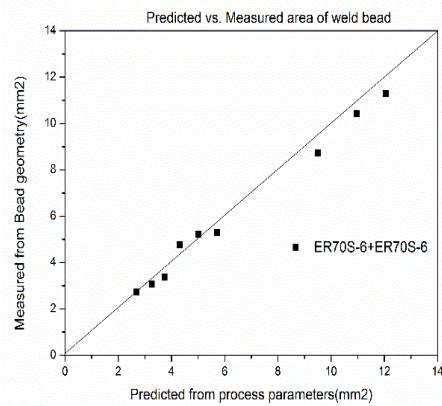
Sl	Current, I (Amp)	Wire speed V_r (m/min)	Torch speed V_t (m/min)	Width w (mm)	Height h (mm)	Area of weld bead (mm^2)		% Error
						Measured $A = \frac{2wh}{3}$	Predicated $A = \frac{2\pi V_r d^2}{4V_t}$	
1	75	2.10	0.50	6.12	2.14	8.73	9.50	-8.75
2	75	2.10	1.10	4.20	1.70	4.76	4.32	9.33
3	75	2.10	1.76	3.40	1.20	2.72	2.70	0.83
4	112	3.30	0.68	6.79	2.30	10.41	10.97	-5.38
5	112	3.30	1.49	4.41	1.78	5.23	5.01	4.32
6	112	3.30	2.29	3.41	1.35	3.07	3.26	-6.16
7	150	4.80	0.90	6.27	2.70	11.29	12.06	-6.84
8	150	4.80	1.90	5.32	1.49	5.28	5.71	-8.08
9	150	4.80	2.90	3.90	1.30	3.38	3.74	10.71

Table 4.7. Comparison of predicted and measured cross-sectional areas of the weld bead with twin-wire combination of ER110S-G+ER110S-G for various current and torch speed.

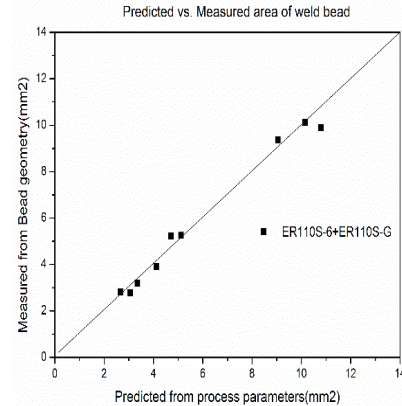
Sl	Current, I (Amp)	Wire speed V_r (m/min)	Torch speed V_t (m/min)	Width w (mm)	Height h (mm)	Area of weld bead (mm ²)		% Error
						Measured $A = \frac{2wh}{3}$	Predicated $A = \frac{2\pi V_r d^2}{4V_t}$	
1	75	2.00	0.50	6.10	2.30	9.35	9.04	3.32
2	75	2.00	1.10	4.20	1.40	3.92	4.11	4.86
3	75	2.00	1.70	3.50	1.20	2.80	2.66	5.01
4	112	3.10	0.69	6.60	2.30	10.12	10.16	-0.37
5	112	3.10	1.49	4.40	1.78	5.22	4.70	9.91
6	112	3.10	2.29	3.40	1.23	2.79	3.06	-9.77
7	150	4.30	0.90	6.20	2.39	9.88	10.80	-9.34
8	150	4.30	1.90	5.28	1.49	5.24	5.12	2.45
9	150	4.30	2.90	3.70	1.29	3.18	3.35	-5.35

Table 4.8. Comparison of predicted and measured cross-sectional areas of the weld bead with twin-wire combination of ER110S-G+ER70S-G for various current and torch speed.

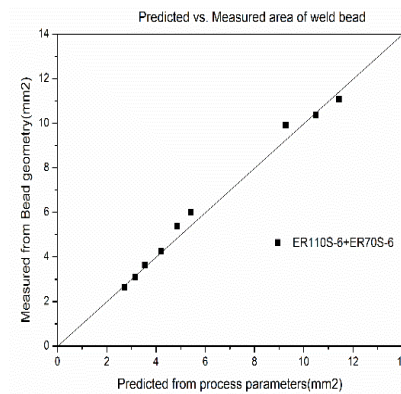
Sl	Current I (Amp)	Wire speed (m/min)		Torch speed V_t (m/min)	Width w (mm)	Height h (mm)	Area of weld bead (mm ²)		% Error
		V_{r2} ER110S-G	V_{r1} ER70S-G				Measured $\frac{2wh}{3}$	Predicated $\frac{2\pi(V_{r1} + V_{r2})d^2}{4V_t}$	
1	75	2.00	2.10	0.50	6.20	2.40	9.92	9.27	6.56
2	75	2.00	2.10	1.10	4.21	1.52	4.27	4.21	1.24
3	75	2.00	2.10	1.70	3.30	1.20	2.73	2.73	-3.20
4	112	3.10	3.30	0.69	6.50	2.39	10.36	10.48	-1.21
5	112	3.10	3.30	1.49	4.50	1.79	5.37	4.86	9.58
6	112	3.10	3.30	2.29	3.39	1.40	3.16	3.16	-2.54
7	150	4.30	4.80	0.90	6.15	2.70	11.07	11.43	-3.24
8	150	4.30	4.80	1.90	5.30	1.70	6.01	5.41	9.87
9	150	4.30	4.80	2.90	3.90	1.40	3.55	3.55	2.50



(a)



(b)



(c)

Figure 4.8. Predicted vs. measured cross-sectional areas of the weld bead for the three combination of filler wires, (a) ER70S-6+ER70S-6 (b) ER110S-G+ER110S-G and (c) ER110S-G+ER70S-6.

The measured and predicted weld bead geometries for these various cases have been listed in Table 4.6. , Table 4.7 and Table 4.8; the same are plotted against a 45° line shown in Figure 4.8 (a), (b) and (c). Interestingly, the error in case-3 was less than the other two cases, signalling a stable deposition even when dissimilar wires were used. The error in all the three cases was found to be under acceptable limits. Hence, the parabolic assumption of weld bead cross section can be adopted for the twin-wire welding also. From this it follows that for optimal deposition, the step-over increment is two-thirds of the weld bead width and the layer thickness equal to the weld bead height (Suryakumar et al. 2011). The earlier experimental values were also used to create a second degree regression model, as shown below, for predicting weld bead width and height as a function of wire speed and torch speed:

$$h = C_0 + C_1(v_{r1} + v_{r2}) + C_2v_t + C_3(v_{r1} + v_{r2})^2 + C_4v_t^2 + C_5v_t(v_{r1} + v_{r2})$$

$$w = C_0 + C_1(v_{r1} + v_{r2}) + C_2v_t + C_3(v_{r1} + v_{r2})^2 + C_4v_t^2 + C_5v_t(v_{r1} + v_{r2})$$

Where, h height of weld bead in mm

w width of weld bead in mm

$C_0 - C_5$ are the coefficient of regression model and corresponding values are listed in Table 4.9. The regression model was generated using LABFit software. The surface plot of the same is shown in Figure 4.9.

Table 4.9. Regression coefficient of area, width and height of weld beads for all combination of fillers.						
	ER70S-6+ER70S-6		ER110S-G+ER110S-G		ER110S-G+ER70S-6	
	Width	Height	Width	Height	Width	Height
C_0	1.57E+00	5.44E+00	1.44E+00	5.57E+00	1.70E+00	5.84E+00
C_1	6.13E-01	1.27E+00	9.14E-01	1.14E+00	7.27E-01	1.10E+00
C_2	-1.04E+00	-3.52E+00	-1.42E+00	-3.35E+00	-1.41E+00	-3.74E+00
C_3	-1.72E-02	-1.37E-01	-9.37E-02	-1.31E-01	-4.34E-02	-1.56E-01
C_4	3.41E-01	2.82E-01	3.04E-01	1.72E-01	3.43E-01	1.08E-01
C_5	-1.94E-01	2.50E-01	-6.32E-02	3.24E-01	-1.13E-01	4.77E-01

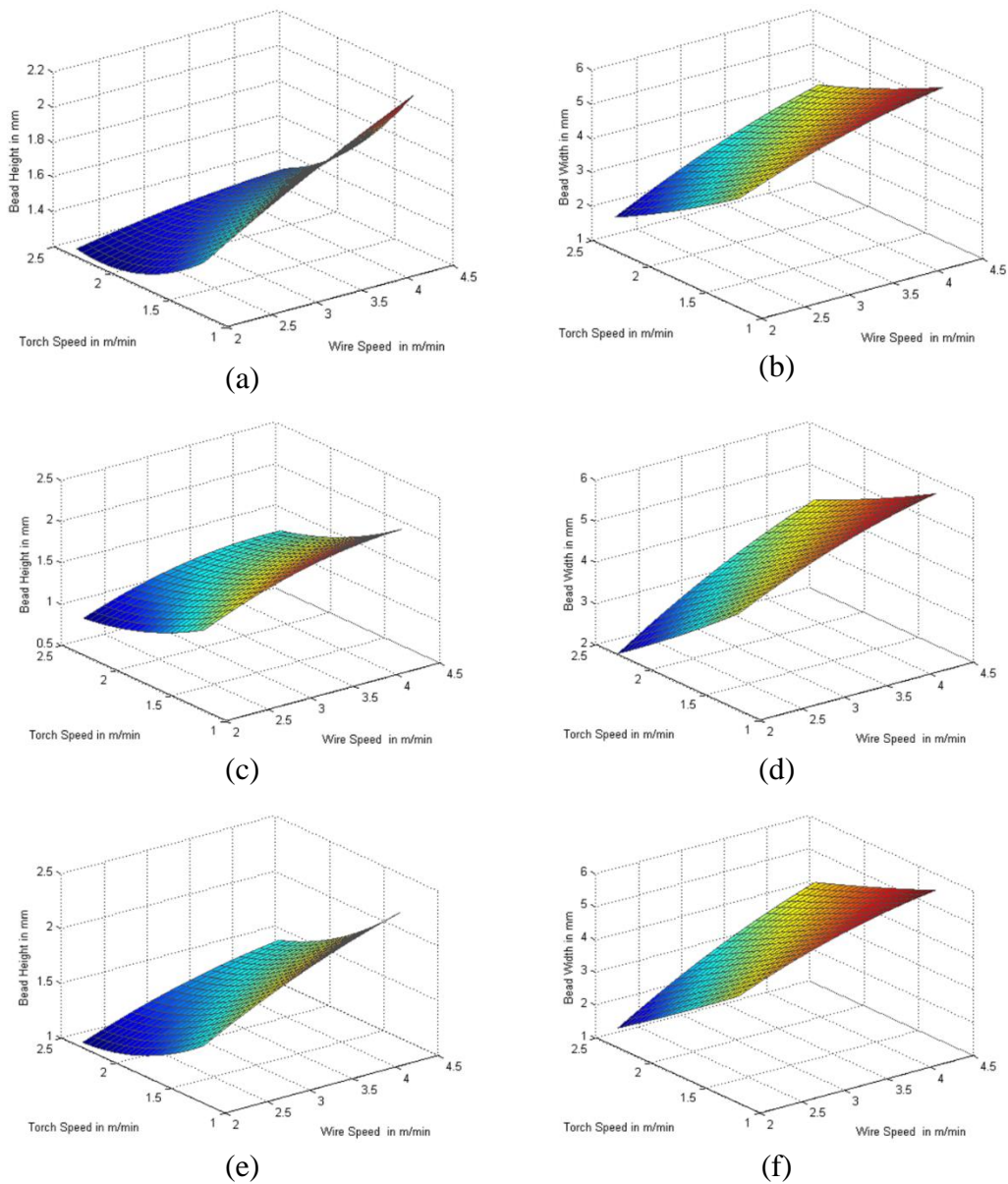


Figure 4.9. Surface plots of weld bead shapes (a)-(b) ER70S-6+ER70S-6 (c)-(d) ER110S-G+ER110S-G (e)-(f) ER110S-G+ ER70S-6.

4.4 Effect of deposition conditions on hardness

Twin-wire process has been popular and well established for joining applications for which it was primarily developed. The current research adapted the same process for metal deposition/cladding than just joining. However, as it is used for metal deposition of a layer in Additive Manufacturing, its context of application being different, the effect of deposition parameters have to be freshly looked into. The crucial difference between traditional welding and weld-deposition is the multiple (and numerous)

number of passes and changing direction of the weld-deposition. Hence, the following considerations were looked into:

- i. Thermal steady-state conditions
- ii. Effect of torch direction
- iii. Effect of number of overlapping beads
- iv. Hardness variation along the cross-section of weld bead

4.4.1 Thermal steady-state conditions

Considerable amount of heat is generated during the weld-deposition process, which leads to the heating up of the base plate. Hence, the base plate temperature at the beginning is quite different from the temperature after a couple of weld-deposition passes. After a certain time, the heat added by weld-deposition equals the heat loss due to conduction and convection and further temperature change occurs in the base plate. The identification of this point helps in establishing the thermal steady-state condition thus enhancing the repeatability of the process.

Nine parallel weld-deposition beads of 120mm each for each combination of filler wires were deposited on a plate of 160mm x 160mm x 10mm at wire speed and torch speed values of 3.5m/min and 1.5m/min respectively. This set of experiments was repeated for three times as shown in Figure 4.10 (a)-(i), to minimize error. These weld beads were cut cross-sectional and polished using emeries of grit size of 180, 360, 600, 1200, 1500, 2000 before the final diamond polish of 12 μ , 6 μ , and 1 μ . They were then cleaned using ethanol solution. Subsequently, the micro-hardness of the cross-section of the weld beads were measured, as tabulated in Table 4.10.. Figure 4.11 plots the hardness value of each bead with one presenting the first weld-bead (deposited on a base plate at room temperature) and the subsequent beads being done on the base plate undergoing gradual heating. As can be inferred from the figure, the first three weld beads have high hardness values and it then gradually stabilizes for the subsequent six beads. Hence, the thermal steady-state during experimentation (and a replication of the layered deposition scenario) can be achieved after the first three beads.

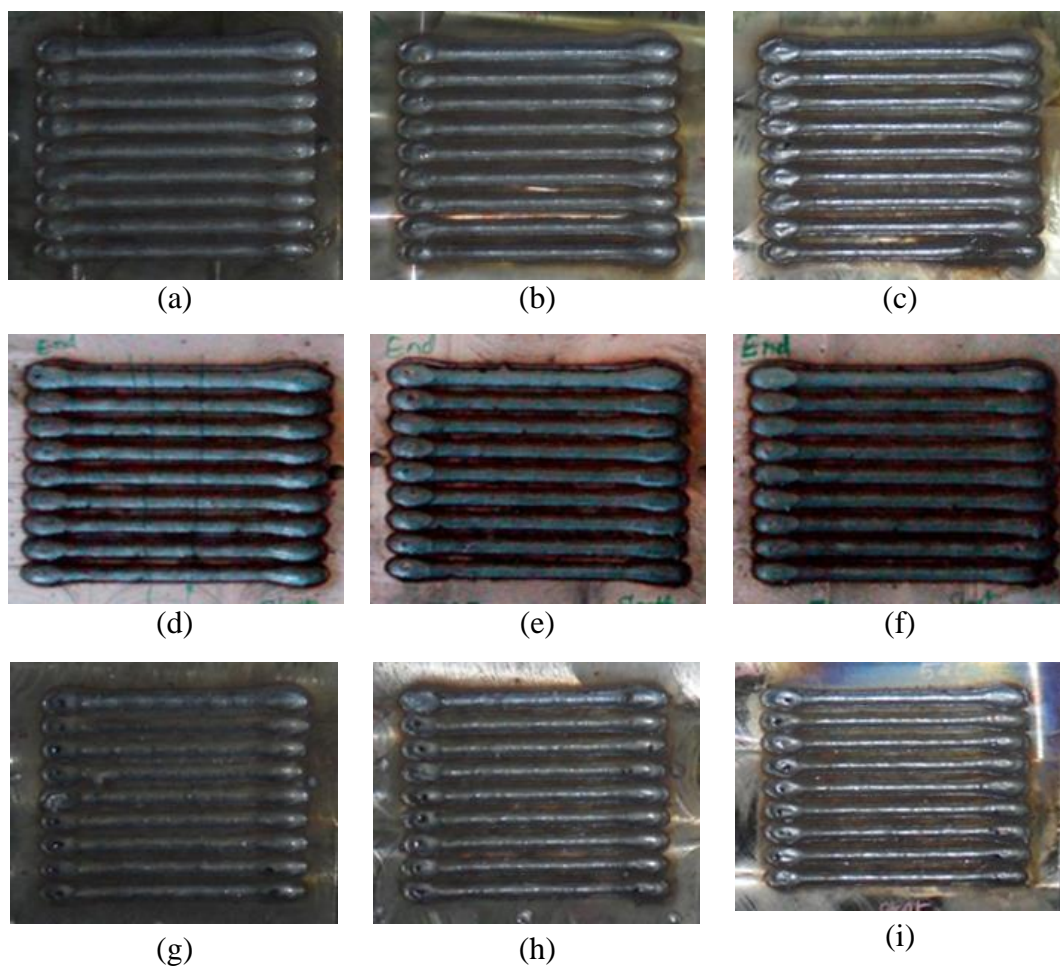


Figure 4.10. Identifying steady state condition of hardness values (a)-(c) ER70S-6+ER70S-6 (d)-(f) ER110S-G+ER110S-G (g)-(i) ER110S-G+ER70S-6.

Table 4.10. Hardness values of steady state condition for three combination of two filler wires.

Sl	Wire speed in m/min		Weld Bead order no	Hardness values in HV		
	Nozzle-1	Nozzle-2		ER70S-6+ER70S-6	ER110S-G+ER110S-G	ER110S-G+ER70S-6
1	3.5	3.5	1	404.33	495.00	452.00
2	3.5	3.5	2	380.00	485.73	430.00
3	3.5	3.5	3	370.00	484.33	425.00
4	3.5	3.5	4	358.73	481.13	418.00
5	3.5	3.5	5	345.27	473.13	420.00
6	3.5	3.5	6	350.00	471.93	422.00
7	3.5	3.5	7	355.00	475.00	418.00
8	3.5	3.5	8	349.00	479.00	417.00
9	3.5	3.5	9	352.00	481.00	421.00

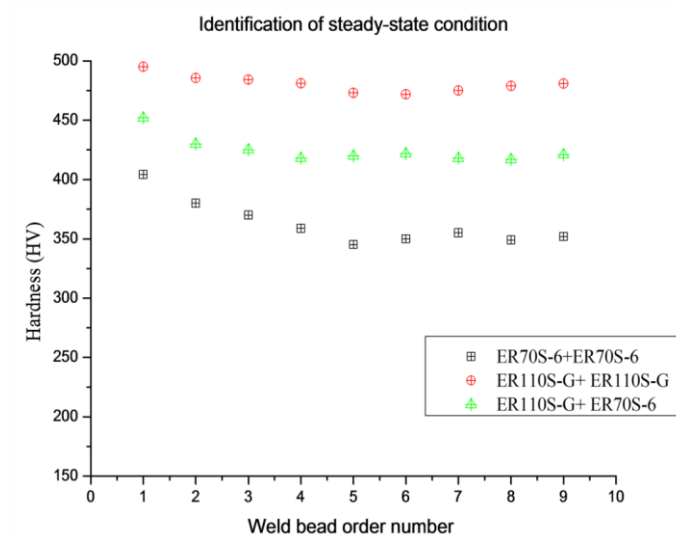


Figure 4.11. Hardness values of deposited weld bead for identification of steady-state condition.

4.4.2 Effect of torch direction

In twin-wire, the direction of the weld-deposition has to be parallel to the filler wires, with one leading and the other trailing. As the leading and trailing wire can be dissimilar, the possible effect of this, if any, on the hardness of the weld-deposition was studied. Experiments were conducted for different torch direction with different wire speeds viz. forward, backward direction. Figure 4.12 shows the representations of direction, wire speed and Figure 4.13 shows the weld beads as deposited in the forward and backward direction. From the last section, it was found that thermal steady-state can be achieved after the first three beads. Considering that, of nine beads first three beads was deposited for pre-heating and steady-state condition and of the remaining six beads, three beads is in forward and backward direction. The measured hardness values are listed in Table 4.11. & Figure 4.14. As can be inferred from Figure 4.14, the torch direction does not have any effect on the hardness of the weld-deposition.

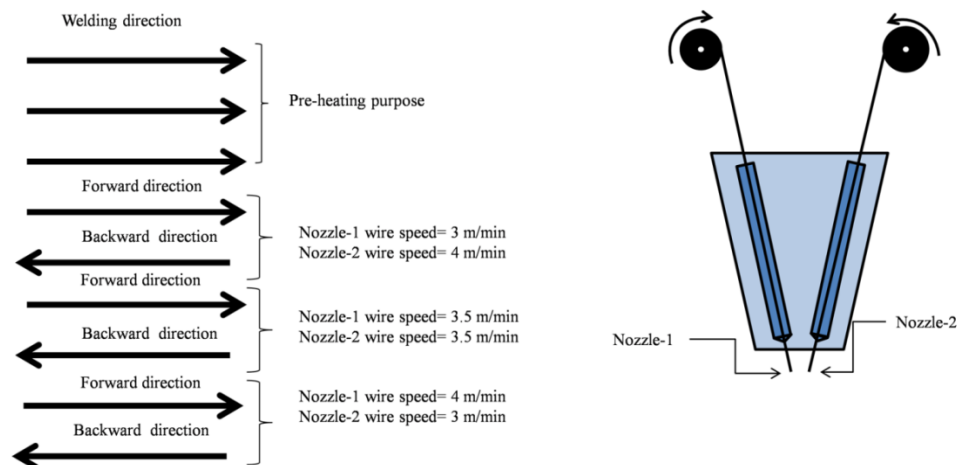


Figure 4.12. Schematic representation of weld torch direction and wire speed.

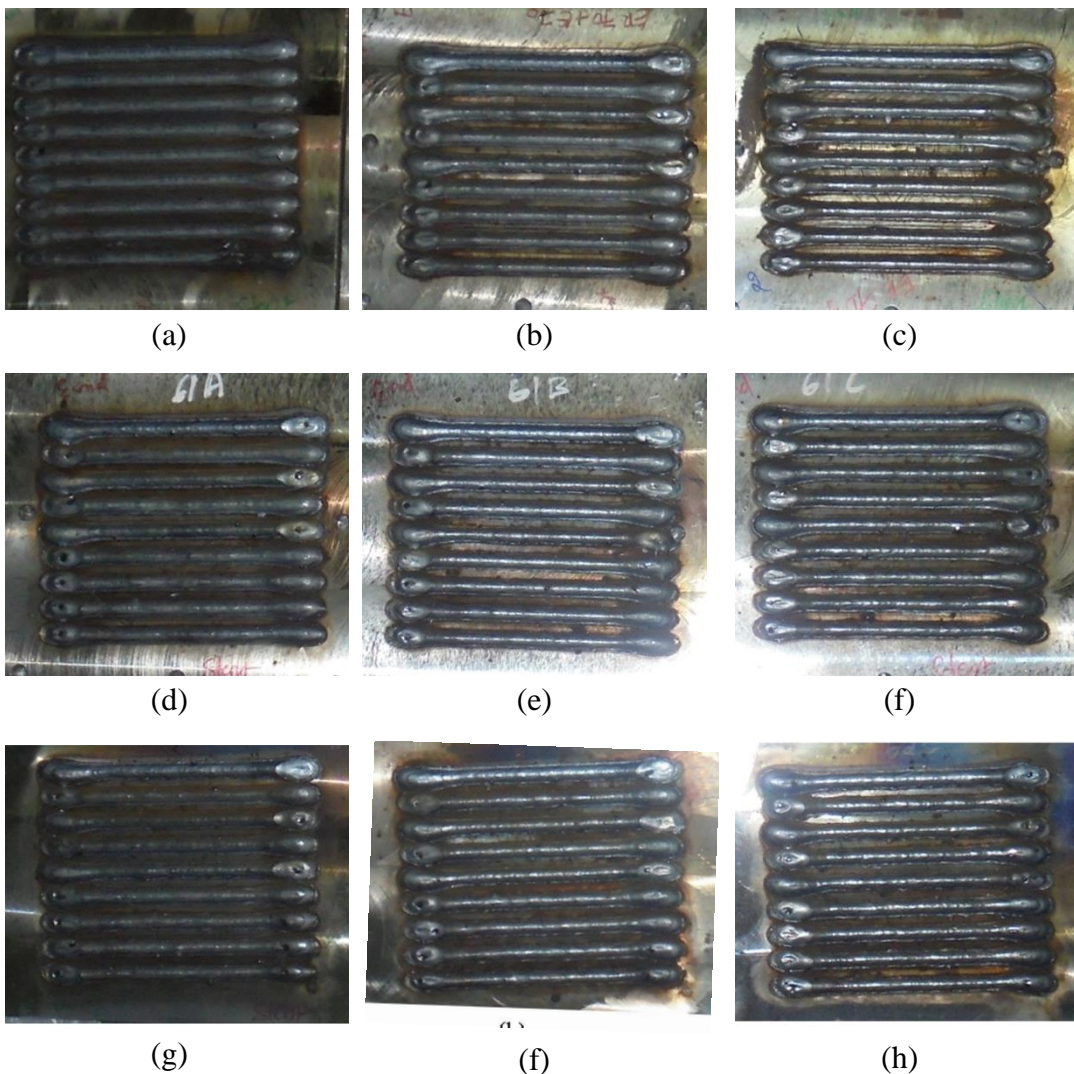


Figure 4.13. Weld bead was deposited in the two directions (a)-(c) ER70S-6+ER70S-6 (d)-(f) ER110S-G+ER110S-G (g)-(i) ER110S-G+ER70S-6.

Table 4.11. Hardness values of different torch direction.							
Sl	Wire speed in m/min		Torch direction	Bead order no	Hardness values in HV		
	Nozzle-1	Nozzle-2			ER70S-6+ER70S-6	ER110S-G+ER110S-G	ER110S-G+ER70S-6
1	3	4	Forward	4	351.00	479.00	420.00
2	3	4	Backward	5	352.00	473.00	419.00
3	3.5	3.5	Forward	6	355.00	475.00	420.00
4	3.5	3.5	Backward	7	351.00	471.00	422.00
5	4	3	Forward	8	351.00	468.00	420.00
6	4	4	Backward	9	354.00	472.00	419.00

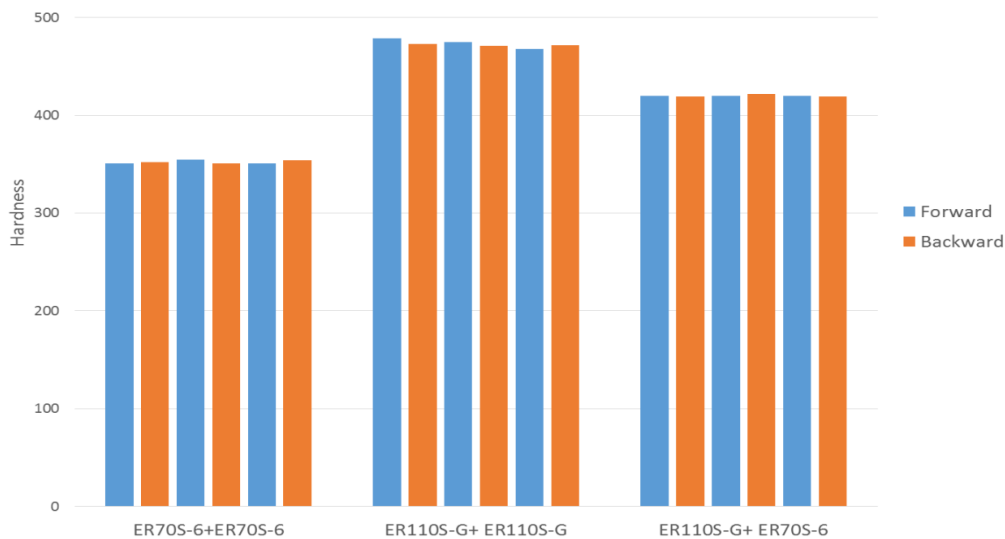


Figure 4.14. Effect of different torch direction.

4.4.3 Effect of bead overlap

One important differentiating factor of weld-deposition from other forms of welding is that weld beads partially overlap with each other. This results in a deposited weld-bead being subjected to another phase of heating and partial re-melting when the next weld-deposition pass is made. Based on the feature size of the layer being deposited, the number of passes to be made may also change; a thin wall for example may need only two passes while a thicker wall may require four passes. Hence, a set of experiments were conducted to find the effect of overlapping weld beads. Figure 4.15 shows the deposited overlapping two, three and five weld beads for three combinations of fillers, with a step-over increment is 3mm. The measured values are listed in Table 4.12. And the corresponding values were plotted in Figure 4.16. From

the figure, it is clear that as a result of partial re-melting, the overlapping beads have less hardness compared to single bead. After three beads, the hardness stabilizes and does not change much. It may be noted that single bead deposition will have higher hardness than overlapping beads and hence must be avoided during area-filling of a given layer. However, a most of the weld-deposition in a layer demand multiple passes deposition, it will not be a severe constraint.

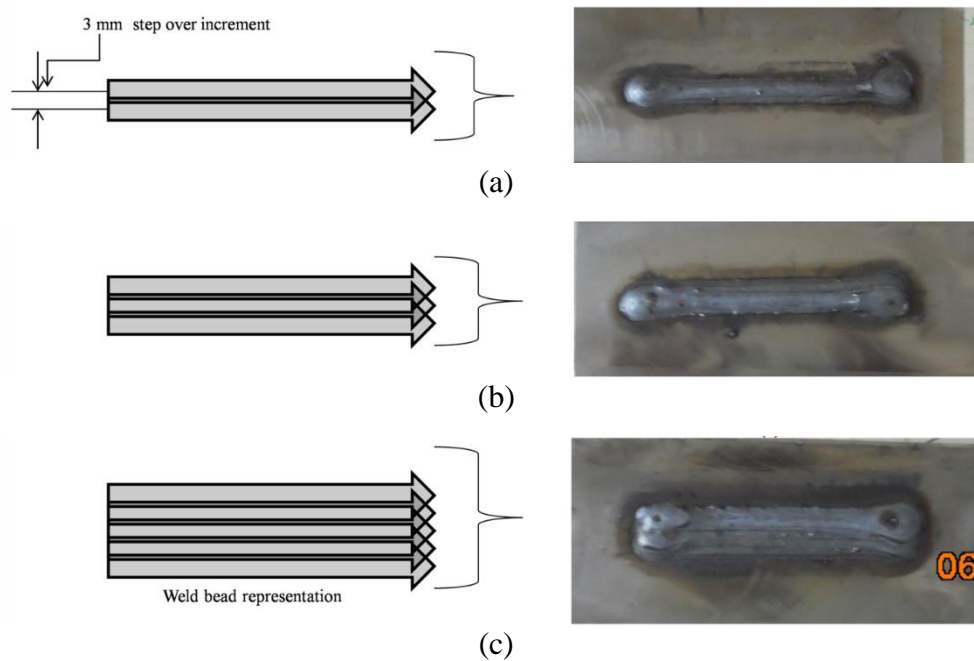


Figure 4.15. Weld beads of (a) Two overlap beads (b) Three overlap beads (c) Five overlap beads.

S.No	Wire speed in m/min		Average hardness values in HV			
	Nozzle-1	Nozzle-2	Single bead	Two beads	Three beads	Five beads
1	3.5	3.5	440.00	300.00	255.00	248.80
2	3.5	3.5	450.00	294.00	249.33	250.60
3	3.5	3.5	450.00	301.00	248.00	249.20
4	3.5	3.5	446.00	292.50	249.67	249.20
5	3.5	3.5	453.00	295.50	251.33	250.80
6	3.5	3.5	452.00	286.50	250.67	248.60

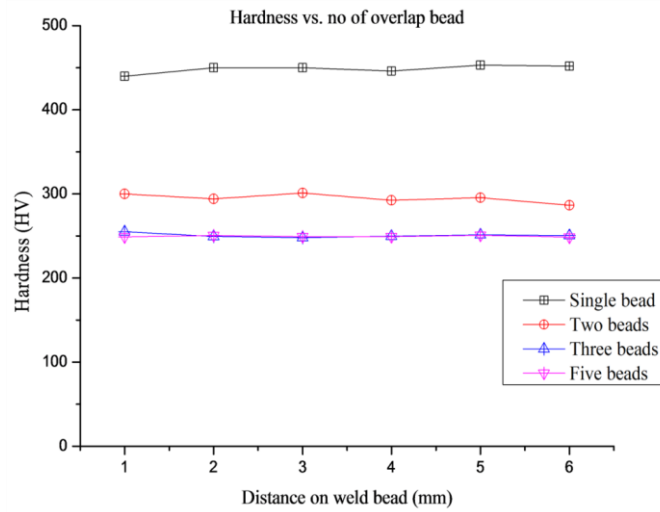


Figure 4.16. Effect of hardness on number of beads deposited of filler wire combination (ER110S-G+ER70S-6).

4.4.4 Hardness variation along the cross-section of weld bead

Figure 4.17 shows hardness variation in cross-section of weld bead along vertical direction, from top surface to bottom or towards base plate. It is observed that there is variation in hardness between base plate and weld bead, especially high hardness is found in HAZ, values listed in Table 4.13. However, there is negligible variation within the weld bead. Hence, hardness variation within the bead is neglected, and top of weld bead can be milled at any location for subsequent layers.

Distance from top of weld bead (mm)	Hardness (HV)
0.2	325
0.4	319
0.6	310
0.8	320
1.0	320
1.2	320
1.4	320
1.6	443
1.8	327
2.0	255
2.2	212
2.4	181
2.6	181
2.8	181
3	180
3.2	183
3.4	184

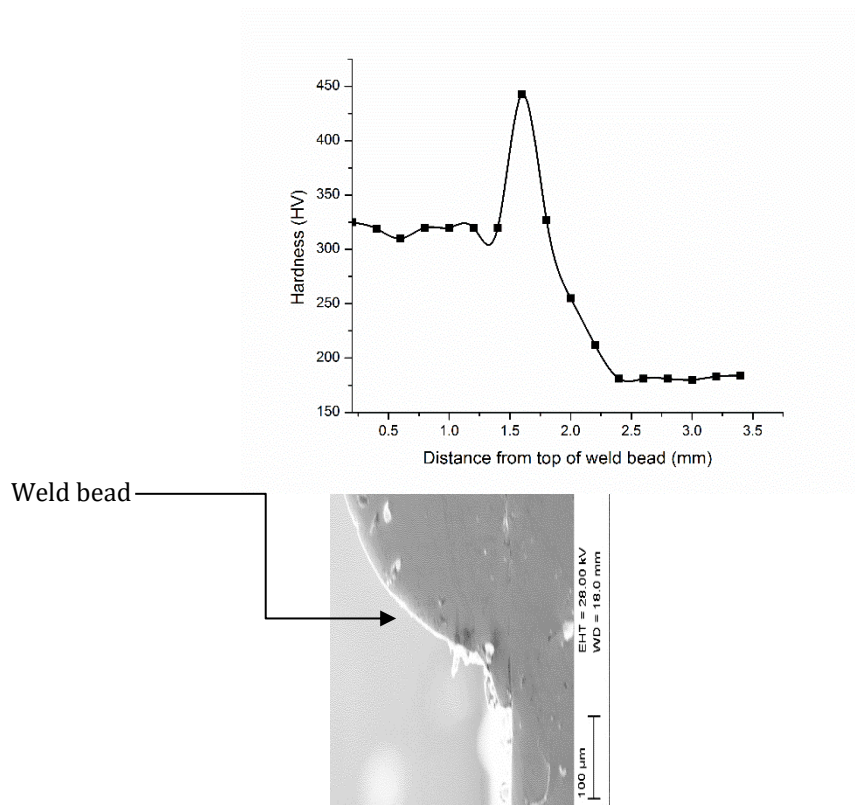


Figure 4.17. Hardness variation along cross-section of bead in vertical direction.

4.5 Summary

The operating range of the process parameters viz., current and torch speed for the three possible combinations of the filler wires have been determined and the feasible working region obtained from the same.

Earlier work on weld bead cross section suggests it follows a parabolic profile with the optimal step-over increment being two-third of the weld bead width. Experimental investigation of the weld-bead cross section for various values of wire and torch speeds confirmed the suitability of this model for twin-wire deposition. A second degree regression model was also computed for predicting weld bead width and height as a function of wire speed and torch speed.

Criterion for adopting the twin-wire process from joining to metal deposition/cladding has also been studied. It is found that during weld-deposition of multiple passes,

thermal steady state is reached after three weld-beads. Although in dissimilar twin-wire welding, the leading and trailing may be different for forward and backward torch direction, it was found that the torch direction does not have any effect on the hardness of the weld-dead deposited. The number of overlap beads is observed to have an effect on the hardness with single beads having higher hardness than overlapping multiple beads. This is due to another phase of heating and partial-re-melting taking place when the next weld-deposition pass is made. Hardness variation in cross-section of weld bead along was measured. It was observed that there is variation in hardness between base plate and weld bead. However, there is less variation is occurred within the weld bead. Hence, hardness variation within bead is neglected. These preliminary studies on primary process parameters and secondary operating conditions will provide the basis for realising a gradient material matrix, to be presented in the next chapter.

Chapter 5

Manufacture of Functionally Gradient Objects

5.1 Introduction

In Additive Manufacturing, the components are realized in a layer-by-layer manner by selective addition of material at required location. Thus, programmable control of process parameters for a given position is a crucial component in its implementation. The same is achieved in TWAM with the help of twin-wire gas metal arc welding setup integrated with a kuka robot, as discussed in earlier chapter. The desired position is obtained by the manipulation of the weld-deposition torch which is attached to the robot arm. The twin-wire welding employs two independent power sources to control the proportion of each wire. These are also integrated to the robot controller for a single point control of position and individual deposition rates of the two filler wires.

Figure 3.19 illustrates the various steps followed in the fabrication of gradient objects. In the first step, the CAD model is sliced into 2D layers; the tool paths for the same are then converted to the robot format in the next step. The gradient material deposition is obtained by independently controlling the proportion of two different filler wires in the twin-wire welding setup. ER70S-6 and ER110S-G were the two wires selected for the same as they belong to the same family of steels, but has different hardness and tensile properties. The weld-deposition process parameters required at a given location are archived by calling the corresponding program number. Hence, integration of positional control and process parameters, achieved here with the help of a robot interface is a must in its implementation.

For a given layer, two directions viz., weld-deposition direction (labelled as X-direction) and step-over direction (labelled as Y-direction) are possible. Depending on the nature of the gradient matrix, the program for calling the particular weld-deposition process parameters may be varied accordingly. Figure 5.1 (a) illustrates an

example, where the weld bead having distinct properties is divided into three segments (X- direction) with a corresponding program having the required process parameters being called. Similarly, Figure 5.1 (b) shows that the weld-deposition parameters changing across the step over direction (Y- direction) with respect to the parameter number. It may be noted from the above discussion that knowledge of the right process parameters to obtain the given property (hardness in this context) at a given location is necessary to realize the same. The following sections present the experimental studies done to obtain such a model for predicting material property (hardness) as a function of process parameters.

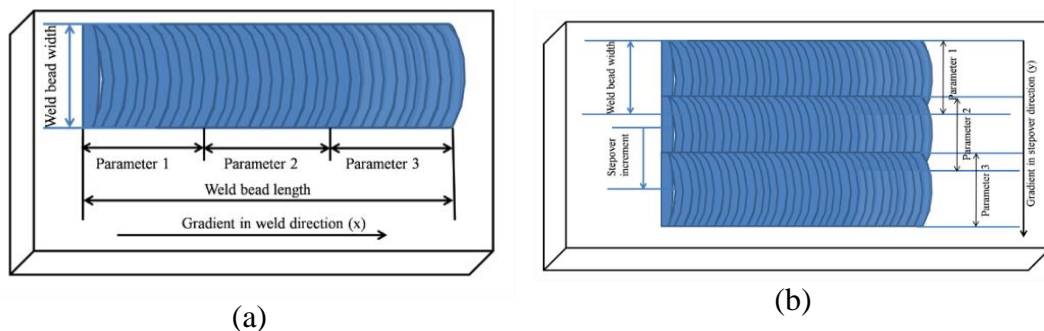


Figure 5.1. Representation of parameter setting for achieving gradient in different directions (a) weld direction, X (b) step-over direction, Y.

5.2 Effect of ratio of filler wires

Different experiments were carried out to study the hardness of weld bead using the following combinations of the wires in each of the welding systems (also indicated in the earlier chapter):

1. Case-1: ER70S-6+ER70S-6
2. Case-2: ER110S-G+ER110S-G
3. Case-3: ER110S-G+ER70S-6

The first two are aimed at obtaining the properties of individual wires; the third is meant for study of the combination of the two. It is expected that the hardness of the combination will be in proportion to the volume of the individual filler wires which in turn is proportional to their wire feed speeds. All other process parameters, except

ratio of the deposition rate of the filler wires were kept constant with the values tabulated in Table 5.1.

Table 5.1. Process parameters used for experimentation.	
Parameter	Value
Wire speed (m/min)	Between 2m/min and 5m/min
Torch Speed (m/min)	1.5
Nozzle gap (base plate to torch) (mm)	16
Shielding gas flow rate (L/min)	12
Shielding gas used	82% Argon+18% CO ₂
Wire Diameter	1.2mm
Filler materials	ER 70S-6, ER110G-S
Step over increment (mm)	3mm

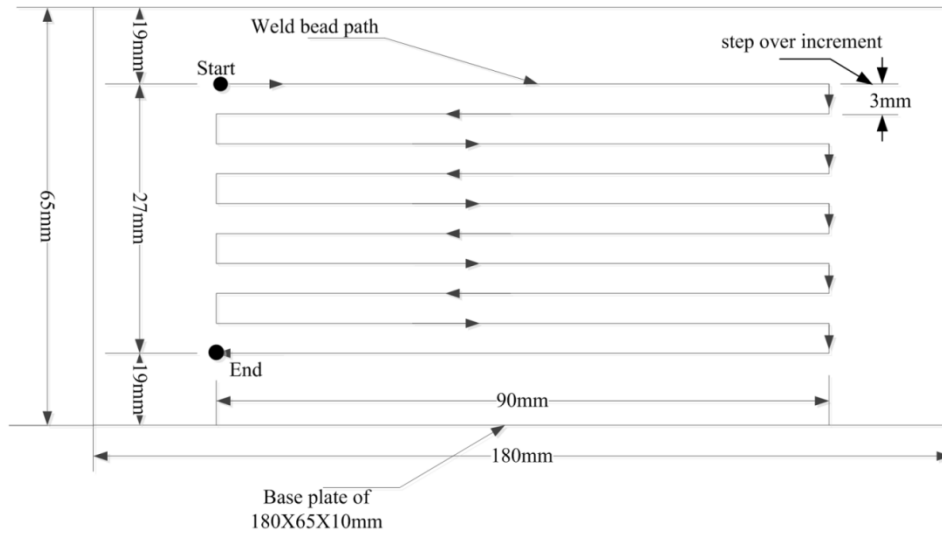


Figure 5.2. Weld-deposition torch path.

Figure 5.2 shows the pattern used in the experiments. Weld beads were deposited on a Mild Steel (MS) substrate of 180 mm X 65 mm X 10 mm for various combinations of wire speed and filler wires. Each combination was repeated three times. Based on the earlier studies on process parameters, the wire speed (feeding speed of the filler wire) was varied from 2m/min to 5m/min (Somashekara and Suryakumar 2014). To maintain uniform deposition rate while realizing a gradient matrix, the combined material deposition rate of the two filler wires was kept constant at 7m/min, while changing their proportion. Therefore,

$$v_a + v_b = \text{constant} \quad (5.1)$$

$$= 7\text{m/min}$$

Where, v_a and v_b are the wire speeds of the two filler wires.

In this study, ten beads with a step over increment of 3mm were deposited. The proportion of material deposited from the individual filler wire can be expressed as:

$$\text{Proportion of filler wire } a \text{ out of total deposited material} = \frac{v_a}{v_a + v_b} \quad (5.2)$$

$$\text{Proportion of filler wire } b \text{ out of total deposited material} = \frac{v_b}{v_a + v_b} \quad (5.3)$$

For these three combinations of filler wires, the wire speeds, v_a and v_b were varied from 2 to 5 m/min and 5 to 2m/min respectively. Figure 5.3 (a), (b) and (c) shows the deposited weld beads on rigidly clamped MS plate, EDM cut samples and polished samples respectively.

5.2.1 Effect of rate of melting on hardness

Before going for the dissimilar wires, the property variation for similar filler wires under different parameters was also studied to confirm if they have similar properties under different rate of melting. Table 5.2 and Table 5.3 lists the measured hardness for various combinations of wire speeds.

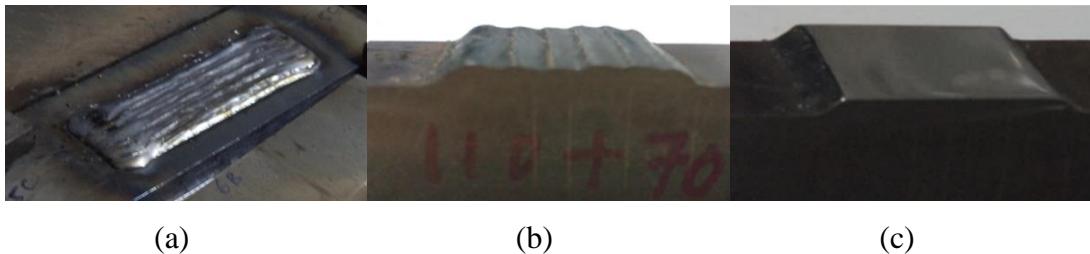


Figure 5.3. (a) Deposited multi weld beads on MS plate (b) EDM cut weld sample after deposition (c) polished sample for micro-hardness testing.

Table 5.2. Measured hardness values for various combinations of wire speeds while using ER70S-6 in both weld-deposition units.				
S.No	ER70S-6 filler wires speed (m/min)		Measured Hardness in HV _{0.5}	Average hardness in HV _{0.5}
	Weld-deposition unit-1	Weld-deposition unit-2		
1	2.0	5.0	198.16	197.95
			195.64	
			200.04	
2	2.5	4.5	202.44	200.76
			197.96	
			201.88	
3	3.0	4.0	196.72	197.40
			196.00	
			199.48	
4	3.5	3.5	199.16	198.68
			198.88	
			198.00	
5	4.0	3.0	198.80	198.60
			197.44	
			199.56	
6	4.5	2.5	195.72	197.55
			197.48	
			199.44	
7	5.0	2.0	196.32	198.92
			199.80	
			200.64	

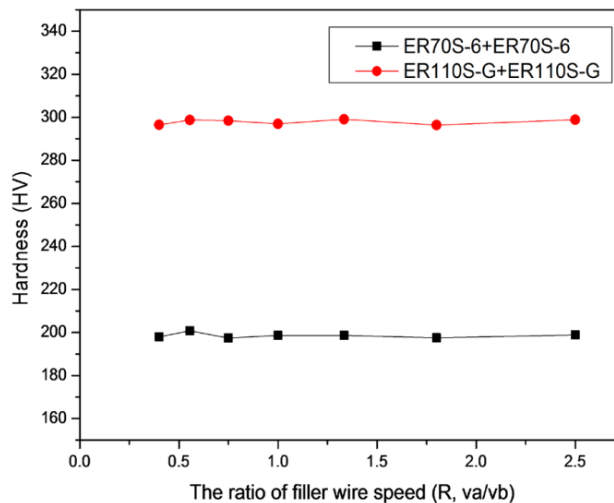


Figure 5.4. Effect on melting rate on the hardness of deposited material. R is the ratio of the wire speeds of the two weld-deposition units.

Table 5.3. Measured hardness values for various combinations of wire speeds while using ER110S-G in both weld-deposition units.				
S.No	ER110S-G filler wires speed (m/min)		Measured Hardness in HV _{0.5}	Average hardness in HV _{0.5}
	Weld-deposition unit-1	Weld-deposition unit-2		
1	2.0	5.0	296.92	296.56
			297.12	
			295.64	
2	2.5	4.5	297.32	298.79
			298.64	
			300.40	
3	3.0	4.0	294.44	298.43
			293.88	
			306.96	
4	3.5	3.5	294.04	296.92
			296.48	
			300.24	
5	4.0	3.0	295.48	299.05
			299.68	
			302.00	
6	4.5	2.5	294.52	296.41
			293.44	
			301.28	
7	5.0	2.0	295.16	298.91
			300.84	
			300.72	

Figure 5.4 shows the average hardness values of the individual filler wires for various values of wire speed. It can be inferred from the Figure 5.4, Table 5.2 and Table 5.3 that the two filler wires exhibit similar properties under different rate of melting. Hence, the individual hardness of each of the filler wires can be taken as below:

$$\text{Average hardness of fully ER110S-G weld bead, } H_{ER110S-G} = 295.14 \pm 9 \text{ HV}_{0.5} \quad (5.4)$$

$$\text{Average hardness of fully ER70S-6 weld bead, } H_{ER70S-6} = 198.19 \pm 8 \text{ HV}_{0.5} \quad (5.5)$$

5.2.2 Effect of filler wire ratio on hardness

While the previous section focused on same filler wires being used in both weld-deposition units, the effect of dissimilar filler wires is presented in the current section.

Experiments were conducted for various proportions of the dissimilar filler wires. The wire speeds of ER110S-G, v_a and ER70S-6, v_b were varied from 2 to 5m/min and 5 to 2m/min respectively. As in the earlier cases, the total wire speed of the combination was maintained at 7m/min to ensure uniform deposition rate. The proportion of the two filler wires can be obtained by using eqn. (5.2) and eqn. (5.3). The values of the hardness measured for these various combinations are listed in Table 5.2 and Table 5.3 .

It is expected that the hardness of the final weld bead is a function of the proportion of each filler wire. In other words, the predicted hardness based on wire speed ratio can be expressed as follows:

$$\begin{aligned} \text{Predicated Hardness, } H &= \\ &= H_{ER110S-G} \left(\frac{v_{ER110S-G}}{v_{ER110S-G} + v_{ER70S-6}} \right) + H_{ER70S-6} \left(\frac{v_{ER70S-6}}{v_{ER110S-G} + v_{ER70S-6}} \right) \end{aligned} \quad (5.6)$$

Table 5.4 shows the comparison of the measured and predicted values of hardness for various wire speed ratios. Figure 5.5 (a) depicts the variation in predicted and measured hardness with respect to filler wire speed ratio and Figure 5.5 (b) shows the scatter plot of the predicted and measured hardness values. From these, it may be observed that the predicted hardness is a function of proportion of each filler wire. Figure 5.6 surface plots the hardness for different wire speeds. These help in the selection of suitable process parameters for a desired hardness at a given location.

Table 5.4. Measured hardness values for various combinations of wire speeds while using dissimilar filler wires.								
S.No	Filler wires speeds (m/min)		Proportion of each filler wire (in %)		Hardness value (HV _{0.5})			
	ER110S-G $v_{ER110S-G}$	ER70S-6 $v_{ER70S-6}$	ER110S-G ref <i>eqn(5.4)</i>	ER70S-6 ref <i>eqn(5.5)</i>	Measured	Average measured	Predicted <i>ref eqn(5.6)</i>	Error (%)
1	2.0	5.0	28.57	71.43	223.00	222.51	226.91	1.92
					221.56			
					222.84			
2	2.5	4.5	35.71	64.29	235.60	235.72	234.01	-0.72
					235.20			
					236.28			
3	3.0	4.0	42.86	57.14	233.08	234.63	241.02	2.72
					234.96			
					235.80			
4	3.5	3.5	50.00	50.00	250.48	250.61	248.13	-1.03
					249.60			
					251.72			
5	4.0	3.0	57.14	42.86	250.52	249.82	255.24	2.14
					249.00			
					249.84			
6	4.5	2.5	64.29	35.71	264.20	264.31	262.35	-0.85
					264.16			
					264.40			
7	5.0	2.0	71.43	28.57	258.40	260.81	269.46	3.25
					262.96			
					261.00			

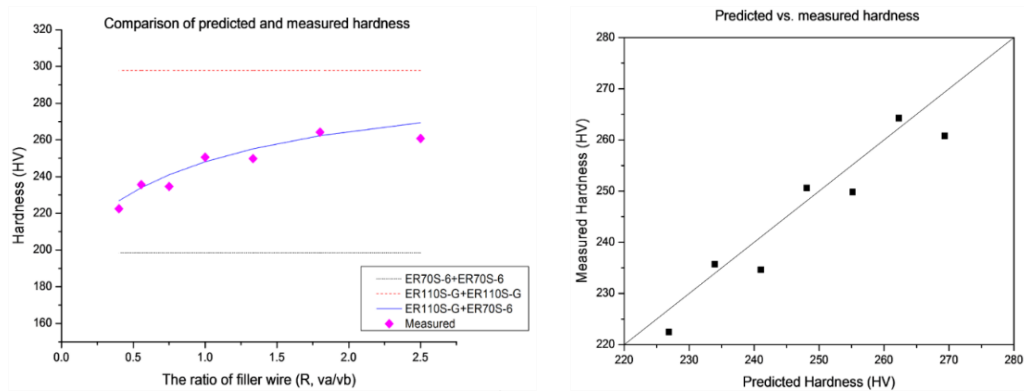


Figure 5.5. Predicted vs. measured hardness values of combination of ER110S-G+ER70S-6 filler wires

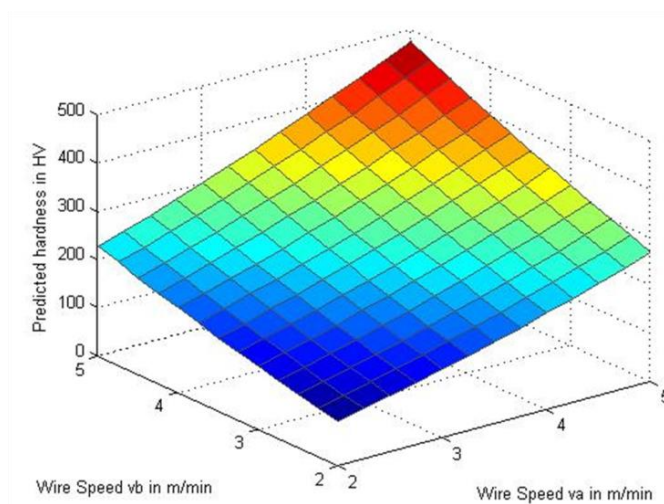


Figure 5.6. Surface plot of hardness for various values of wire speeds

5.3 Fabrication of gradient layers

After the identification of the process parameters required for various values of hardness, the following sample parts were fabricated to demonstrate the concept of realizing FGMs through TWAM:

- (a) One dimensional gradient in step-over direction, Y
- (b) One dimensional gradient in weld-deposition direction, X
- (c) Two dimensional gradient in both step-over and weld-deposition directions, X-Y
- (d) Three dimensional gradient, X-Y-Z.

5.3.1 Gradient in step-over direction

The simplest case of gradient is one in step-over direction where each welding pass will have a particular set of parameters. Figure 5.7 shows the intended sample for such a gradient. It is divided into three regions of 9mm each; the desired hardness of each of these regions is 248.1, 234.0 and 226.9HV0.5 respectively. Each section is 80mm long. The process parameters during the each of these weld-deposition passes can be computed from the hardness model obtained in the earlier section. The wire speed combination for the first three beads comprising the first region will be $v_{ER110S-G} = 3.5\text{m/min}$ and $v_{ER70S-6} = 3.5\text{m/min}$. Similarly, for the next three beads, comprising the second region will be $v_{ER110S-G} = 2.5\text{m/min}$ and $v_{ER70S-6} = 4.5\text{m/min}$ and that of third region with the last three beads will be $v_{ER110S-G} = 2.0\text{m/min}$ and $v_{ER70S-6} = 5.0\text{m/min}$. Figure 5.7 (b) shows the sample prepared in this manner. Figure 5.8 plots the desired

and measured hardness across the step-over direction (Y). The measured values show good match with the desired hardness at that location.

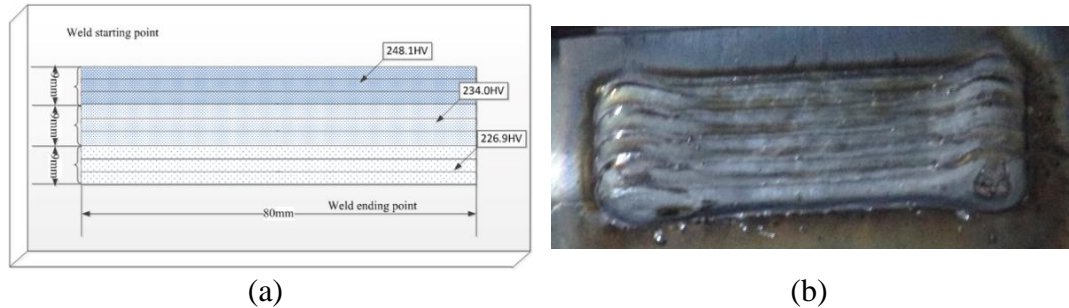


Figure 5.7. One dimensional gradient across the step-over direction (a) representation of desired gradient (b) sample prepared with varying wire speed ratios.

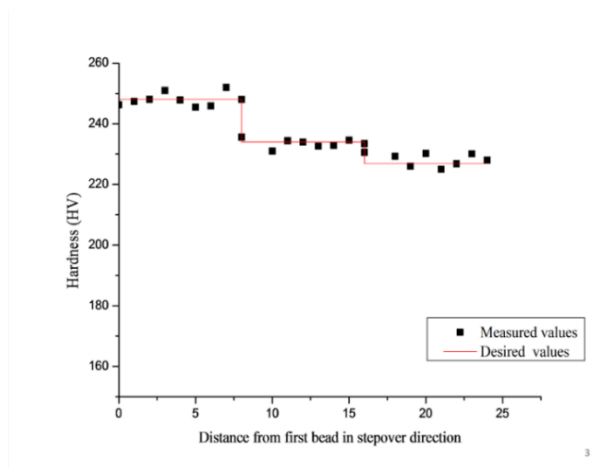
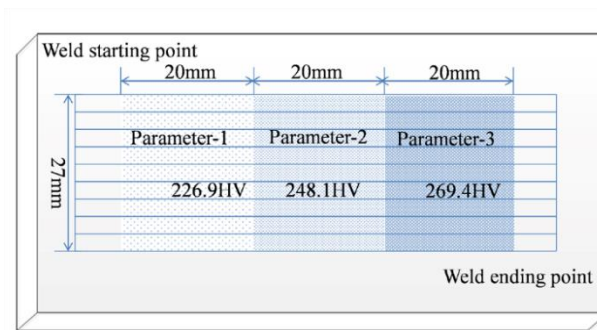


Figure 5.8. Desired and measured hardness along the step-over direction (Y).

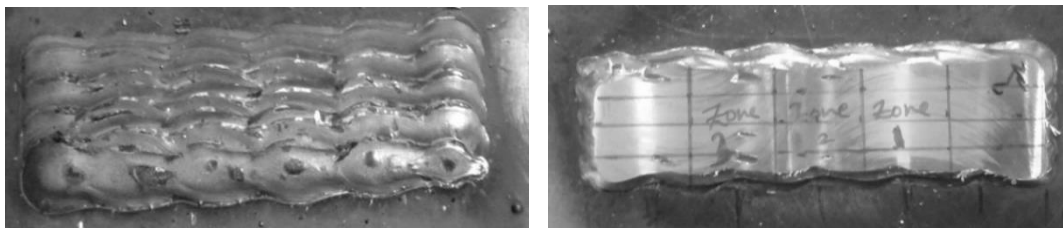
5.3.2 Gradient in weld-deposition direction

To demonstrate a gradient in weld-deposition direction, a sample with three different hardness values in the X-direction was selected. The layer of 120mm x 30mm was prepared using TWAM. In order to avoid the effect of perpendicular welding, the edges were ignored and only the central portion was studied. The central portion was divided into three zones of different hardness viz., 226.9, 248.1 and 269.5HV along X-axis respectively. As the hardness variation is occurring in every weld-bead, a given weld-bead has to be divided into multiple sub-programs and each sub-program representing the particular set of process parameters has to be called from the robot controller. The wire speed combination for the first zone will be $v_{ER110S-G}=2.0\text{m/min}$ and $v_{ER70S-6}=5.0\text{m/min}$. Similarly, for the second zone, it will be $v_{ER110S-G}=3.5\text{m/min}$

and $v_{ER70S-6}=3.5\text{m/min}$ and that of the zone will be will be $v_{ER110S-G}=5.0\text{m/min}$ and $v_{ER70S-6}=2.0\text{m/min}$. This segmentation has to be carried out for each weld-deposition pass, making it more intricate than the earlier case. Figure 5.9 shows the sample prepared in this manner. Figure 5.10 plots the desired and measured hardness across the weld-deposition direction (Y). Although the measured values in first zone shows good match with the desired hardness, the error is considerable in the third zone. This may be due to the transition occurring between zone 2 and zone 3.



(a)



(b)

(c)

Figure 5.9. Gradient in weld-deposition direction (a) representation of desired gradient (b) deposited weld beads (c) polished sample for micro-hardness testing.

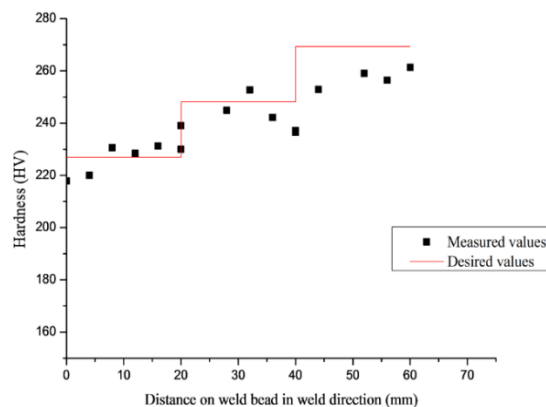


Figure 5.10. Desired and measured hardness along the weld-deposition direction (X).

5.3.3 Two dimensional gradient in both step-over and weld-deposition directions

In the earlier sub-sections, the gradient in step-over and weld-deposition direction was dealt separately. They are combined here to fabricate a layer with hardness varying as shown in Figure 5.11. The two dimensional 80mm x 80mm layer is discretized into 16 square segments of 20mm x 20mm each. The desired hardness and the corresponding wire speeds are indicated in Figure 5.11 (a) and (b) respectively. Figure 5.12 shows the deposited weld bead and the polished layer for measurement of micro hardness. The measured values are compared with the desired hardness in Table 5.5, showing good match between the two. Figure 5.13 shows predicted hardness for varying values of VER_{110S-G} in both the directions plotted together with measured values from the experiments.

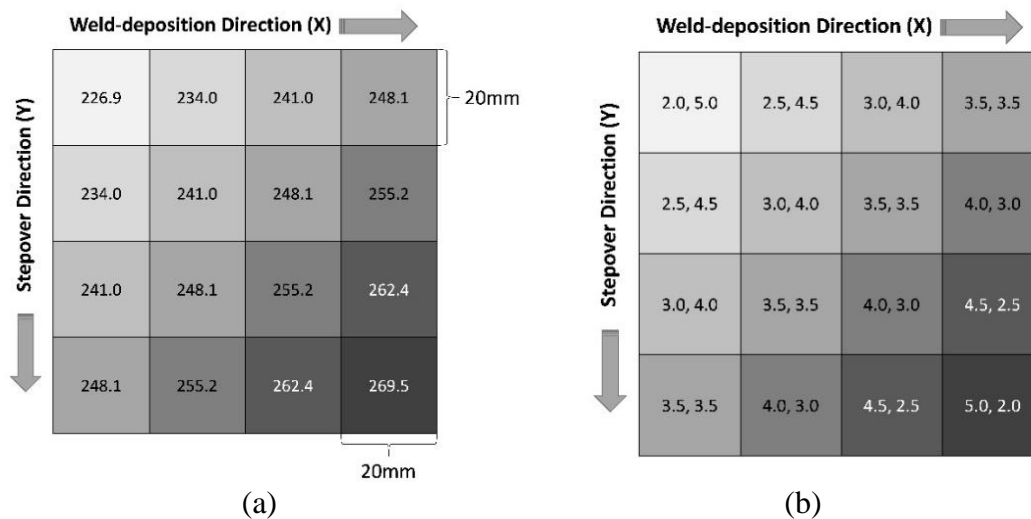


Figure 5.11. Two dimensional gradient in both step-over and weld-deposition directions (a) the desired hardness (b) the wire speeds (VER_{110S-G} , VER_{70S-6}) used to obtain the same.

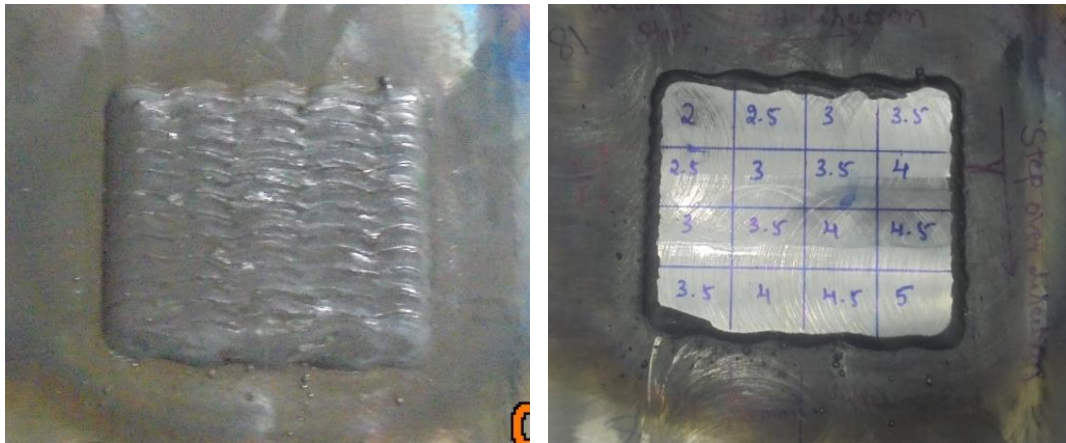


Figure 5.12. Deposited weld beads of two dimensional gradient.

Table 5.5. Hardness values in two dimensional gradients for various proportion of wire speed.

Step-over direction (Y) mm	Weld-direction (X) mm	Hardness (HV)			Error (%)
		Measured	Average Measured	Desired	
0-20	0-20	233.78	228.3	226.87	-0.63
		227.22			
		223.89			
	20-40	228.67	225.15	233.95	3.76
		218.11			
		228.67			
	40-60	239.33	236.78	241.03	1.76
		240.22			
		230.78			
	60-80	247.22	244.56	248.11	1.43
		232.00			
		254.44			
20-40	0-20	241.22	233.74	233.95	0.09
		231.78			
		228.22			
	20-40	244.33	241.41	241.03	-0.16
		240.22			
		239.67			
	40-60	241.11	242.85	248.11	2.12
		244.11			
		243.33			
	60-80	246.56	243.3	255.19	4.66
		234.11			
		249.22			
40-60	0-20	242.33	240.11	241.03	0.38
		238.89			
		239.11			
	20-40	247.67	249.11	248.11	-0.4
		249.00			

		250.67			
	40-60	255.22	255.74	255.19	-0.22
		254.78			
		257.22			
		247.89			
	60-80	249.89	253.19	262.27	3.46
		261.78			
		243.11			
60-80	0-20	237.78	238.93	248.11	3.7
		235.89			
		254.22			
	20-40	244.89	252.22	255.19	1.16
		257.56			
		252.67			
	40-60	254.89	252.33	262.27	3.79
		249.44			
		252.89			
	60-80	256.67	256.3	269.35	4.85
		259.33			

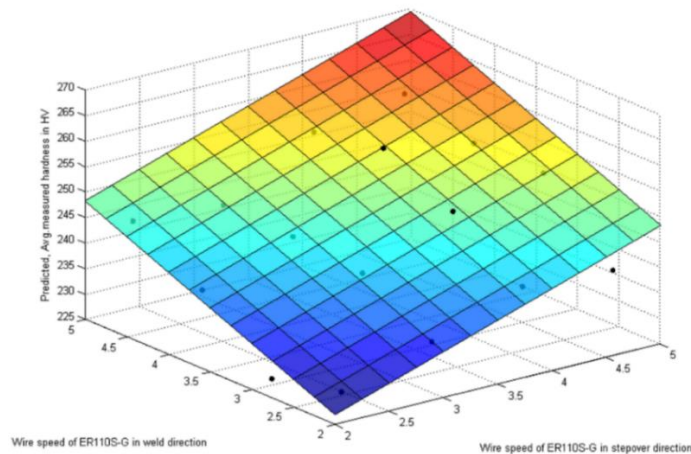


Figure 5.13. Two dimensional gradient of predicted vs. average measured hardness values for various proportion of wire speeds.

5.3.4 Three dimensional gradient

In the earlier sub-sections, the gradient in step-over and weld-deposition direction was dealt separately and continuously. In this section thickness gradient is combined here to fabricate a layer of two dimensional gradient to fabricate three dimensional part with varying wire speed the representation as shown in Figure 5.14. Figure 5.15 shows the steps followed to achieve a rectangular three dimensional object. However, it may be noted that as the actual measurement of internal hardness of this block involves

humongous amount of destructive analysis of each sub components. Hence, it has been presented only as a demonstration part.

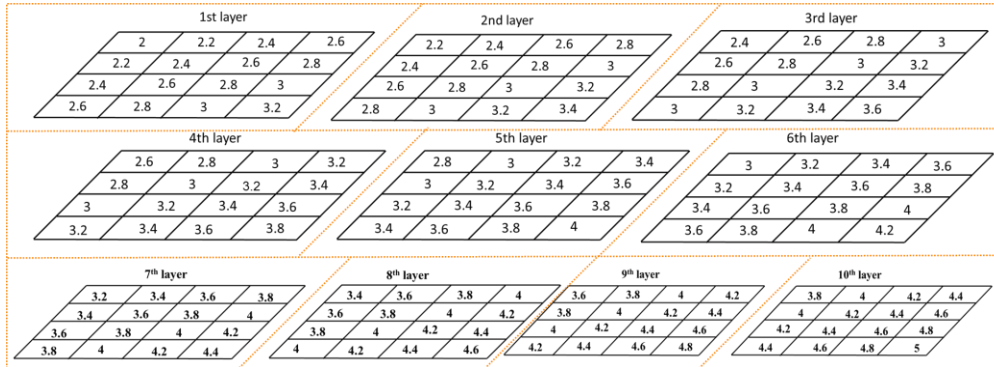


Figure 5.14 Two dimensional layer w.r.t. wire speed



Figure 5.15 Fabrication of three dimensional gradient object

5.4 Applications

Applications of gradient metallic component has high demand in many sectors including and not limited to aerospace, bio-medical, bone replacements, gradient die

tools, automobile parts. In support of this many researchers have successfully demonstrated the application of AM to manufacture the gradient objects using LENS, SLS, etc. listed in the literature survey section. TWAM is also capable of manufacturing gradient objects. Two such cases are illustrated using TWAM process: square hollow shape and die tooling.

Case-1

Figure 3.19 shows steps followed to achieve gradient object. Figure 5.16 shows representation of gradient component of square hollow type (a) the schematic representation gradient layers of square type gradient from inside to out (b) CAD model.

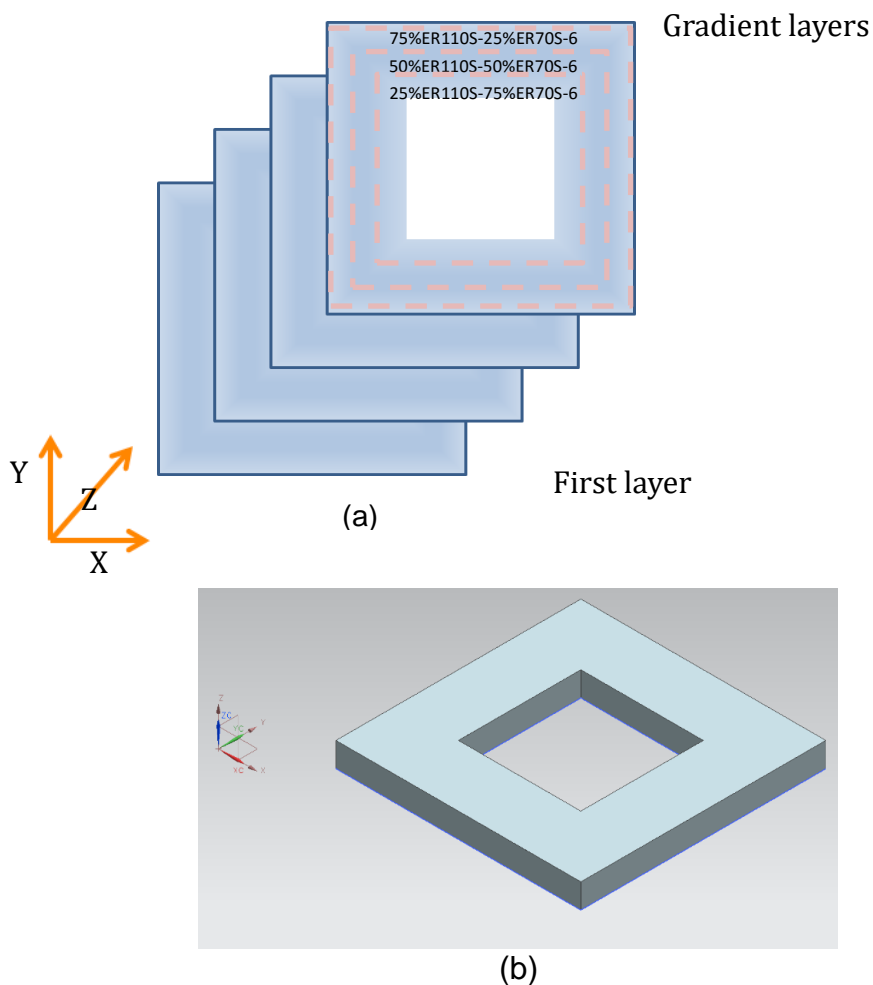


Figure 5.16. Component of gradient (a) Schematic representation of two dimensional gradient layer (b) CAD model.

Gradient deposition was done using the combination of ER110S-G and ER70S-6. The hard outer shell done with 75% of ER110S-G and 25% of ER70S-6 composition. Similarly, the middle part is made up of 50% of each filler wire and inner part with 25% of ER110S-G and 75% of ER70S-6. Therefore, the gradient of the object varies in steps from outside to the inside along the cross section. In other words, the outside of the object or the outer circumference has higher hardness, which gets reduced as we move to the inside of the object or the inner circumference. Figure 5.17 (a) & (b) shows the first layer deposited and the corresponding finished part respectively.

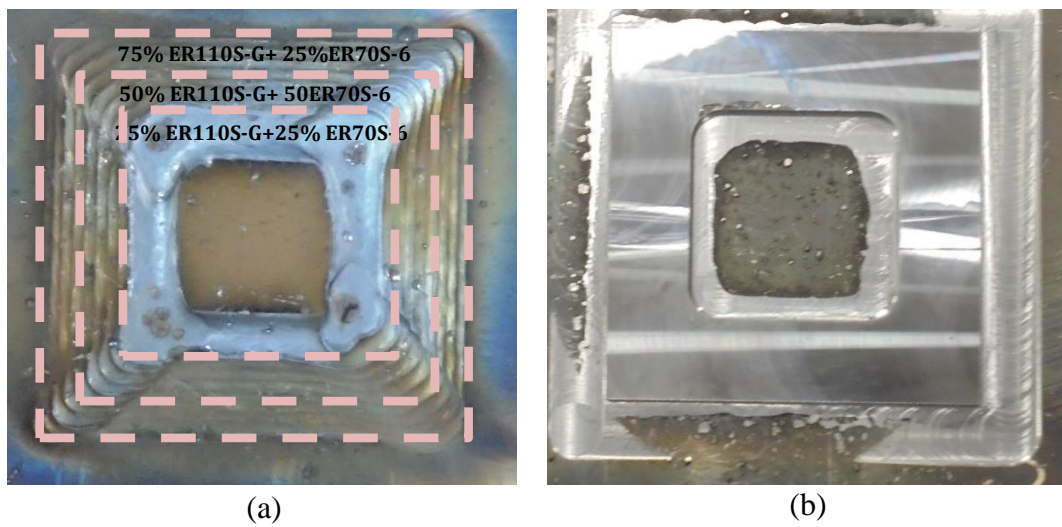
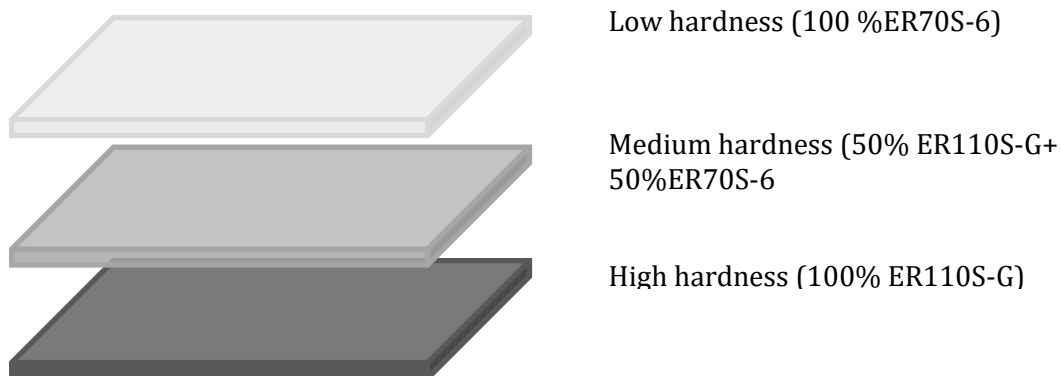


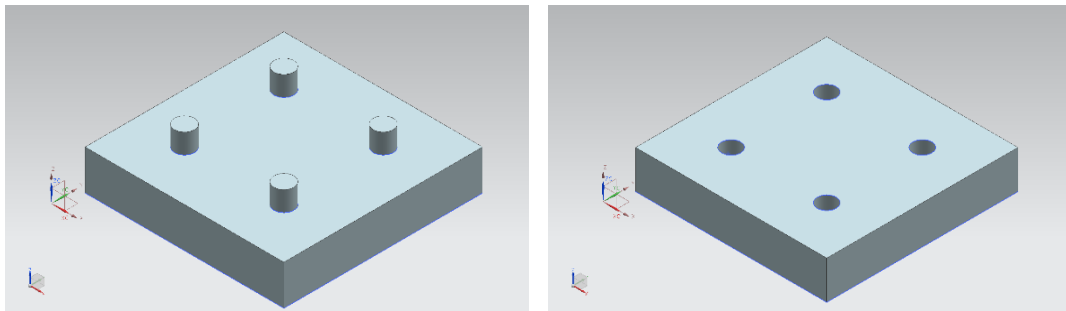
Figure 5.17. Deposited gradient part (a) Sample of first layer (b) Finished part.

Case-2

Figure 5.18 (a) depicts the layers constituting the gradient object of the mold. In this case, punch-cavity pair is designed. Figure 5.18 (b) and (c) show the CAD model of punch-cavity pair. Figure 5.19 (a) shows the layers deposited by 100% ER110S-G and (b) shows the layer after milling process.



(a)



(b)

(c)

Figure 5.18. (a) Schematic representation gradient layers for gradient mold; (b) CAD model of punch-cavity pair.

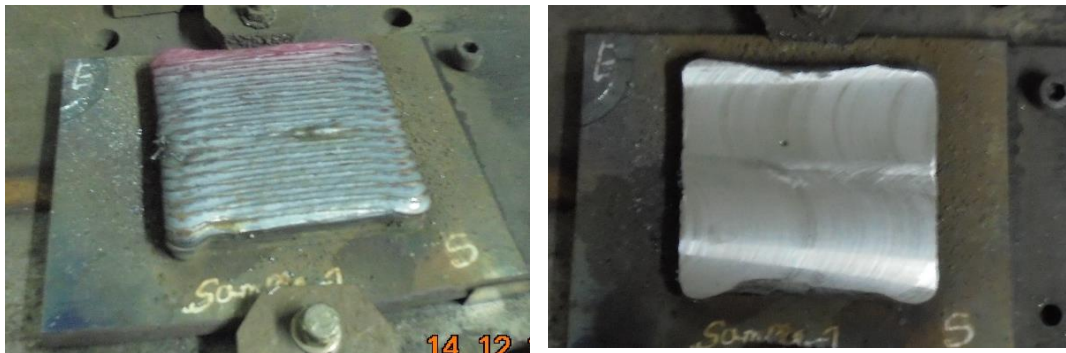


Figure 5.19. (a) Layers deposited by 100% ER110S-G, (b) layer after milling process

The layers forming the cavity area of the dies is deposited by 100% ER70S-6 and therefore, is of lesser hardness. The hardness increases as we move away from the cavity area, where there is a sequential deposition of 50% ER110S-G+50% ER70S-6 followed by 100% ER110S-G resulting in high hardness on the outside of the die. Figure 5.20 shows the finished part of the gradient mold for the punch-cavity pair of a die at two different orientations.

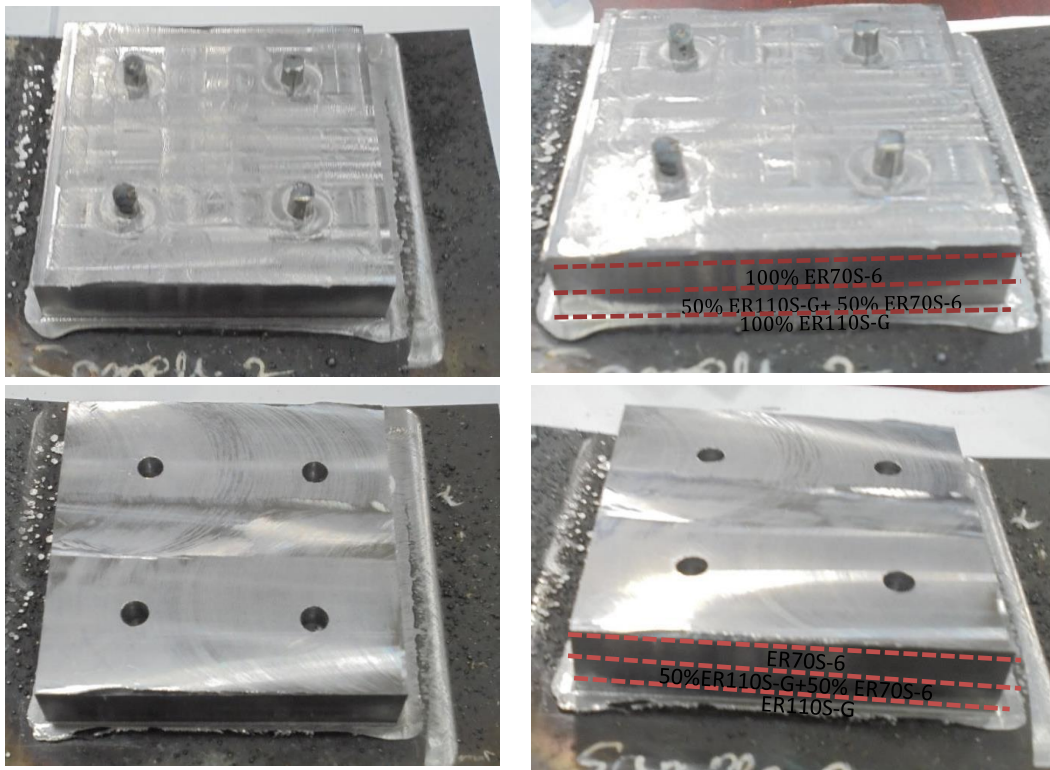


Figure 5.20. Finished gradient mold for the punch-cavity pair of a die at two different orientations.

5.5 Summary

The methodology and various experiments carried out to identify the suitable process parameters at a given location for a desired variation of hardness have been presented. It is found that the individual melting rate of the filler wires does not affect the hardness of the weld bead and it is only a function of the ratio of the amount of material of each deposited (and the wire speed).

Four types of sample parts were fabricated to demonstrate the concept of realizing FGMs through TWAM viz., gradient in step-over direction, in weld-deposition direction, in both the directions and finally gradient in X, Y and Z directions. While the first requires change in weld-deposition parameters across weld beads, the latter two demand modification of process parameters for different sub-sections too. The final three dimensional variation also requires demands such variation to be carried across layers. The fabricated parts showed good match with the desired hardness values for a given location.

Furthermore, to demonstrate the possible applications of TWAM, two illustrative examples were fabricated viz., a hollow square and a punch-cavity pair. These components have hard outer shell and the inner surface of lower hardness with the hardness gradually varying from one surface to the other. As most of the actual applications today assume the fabrication of only a homogeneous material matrix possible, real case studies in FGMs being used are indeed rare. It is hoped that with the new possibilities being opened by AM, designers will be empowered to contemplate more complex parts with varying properties.

Chapter 6

Characterization of Twin-wire Weld-Deposited Objects

6.1 Introduction

Apart from the composition of the materials deposited, owing to the sequential nature of the AM approach, the process parameters also play a role in deciding the properties of the manufactured object. For example the first layer may be subjected to numerous cycles of heating and cooling in contrast to the last layer. These differences in the conditions may also lead to variance in properties and has to be characterized for precise control of the process. Jandric et.al studied the effect of localized heat on microstructure of three dimensional parts through weld-deposition. It was observed that most low carbon steels transition from austenite to ferrite on gradual cooling to room temperature. However, phase change may also be affected by the cooling rate; in the earlier case, if the cooling rate is fast, cementite and ferrite phase will form (Jandric, Labudovic, and Kovacevic 2004). Thijs et.al examined the effect of process parameters and the relation between them and the scanning direction (Thijs et al. 2010). This chapter discusses mechanical and material characterization of parts deposited through TWAM. This is carried out using micro-hardness testing, Optical Metallography (OM), Energy Dispersive X-ray Fluorescence (ED-XRF), Energy Dispersive X-ray analysis (Edax), X-ray diffraction (XRD). The best resolution that can be achieved in the gradience has also been analyzed.

6.2 Experimental analysis for characterization of the specimen

6.2.1 Sample preparation

The commercially stated yield strength - tensile strength of these two filler wires are 490MPa-680MPa and 570MPa-800MPa respectively. While the filler wire ER110S-G is a high strength steel with high alloy composition, ER70S-6 is a carbon steel of normal strength. The difference between the two filler properties is mainly due

difference in Ni, Mn and Mo composition and the effect of these will be discussed in detail in the subsequent sections.

Experiments with various combinations of filler wires, as given below were carried out for the characterization of the process; each combination was repeated thrice to increase the accuracy of the analysis. Based on the earlier studies by the authors on the operating parameters of twin-wire, the wire speed and torch speed values of 3.5m/min and 1.5m/min were found to be optimal and the same were used for current experiments (Somashekara and Suryakumar 2014). These experiments were carried out on mild steel base plates with an step-over increment 3.0mm and 82-18% mixture of Ar+CO₂ shielding gas. The combination of filler wires for analysis are:

1. 100% of ER70S-6
2. 75% of ER70S-6+25% of ER110S-G
3. 50% of ER70S-6+50% of ER110S-G
4. 25% of ER70S-6+75% of ER110S-G
5. 100% of ER110S-G



Figure 6.1. Specimen preparation (a) weld-deposition (b) cross-sectional cut weld specimen (c) a cut-specimen with polished top surface for hardness measurement.

6.2.2 Micro hardness analysis

The specimen for micro hardness testing were prepared through sequential grinding with emery papers of grits 180, 360, 600, 1200, 1500 and 2000 followed by diamond polishing using 9 μ , 6 μ , 3 μ and 1 μ grits. Figure 6.2 & Figure 6.3 shows the indentation and hardness values for each of the above mentioned combinations of the filler wires. As expected, specimen deposited with 100% ER110S-G has highest hardness and lowest hardness was found in the case of 100% ER70S-6. It may be also observed that increase in the ER110S-G ratio proportionately increases the hardness; the reverse is

true in the case of ER70S-6. This also correlates with the finding the earlier chapter where the hardness of the resultant weld bead is in the volumetric ratio of the filler wires used.

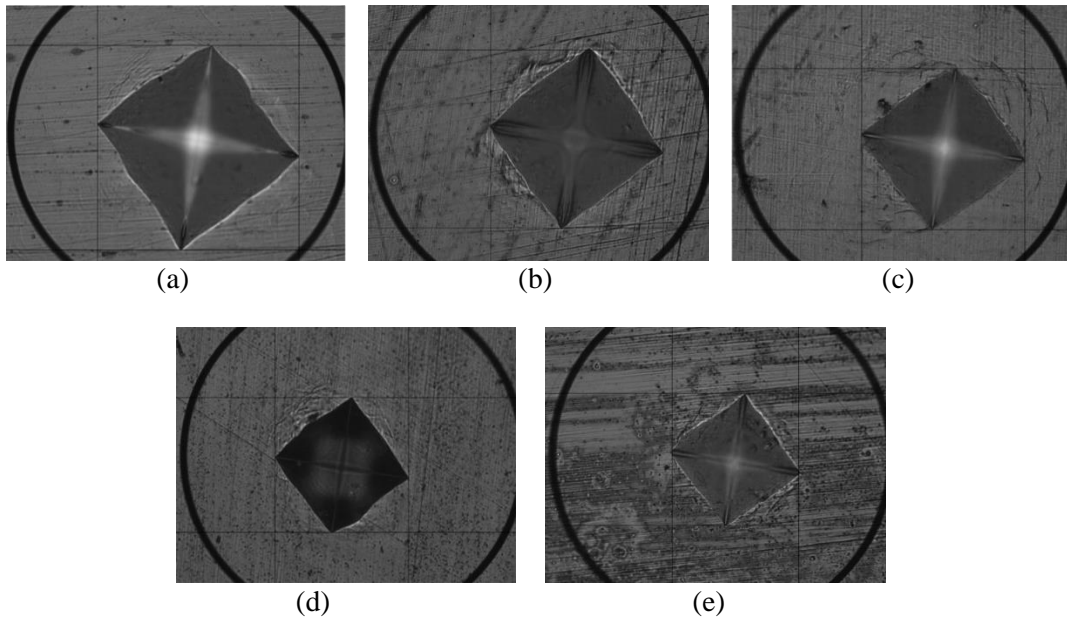


Figure 6.2. Micro-hardness indentations of composition (a) 100% of ER70S-6 (b) 75% of ER70S-6+25% of ER110S-G (c) 50% of ER70S-6+50% of ER110S-G (d) 25% of ER70S-6+75% of ER110S-G (e) 100% of ER110S-G.

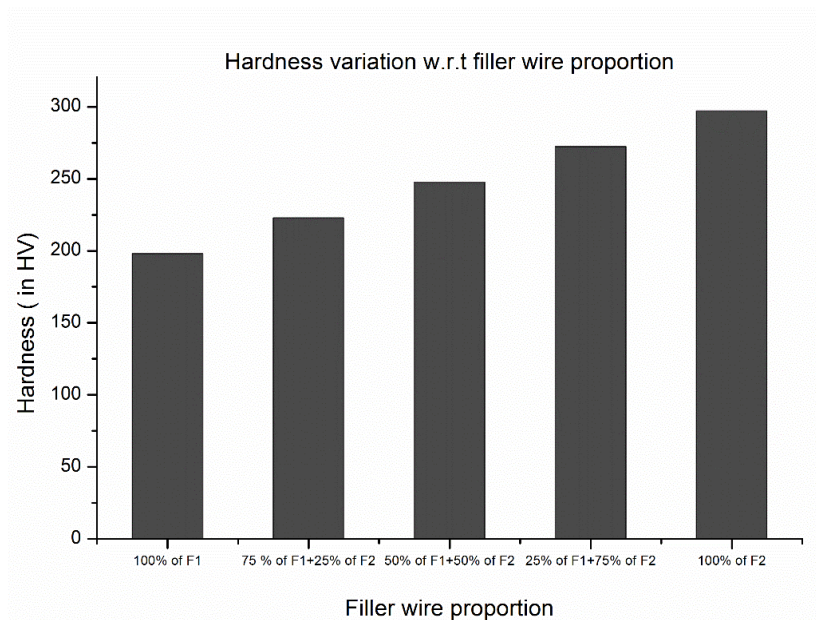


Figure 6.3. Hardness variation with respect to filler wire proportion. F1 and F2 are filler wires.

6.2.3 Microstructural analysis

To facilitate the study of the microstructure, deposited specimen were cleaned in Nitric Acid and Alcohol (Nital) solutions before microstructure analysis in Optical Microscope STM6-LM made by Olympus. Figure 6.4 shows the microstructure of weld beads; the black and white colours in the images being indicative of pearlite and ferrite structures respectively. Figure 6.4 (a) shows the solid solution of ferrite and pearlite which has approximately 80% of ferrite and 20% of pearlite. White color ferrite grains indicate that more amount of ferrite is present, which normally indicates lesser hardness.

Figure 6.4 (b) shows the coarse bainite-ferrite structure was found in deposited part of 75% of ER70S-6+25% of ER110S-G filler wires proportion, the amount of ferrite percentage is less compared to fully deposited ER70S-6. Evidently, when proportion of filler ER110S-G increases, the percentage of alloys will also increase which results in increase in the hardness. Figure 6.4 (c) shows a specimen with combinations of 50% of ER70S-50% of ER110S-G. It reveals a medium grained bainite-ferrite structure. Similarly, in the Figure 6.4 (d) shows the medium grained bainite-ferrite structure with decreasing ferrite composition, in the proportion of 25% of ER70S-6+75% of ER110S-G. Figure 6.4 (e) shows the coarse grained bainite-ferrite structure was formed with 100% ER110S-G filler wire used, in this part the percentage of ferrite composition decreased drastically.

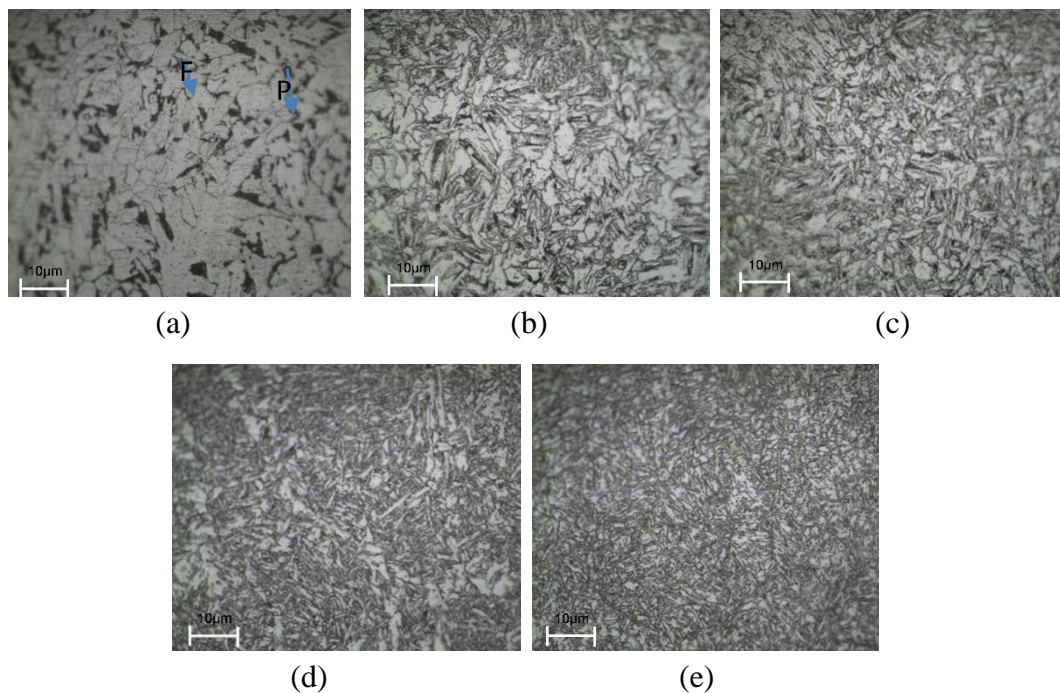


Figure 6.4. Microstructural variation with respect different proportion of filler wire (a) 100% of ER70S-6 (b) 75% of ER70S-6+25% of ER110S-G (c) 50% of ER70S-6+50% of ER110S-G (d) 25% of ER70S-6+75% of ER110S-G (e) 100% of ER110S-G.

6.2.4 X-Ray Fluorescence (XRF) analysis

XRF is a good technique for finding elements present in the unknown sample. The present study focuses on the elements present in the deposited part of various proportions of filler wire with dissimilar filler wires. To find the percentage of each element present in the unknown parts, analysis was done using Epsilon 3^{XLE} EDXRF spectrometer made by PANalytical. Figure 6.5 illustrates the different proportion of filler wire of particular element presented in the component, with Fe, Ni, Mo, Mn, Cu and Cr elements being detected. It was observed as we progress from lower to higher proportion of ER110S-G, the percentage of elements like, Ni, Mo, Mn and Cr also increases, while that of Cu and Fe-balance decreases. Similarly, observation can also be made from XRF spectrums shown in Figure 6.6.

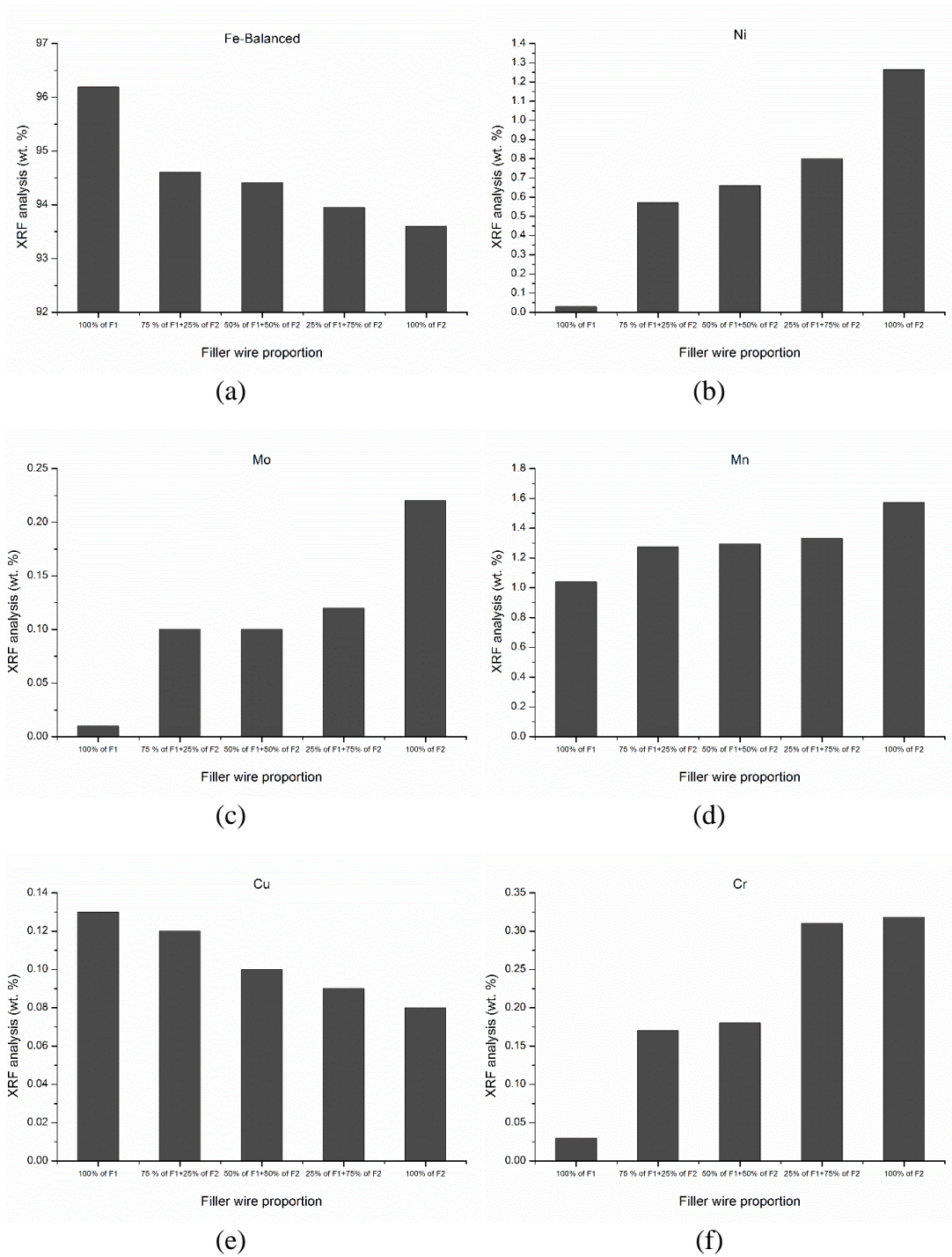


Figure 6.5. XRF analysis of weld-deposited parts of composition of element (a) Fe (b) Ni (c) Mo (d) Mn (e) Cu (f) Cr (F1 and F2: filler wires ER70S-6 and ER110S-G).

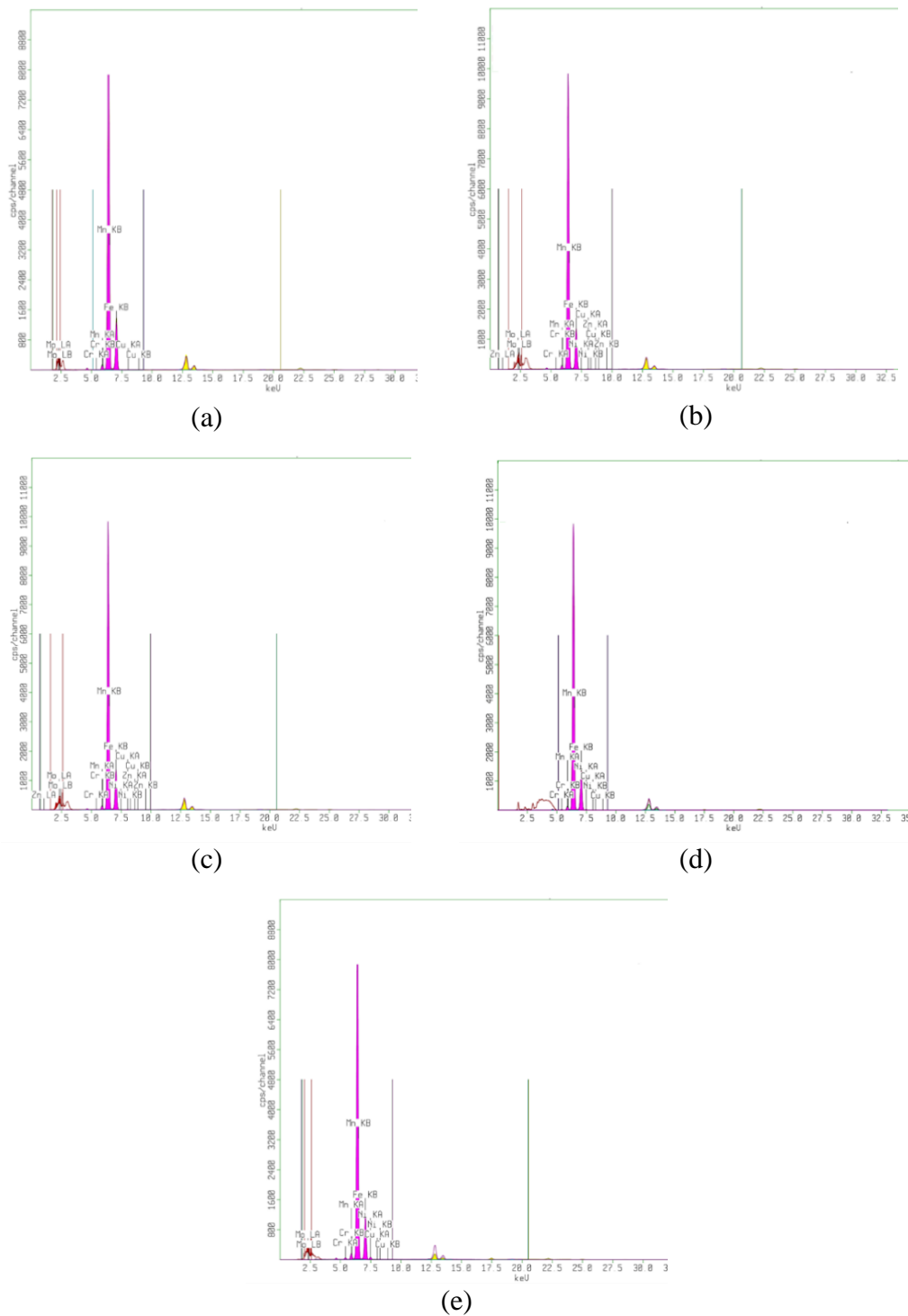


Figure 6.6. X-Ray Fluorescence (XRF) spectrum (a) 100% of ER70S-6 (b) 75% of ER70S-6+25% of ER110S-G (c) 50% of ER70S-6+50% of ER110S-G (d) 25% of ER70S-6+75% of ER110S-G (e) 100% of ER110S-G.

6.2.5 Energy Dispersive X-ray analysis (EDAX)

EDX analysis was conducted using the Oxford EDX equipped Carl Zeiss AG, for quantitative analysis of elements presented in the deposited parts. Figure 6.7 shows

the confirmed values of peaks for Fe and other elements like Ni, Mo, Cu, Cr and Mn present in the deposited parts of dissimilar wires at various proportions. The elemental percentage was found similar to XRF analysis. Hence, only spectra graphs are plotted to avoid repetition.

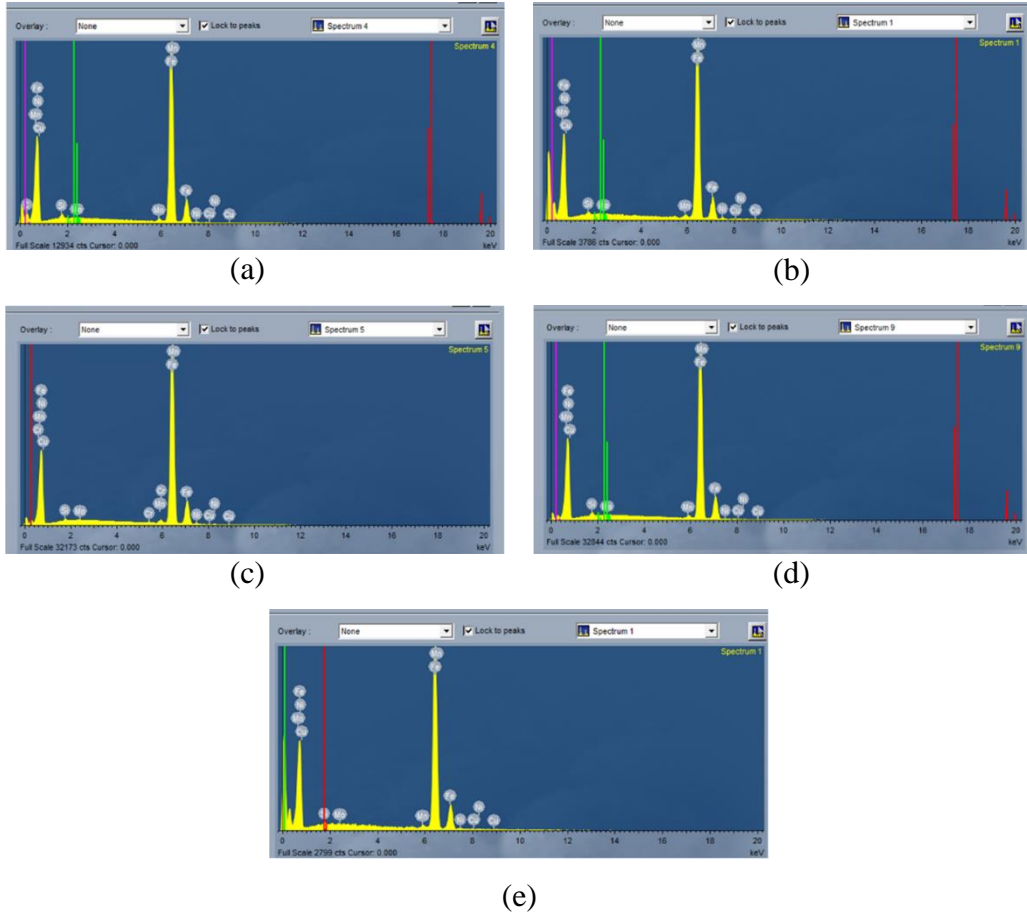


Figure 6.7. Edax Spectra from a different composition part (a) 100% of ER70S-6 (b) 75% of ER70S-6+25% of ER110S-G (c) 50% of ER70S-6+50% of ER110S-G (d) 25% of ER70S-6+75% of ER110S-G (e) 100% of ER110S-G.

6.2.6 X-Ray diffraction (XRD) analysis

X-Ray diffraction is a good technique to identify the phase present in the deposited parts, as the weld bead deposition parts will undergo several thermal cycles and properties changes. Hence, it is very important to understand or identify which phase and composition is present in the deposited parts. Figure 6.8 plots the intensity of different combinations of filler wire proportion. As observed in other cases, here too, for the 100% of ER70S-6 combination, Fe intensity is high and gradually decreases

as we move towards 100% of ER110S-G combination. These results will be studied in detail in the subsequent results and discussion section.

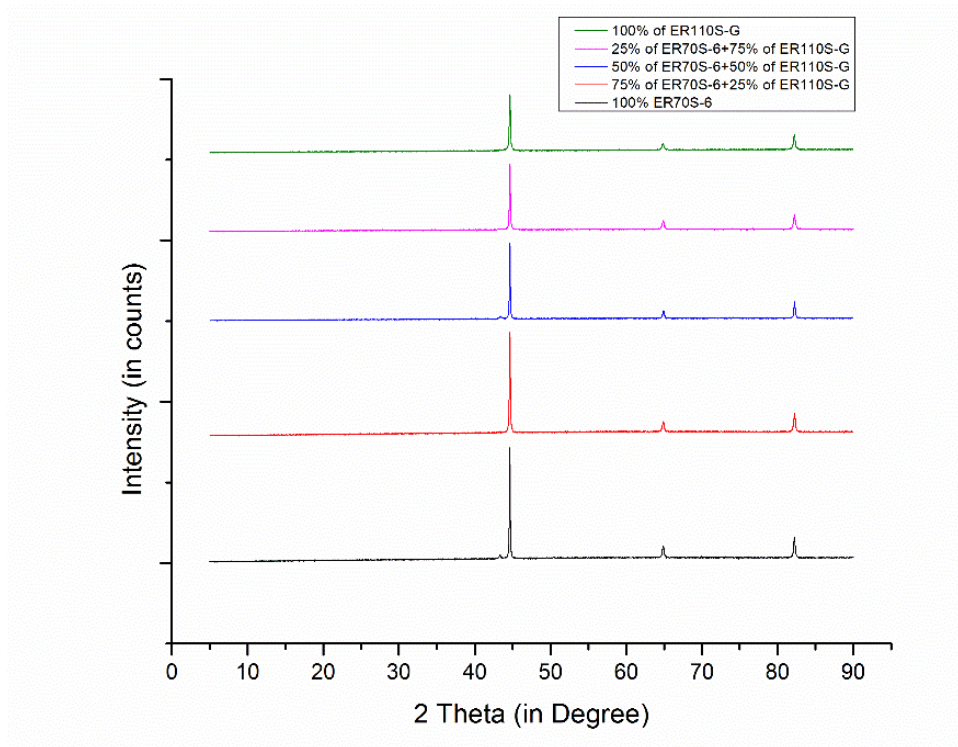


Figure 6.8. XRD phase of different filler wires combinations.

6.3 Results and Discussions

The various set of experimental analysis for characterization of the specimen presented in the above section aims at getting an insight into the development and change of mechanical and characterization, during the twin-wire welding based deposition of different proportions of filler wire with dissimilar wires. The following are some of the observations based on the results of these experiments:

- 1. 100% of ER70S-6:** The hardness of similar filler wire with 100% of ER70S-6 was found to be 198HV. The corresponding microstructure, shown in Figure 6.4 (a) reveals a solid solution of ferrite and pearlite with approximately 80% of ferrite and 20% of pearlite. Bigger the ferrite (white color) grain size, relatively lesser is the hardness, as is so in this case. Black or dark grey color indicates the composite of pearlite, which is present in lesser percentage. From XRF and Edax, it was found that in this particular combination, the percentage

of alloys are less and Fe-balanced element is more. Additionally, from XRD analysis it was also found Fe peak intensity is higher compared to the rest of the peaks shown in Figure 6.8.

2. **75% of ER70S-6+25% of ER110S-G:** A deposited specimen of dissimilar filler wire combination of 75% of ER70S-6+25% of ER110S-G was found to have the corresponding hardness of 222 HV. Figure 6.4 (b) shows the microstructure of the corresponding part, a solid solution of fine bainite-ferrite was formed, in this case the ferrite percentage slightly decreased compared to the previous case. This change is due to addition of the other filler wire of ER110S-G, which changes the structure is slightly due to its high amount of Ni, Mo alloys. Correspondingly Fe percentage decreased and alloys percentage increased, as a result Fe intensity decreased.
3. **50% of ER70S-6+50% of ER110S-G:** For the dissimilar filler wire combination of 50% of ER70S-6 and 50% of ER110S-G, hardness was found to be 247 HV, which indicates that hardness directly increased when the proportion of ER110S-G filler wire increased. The microstructure of corresponding values are in shown in Figure 6.4 (c) it was found that a medium grained bainite-ferrite structure, as the percentage of the alloys(Ni, Mo) increased the percentage of Fe element decreased resulting in decrease in ferrite matrix in structure. Subsequently, Fe intensity decreased as shown in Figure 6.8.
4. **25% of ER70S-6+75% of ER110S-G:** Similarly, in the case of 25% of ER70S-6 and 75% of ER110-G was found to have relatively higher hardness 272HV compared to previous proportions. The microstructure of corresponding values are shown in Figure 6.4 (d). It had medium grained bainite-ferrite and the relative percentage of ferrite matrix decreased. It was observed that as the proportion of ER110S-G increases the corresponding alloys percentage increased and Fe percentage decreased. Also, observed from

XRD peaks the correspondingly Fe peaks are decreased as shown in Figure 6.8.

- 5. 100% of ER110S-G:** A 100% ER110S-G filler condition had a hardness of 297HV; the maximum compared to the previous proportion of filler wires. Figure 6.4 (e) shows the coarse grained bainite-ferrite structure. It was also observed that the ferrite percentage decreased, due to increase in alloy composition. From XRD graphs it was also found that Fe peak was decreased compared to previous part shown in Figure 6.8.

From the above discussion, it was found that hardness of deposited parts is varying in the same pattern as that of the proportion of filler wires. From microscopy analysis, Ferrite-pearlite and Bainite-Ferrite structures were found to be present in the deposited specimens. Ferrite-pearlite microstructure is found to have less hardness and increase in the coarse grained bainite-ferrite structure is observed to have increased the hardness. The percentage of elements like Ni and Mo in the composition, as well as the intensity peaks of the XRD also varied proportionately with the ratio of the filler wires used.

6.4 Resolution of the gradient structure

Gradient resolution specifies the least possible size of gradient pixel or minimum gap required for a changeover from one value to another. It indicates the finest size/feature that can be printed by an additive manufacturing apparatus. It is generally described as the width of minimum possible unit or as the spots per unit length and limited by the nozzle size. Obviously, the higher the resolution, the more spots per unit length can to be printed and the more detailed features can be realized. Thus, resolution plays an important role in the build quality. A higher resolution implies a larger number of printing tracks and more detailed features.

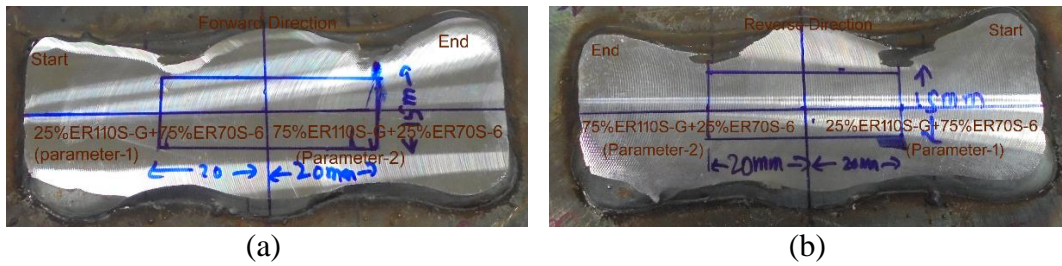


Figure 6.9. Deposited sample of switching over from one welding parameter to another of torch direction (a) forward (b) backward.

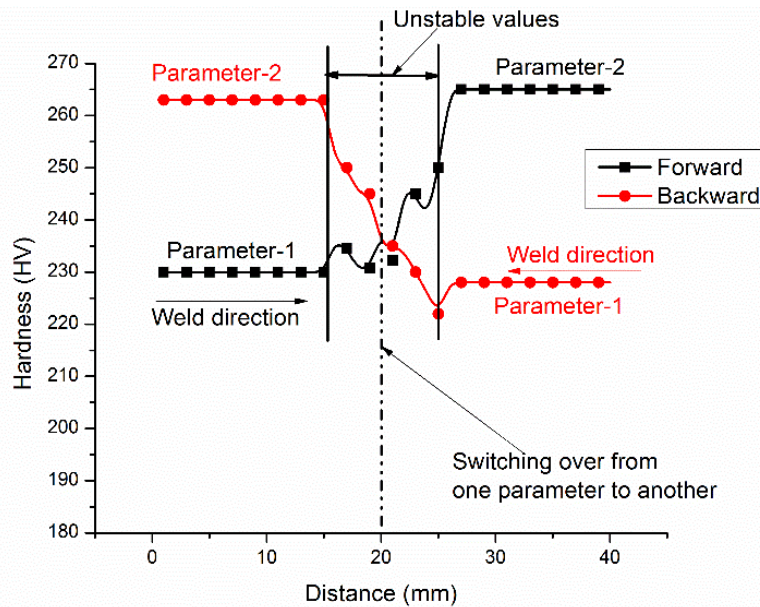


Figure 6.10. Measured hardness variation along the weld-deposition direction with two different weld parameter in forward and backward direction of welding torch.

In order to identify the least possible feature possible, it is important to measure the transition region width while switching over from one parameter to another. To identify the same a pair of experiments with two different parameters, 75% of ER70S-6+25% of ER110S-G, as shown in Figure 6.9 & Figure 6.10 have been carried out. It is observed that there is a transition region between the two set of welding parameters where the hardness values do not follow a predictable pattern. This in other words is gap while switching over from one weld parameter to the subsequent weld parameter. This gap was measured to be ranging between 8-11mm. From this, it can be deduced that a minimum 8-11mm transition gap will can be encountered while moving from one parameter/functional value in the gradient matrix to another.

6.5 Summary

The characterization of objects weld-deposited through TWAM process have been presented in this chapter. Specimen made with five different combinations of filler wires {100:0, 75:25, 50:50, 25:75, 0:100} were used for the analysis. These specimen were examined further by subjecting them to micro hardness, microstructural, X-Ray Fluorescence (XRF), Energy Dispersive X-ray analysis (EDAX) and X-Ray diffraction (XRD) analysis. In all these experiments, the properties were observed to be proportionate to the ratio of the respective filler wire ratios. This also correlates with the finding the earlier chapter where the hardness of the resultant weld bead assumed to be in the volumetric ratio of the filler wires used. This reinforces the hypothesis that the properties of the weld-deposited parts can be controlled in a localized manner by controlling the proportion of the filler wires.

Further on, the width of the transition region while switching over from one set of parameters to another was also investigated. This will help in assessing the best possible resolution of the gradient matrix possible. It was found that a minimum 8-11mm transition gap will can be encountered while moving from one parameter/functional value in the gradient matrix to another.

Chapter 7

FEA Modelling of Twin-wire Weld-Deposition

7.1 Introduction

Residual stresses caused during weld-deposition are a major source of cracks in the fabricated parts. With time, the deposited weld metal contracts. However, the weld is partially prevented by the large adjacent body of relatively cold metal. Hence, leading to residual tensile stresses along the weld (Lin and Perng 1997). Greasley and Naylor found that unrelieved stresses causes specimen distortion during notching resulting in a predominant tensile stress field ahead of the notch tip (Greasley and Naylor 1986). Digiacomo obtained a linear correlation between residual stresses and the elastic deflection within the weld pool and its adjacent base metal of the weldment's members once the constraint forces are released (Digiacomo 1969). Webster and Ezeilo studied the residual stress distributions and their influence on fatigue lifetimes for multi-pass welds (Webster and Ezeilo 2001).

Modelling of the welding process is felt necessary to understand the evolution of the material properties and to better control the thermal and structural characteristics like residual stresses resulting from the process. As such, welding process modelling is highly complex as they are multi-physics simulation involving phase changes. However, either Computational Fluid Dynamics (CFD) & heat transfer modeling of the molten slag or reduced modelling with single phase using equivalent heat source models are usually adopted (Cho et al. 2013; Goldak, Chakravarti, and Bibby 1984). As the focus in the current work is the residual stress evolution in the complete structure, CFD analysis is computationally demanding, hence, an equivalent heat source methodology is adopted to obtain the thermal gradients.

In weld simulations the distribution of thermal gradients depends on two factors: firstly on accuracy of the heat source in representing the melt-pool and secondly on

path of the moving heat source. Numerous heat source equations have been proposed by various researchers for accurate welding simulations (Christiansen, Davies, and Gjermundsen 1965; V. Pavelic, R. Tanbakuchi, O. A. Uyehara 1969; Ghazvinloo and Shadfar 2010; Rosenthal D 1946). Among these, Goldak et al. heat source model which has a Gaussian distribution of power density over a double ellipsoidal geometry is adopted widely in literature for moving heat sources (Goldak, Chakravarti, and Bibby 1984; Rosenthal D 1946).

The material deposition during the process, restricted to solid phase simulations, is implemented using element death-and-birth technique in FE analysis by many researchers (Gery, Long, and Maropoulos 2005; Y Zhang and Chou 2006). The same is also employed in the current work and discussed in detail in the subsequent section.

Multi-pass welding is a key feature which differentiates the weld-deposition for AM from the typical single pass welding often used in material joining. Modeling of multi-pass welding in applications other than AM is limited to a few parallel passes which do not take the area-filling pattern into consideration (Feli et al. 2012; Brickstad and Josefson 1998; Teng, Chang, and Tseng 2003; Deng and Murakawa 2006; Deng, Murakawa, and Liang 2008). Even in such investigations, it was found that the rear pass has the stress release effect on the fore passes and the stress of the last pass plays a significant effect on the residual stress distribution, hence, signifying the importance of the path on the residual stress evolution (Feli et al. 2012). Existing studies on the effect of area-filling for large number of multi-passes has been limited only to experimental finding and/or reduced numerical modelling (Klingbeil et al. 2002). A detailed 3D FEM approach of the same was found lacking. The current study tries to bridge the gap in modeling of pattern dependent weld-deposition for AM, also featuring twin-wire deposition.

Twin-wire welding offers some unique advantages over single wire welding, like higher deposition rates in addition to making it possible to create gradient objects by the use of dissimilar wires. As two different wires from separate power sources go into a single torch in the case of twin-wire welding, its process parameters slightly

differ from those of single wire. Studies on the effect of flux consumption, penetration, heavy corner welds, residual stress in twin-wire was studied by various researchers (Sharma, Arora, and Mishra 2008; Sharma et al. 2009; Janez Tušek 2000; J Tušek 2004). The double ellipsoidal moving heat source modeling of single wire by Goldak et al., can be extended to twin-wire either by superposition of two double ellipsoidal heat sources separated by a distance or combining the two heat sources into an equivalent Goldak heat source while factoring in the arc blow effect (Meng et al. 2005; Sharma et al. 2009; Sharma, Arora, and Mishra 2008; J Tušek 2004; Janez Tušek 2000). In the weld-deposition context of AM, the pattern filling direction changes frequently. Thus, the welding direction need not be always aligned with the twin-wire torch orientation. Hence, superposition approach is preferred over the equivalence approach. As the twin-wire welding was carried out in pulse mode in such a manner that only one arc is active at a given time, the arc-blow effect can be neglected.

7.2 Finite Element Analysis of twin-wire weld-deposition

7.2.1 Governing equations and boundary conditions

Finite Element Analysis (FEA) is a widely used numerical technique for finding approximate solutions to boundary value problems of partial differential equations. In welding application, the magnitude of the heat generated during the deformation is insignificant to that of heat generated by the heat source during welding. Therefore, passively coupled thermo-mechanical approach (i.e. a sequential thermal analysis followed by structural) is adopted. For computing the time-temperature distribution in a non-linear heat transfer analysis, at an initial temperature well above the liquidus temperature, incorporating moving heat source and filler material addition is carried out. Subsequently, the temperature field is used as a thermal load in a non-linear mechanical analysis to calculate the subsequent mechanical effects on the work piece due to thermal strains.

Principle heat conduction equation by Fourier for thermal analysis and the three partial differential equations of force equilibrium for mechanical analysis are used as governing equations.

$$\rho c_p \frac{\partial T}{\partial t} = \frac{\partial}{\partial x} \left(K \frac{\partial T}{\partial x} \right) + \frac{\partial}{\partial y} \left(K \frac{\partial T}{\partial y} \right) + \frac{\partial}{\partial z} \left(K \frac{\partial T}{\partial z} \right) + Q_v \quad (7.1)$$

$$\sigma_{ij,i} + p_j = 0 \quad (7.2)$$

Where T Temperature of the material
 ρ Material Density
 c_p Specific heat
 K Heat Conductivity
 Q_v External volumetric heat supplied into the body
 p_j Body force at any point
 σ_{ij} Stress tensor

At the ambient temperature, convection and radiation are very substantial. Newton's Law for surface convection heat loss and Stefan-Boltzmann's law for radiation heat loss are considered as boundary conditions for thermal analysis. Figure 7.1 & Figure 7.2 illustrate the details of boundary conditions for thermal and structural analysis respectively.

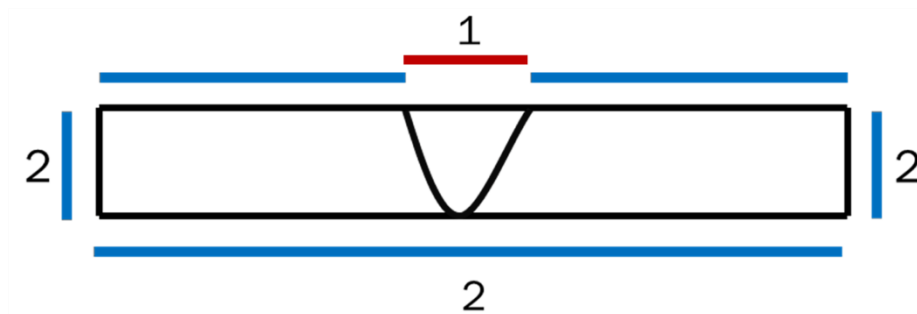


Figure 7.1. Boundary condition for thermal analysis: 1- Heat Source; 2- Convection and Radiation.

According to Newton's law of surface convection, heat loss q_{con} is given by,

$$q_{con} = h_{con} \cdot (T - T_0) \quad (7.3)$$

Where h_{con} Convection heat transfer coefficient
 T_0 Ambient temperature

According to Stefan-Boltzmann's law, the radiation heat loss q_{rad} is given by

$$q_{rad} = \varepsilon \cdot \sigma \cdot ((T - T_Z)^4) - ((T_0 - T_Z)^4) \quad (7.4)$$

Where ε Emissivity constant
 σ Stefan-Boltzmann constant
 T_Z Absolute zero on the actual temperature scale

Materials when uniformly heated (at moderate temperatures less than half the melting point of the solid), regains its original shape after uniform cooling. In weld-deposition process, due to the moving heat source, area adjacent to the latest weld bead will have a higher temperature than that of the rest and hence component experiences non-uniform heating and cooling. The residual stresses in weld-deposition are due to firstly non-uniform heat distribution and secondly the constraining effects from the adjacent structures. The constraining effects can be further sub-divided into elastic and plastic constraints. In substrates, during the weld-deposition, the average temperature was found to be less than one-third of the melting point of the solid. Hence, the major contributions are from elastic constraints and only they were considered in the simulation.

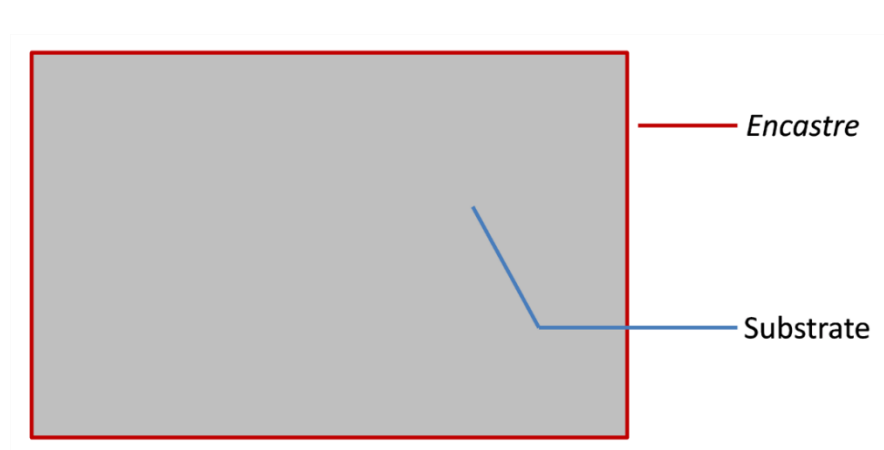


Figure 7.2. Boundary conditions for structural analysis.

Welding, an electric arc, generates approximately 60-70% of the heat energy at the anode and the rest at the cathode. The net heat input (per unit time) is given by the equation (7.5) for a basic welding process:

$$Q = \eta VI \quad (7.5)$$

Where Q Heat Input (W)
 η Arc Efficiency (%)
 V Voltage (V)
 I Current (A)

This basic heat input equation does not fully capture the entire process of arc generation and distribution. Hence, a series of heat source models were put forward in the literature to depict the heat source equation to fit real welding process. Double ellipsoidal heat source model, presented by Goldak et.al. consisting of Gaussian distribution has excellent feature of power density distribution control in the weld pool and HAZ (Goldak, Chakravarti, and Bibby 1984). The heat input is defined separately over two ellipsoidal regions; one region in front of the arc center and the other behind (Figure 7.3). The heat distribution of front and rear quadrants of the heat source of welding arc can be expressed as:

$$q_f = \frac{6\sqrt{3}\eta Q f_f}{\pi\sqrt{\pi}a_f b c} e^{-3\left\{\left(\frac{x^2}{a_f^2}\right)+\left(\frac{y^2}{b^2}\right)+\left(\frac{z^2}{c}\right)\right\}} \quad (7.6)$$

$$q_r = \frac{6\sqrt{3}\eta Q f_r}{\pi\sqrt{\pi}a_r b c} e^{-3\left\{\left(\frac{x^2}{a_r^2}\right)+\left(\frac{y^2}{b^2}\right)+\left(\frac{z^2}{c}\right)\right\}} \quad (7.7)$$

a_r, a_f, f_f, f_r, b, c are characteristic parameters of heat source. As per Goldak et. al., the values of a_f, a_r, b and c can be obtained from shape of the weld bead and molten zone. The recommended estimate for the parameters b and c will be the width and penetration of the weld bead, while those for a_f and a_r will be around one-half and twice the weld bead width. Taking these recommendations into considerations and based on previous studies on the weld-bead geometry, the following values for the parameters are chosen (Adinarayanappa and Simhambhatla 2014):

$$\begin{array}{l|l|l|l} f_f = 0.6 & f_r = 1.4 & \eta = 0.7 & \\ a_f = 3 \text{ mm} & a_r = 9 \text{ mm} & b = 5 \text{ mm} & c = 4 \text{ mm} \end{array}$$

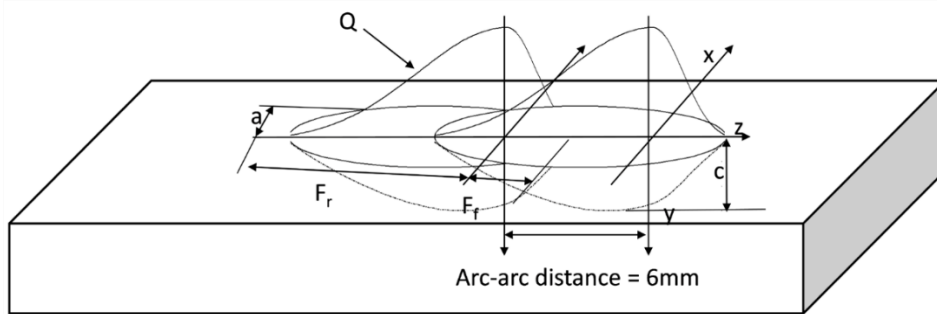


Figure 7.3. Schematic of double ellipsoidal heat source for twin-wire (arc-arc distance = 6mm).

7.2.2 Modeling of filler material and substrate

Earlier there were numerous attempts in 2D and 3D finite element analysis of welding process that only considered the heat input while ignoring the material addition (Lindgren 2006; Anca et al. 2011; Deng and Murakawa 2006). However, as the complete object is fabricated in a layer by layer manner in the weld-deposition based additive manufacturing, the amount of material added is considerable and cannot be neglected. Hence, quiet element method was adopted for factoring-in the material addition. In this method, during the analysis the stiffness and the thermal conductivity of deposition elements are assigned a very low value so that they do not disturb the rest of the model. Upon the instance of weld-deposition occurring in the process, they can be activated by assigning them the appropriate material properties.

In the current work, quiet element technique for which ANSYS has special feature called element death-and-birth functionality has been used to implement the same (ANSYS 2015). The value of thermal conductivity and stiffness of deactivated elements should be low so these may not have any contribution to the rest of the model but should not be as low that may produce an ill conditioned matrix. The elements belonging to a specific weld bead are reactivated by "element birth" option at the start of the respective weld bead or when they come under the influence of welding torch. The material properties of reactivated elements are reinstated at the time of their activation. The schematic representation of this process is shown in Figure 7. (a) and (b).

Typically, weld-deposition is carried out on a substrate rigidly clamped to a machine table. In this simulations, the substrate and the deposition are the deformable bodies using solid-70 3D element in ANSYS with the deposition being modeled using element death-and-birth functionality mentioned above. The clamped support to the substrate is enforced through 3D point to point contact element viz., Contac52 in ANSYS (ANSYS 2015). An additional set of coincident nodes are generated at the bottom of substrate to implement the same.

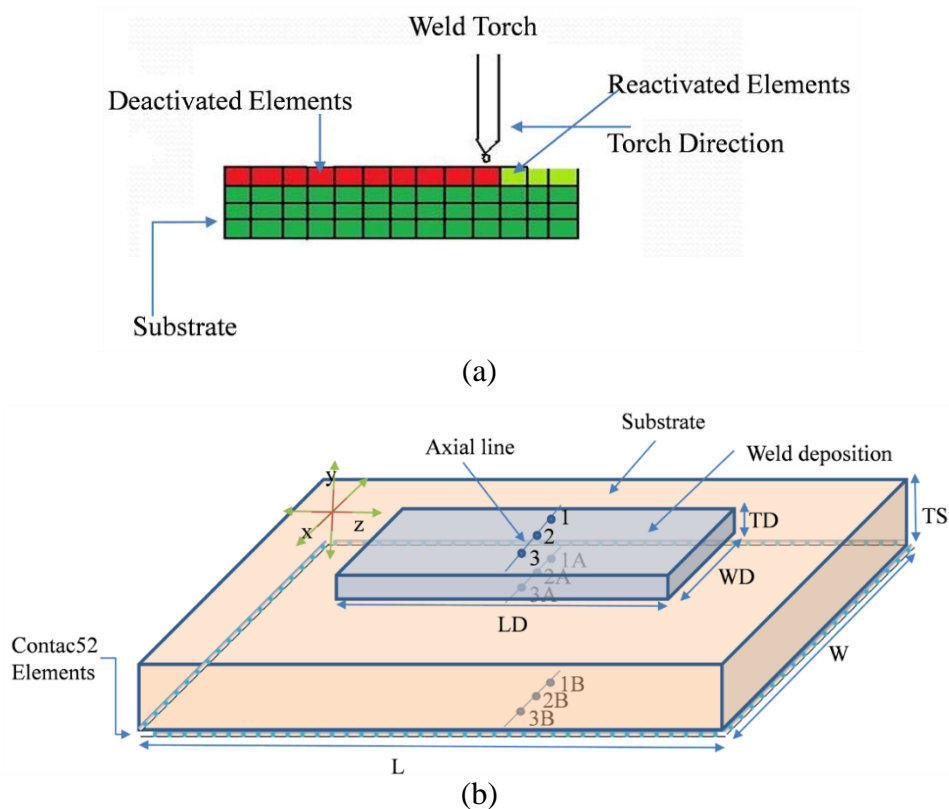


Figure 7.4. Schematic representation of (a) Filler material deposition (b) Geometry of weld and substrate analysed (Nodes 1, 2, 3, 1A, 2A, 3A, 1B, 2B & 3B used in pre-processing).

7.3 Modeling of twin-wire weld-deposition

The primary aim of the present work is to simulate the metal deposition using finite element method with specific application to AM using TWAM. The validity of the model depends on accurate prediction of temperature in the combined fusion zone

from the twin arcs. Among the superposition and the equivalent heat source models discussed earlier, the superposition approach is implemented in the current study, with the distance between the heat sources taken as 6 mm. The heat distribution obtained from the superposition of two double ellipsoidal heat sources is illustrated in Figure 7.5 (a). Figure 7.5 (b) represents the temperature profile over the substrate and deposit from the heat distribution is shown in Figure 7.5 (a).

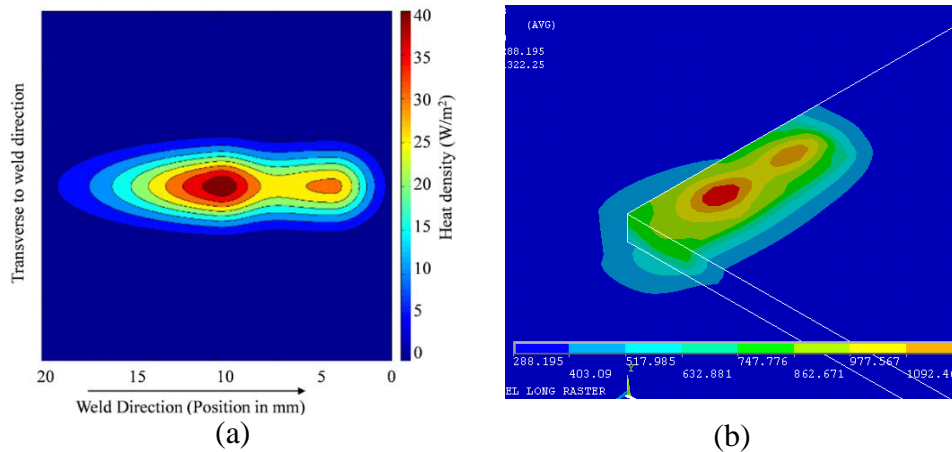


Figure 7.5. Twin-wire (a) heat density (b) temperature distribution at a given point.

The material of the filler wire and substrate plate used in experiments were ER70S-6 and C45 respectively, both belonging to the low-carbon steel family. The temperature dependent material properties for comparable class of material have been presented in Karlsson and Josefson (Karlsson and Josefson 1990; Hildenwall 1979; Sjoström 1982). These set of material properties have been used in literature, like Abid et al for instance, to predict residual stresses with ER70S-6 as the filler wire (Abid et al. 2005). Hence, the same material properties have been adopted in the present study (see Figure 7.6 (a) & Figure 7.6 (b))

At the beginning of the modelling, all the substrate and deposition elements are active. The elements belonging to weld-deposition are then deactivated using EKILL command. These dead elements are then gradually reactivated using EALIVE command at the relevant time step. Double ellipsoid heat equation discussed above is used to generate heat at the centroid of the each element which is activated. The time for heat generation at each element is calculated as follows:

$$t = \frac{\text{Length of deposition}}{\text{Torch Speed}} = \frac{LD}{S} \quad (7.10)$$

Where, t Time of heat generation, min
 LD Length of deposition, m
 S Speed of the weld-deposition torch, m/min

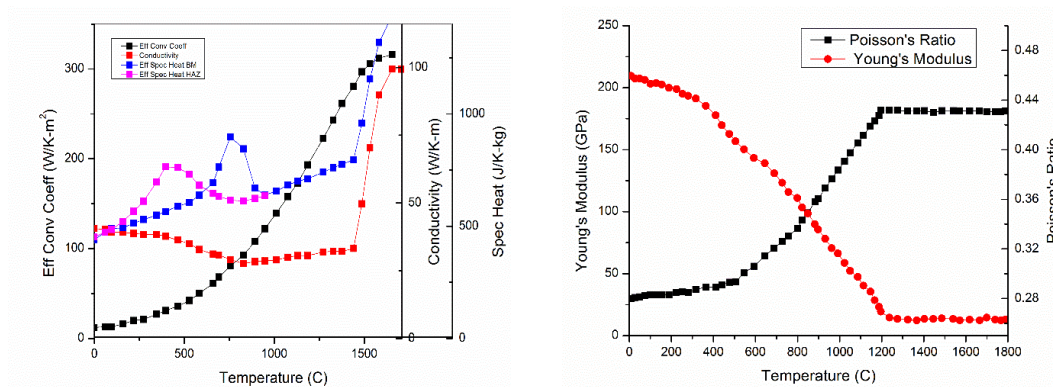


Figure 7.6. (a) Thermal material properties; (b) Structural material properties as a function of temperature (Karlsson and Josefson 1990).

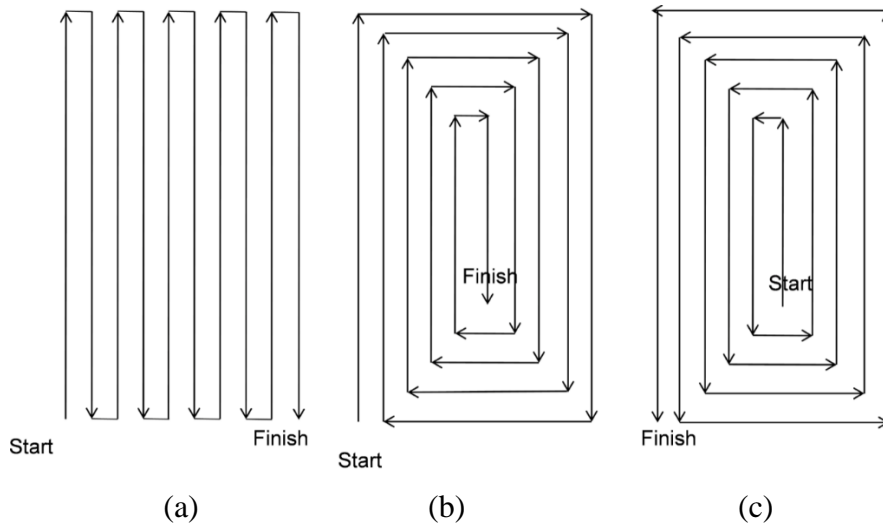


Figure 7.7. Three types of patterns used in weld-deposition (a) Raster (b) Spiral-in (c) Spiral-out.

The FEA modelling of the weld-deposition was done for different area-filling paths, viz., raster, spiral-in and spiral-out area-filling are as shown in Figure 7.7 (a)-(c)

respectively. The ANSYS parametric design language (APDL) was used to develop a subroutine for solving twin-wire weld-deposition problem for these different area-filling patterns. Passively coupled thermo-mechanical analysis as illustrated in Figure 7.8 was performed. The effect of thermal analysis on structural deformations is significant as compared to the heat distribution as a result of structural deformations. Hence, one-way passive coupling as illustrated in Figure 7.8 is adequate.

For the prediction of residual stresses induced during deposition, initially thermal analysis is carried out followed by the structural analysis. In thermal analysis, the temperature distribution is obtained at various stages of deposition considering the heat distribution from the moving heat source as the external source of loading. In the structural analysis, there is no external loading. However, the temperature distribution acts as body force and the only source of loading at each stage of deposition.

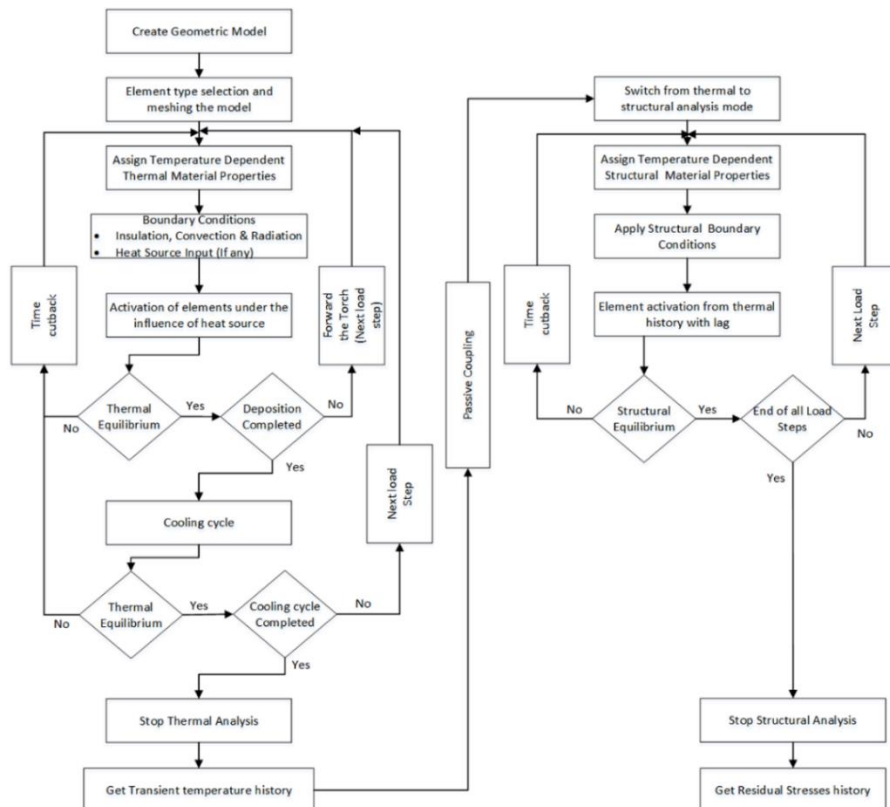


Figure 7.8. Detailed sequentially coupled thermo-mechanical ANSYS analysis.

The basic geometry of the model used comprises of a rigidly clamped rectangular substrate plate of dimensions 160x160x10 mm. Based on earlier experiments, the width and height of each weld-deposition pass was taken as 4.5mm, 1.8mm respectively. Length of each pass is 80 mm and the speed of the weld-deposition torch is 1.5m/min. A one-third overlap between each weld-deposition pass is considered (Suryakumar et al. 2011). The FEA model consists of 90000 3D Solid-70 elements. For saving computational time, the deposition area is fine meshed, while the rest of the substrate is coarsely meshed, as shown in Figure 7.9. The double ellipsoid heat source model discussed in the previous section (Eq. 7.6 & 7.7) is used for the analysis. The elements of the depositing passes are deactivated initially before the solution phase and activated gradually during the depositing process. The initial temperatures of all nodes are set at the ambient temperature 300K.

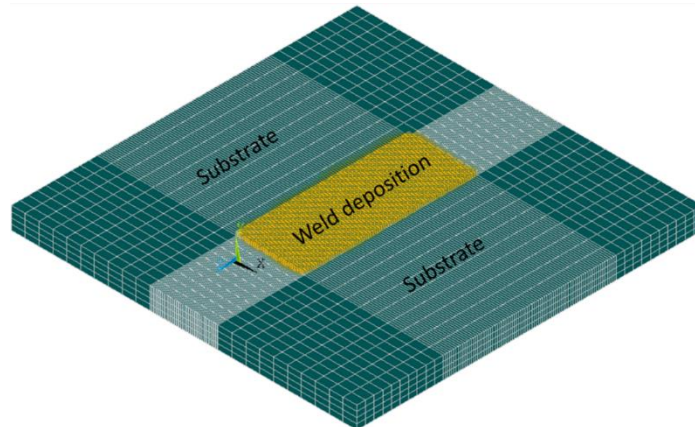


Figure 7.9. 3D finite element mesh.

The convergence and stability criterion for heat equation (1) under time marching scheme is ensured if the Courant number, C is less than 0.5, where C is defined as (Kalnay 2003):

$$C = \alpha \Delta t / \Delta x^2$$

Where, $\alpha = K / (C_p \rho)$ Thermal diffusivity

K Conductivity (W/m-K)

C_p Specific heat at constant pressure (J/kg-K)

ρ Density (Kg/m³)

Δt Time increment (s)

Δx Minimum size of the mesh (m)

In these simulations, Δx is 5×10^{-4} m. For a torch speed of 2.0 m/min, the corresponding Δt value will be 0.015 s. Based on these and the material thermal diffusivity (obtained from Figure 7.6 (a)), the Courant number, C will be 0.4758 which satisfies the convergence and stability criteria as mentioned above.

7.4 Validation of FEA Model

To validate the FE analysis presented above, multi-pass weld-deposition was carried on a C45 substrate plate with dimensions 160x160x10 mm and the residual stresses generated in the same was compared with that obtained from simulations. The fixture design for the same is shown in Figure 7.10. Design of fixture is important while conducting experiments: if the specimen is allowed to cool down without end constraints, the residual stress induced within the material will try to relieve in the form of warping of the substrate plate. However, in FE analysis, residual stresses are quantified rather than warping deformations. Hence, the clamped conditions in the experiments are maintained till the residual stresses are measured in the completely cooled condition, as explained in the subsequent part of this section.

The clamping of the substrate is done with the help of two center-cut square plates encompassing the edges of the substrate as shown in the Figure 7.10 (a). The substrate is sandwiched between these plates, along with heat insulation strips between them, to constraint and insulate the substrate respectively (Figure 7.10 (b)). The following are other considerations to be taken into account for the fixture design:

- Equal and uniform force should be exerted throughout the boundary of the plate.
- Proper clearance should be provided for the movement of the weld torch and for the movement of the XRD probe for residual stress measurement.
- Deposited area of the substrate plate and its bottom surface should not be in contact with any other material (i.e. heat loss is through convection & radiation only)
- The fixture should be able to withstand the force exerted due to the induced residual stress.

The experiments were conducted on substrate as shown in Figure 7.10 (b). The weld-deposition was carried out on an area of 80mm X 31.5mm at the center of the substrate plate with a step-over increment of 3mm between the passes. The process parameters used are listed in the Table 7.1 . Figure 7.11 (a) shows the fixture before deposition and Figure 7.11 (b) and (c) shows the top and bottom view of the substrate after deposition obtained using spiral-in pattern.

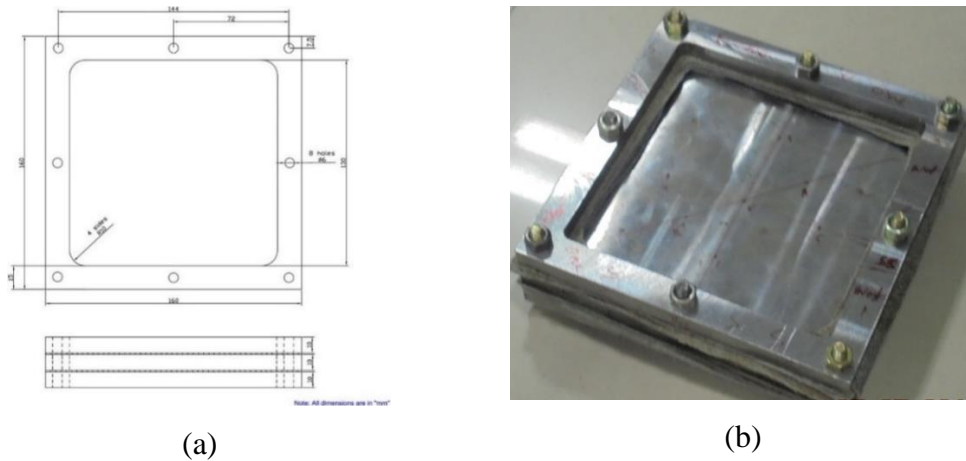


Figure 7.10. Fixture dimensions (a) two dimensional drawing (b) substrate fitted in fixture.

Table 7.1. Process Parameters used in experiments for validation.	
Parameters	Description
Current	112A
Inert gas	82% of Argon + 18% of CO ₂
Gap between two wires	6 mm
Gap between base to nozzle	16 mm
Filler material used	Copper coated mild steel wire (ER70S-6)
Filler wire diameter	1.2 mm
Weld torch speed	1.5 m/min
Percentage of overlap	$\frac{1}{3}rd$ of the weld bead width (i.e. 1.5mm)
Gas flow rate	12 lit/min

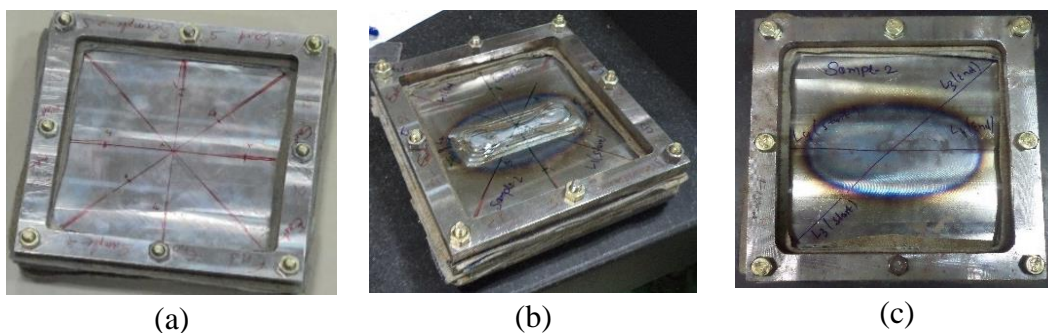


Figure 7.11. Setup used for spiral-in deposition pattern (a) Before weld-deposition (b) After weld-deposition: top view (c) After weld-deposition: bottom view.

Residual stresses were measured using pro-XRD residual stress measuring instrument (Proto Manufacturing and MP40P) shown in Figure 7.12. Residual stress was measured on top and bottom of substrate along diagonal and axial directions (represented by yellow and green lines respectively) as shown in Figure 7.13 (a)-(b). To obtain only the stresses developed during the process, measurements were done before and after the weld-deposition and the pre-weld stresses negated from the latter values. The beta angles range for the XRD measurement were kept in the range of -20° to 20° . Reading of residual stresses were taken at 8 points over each of the measurement profiles. The results of these experiments vis-à-vis FE analysis are presented in the subsequent section.

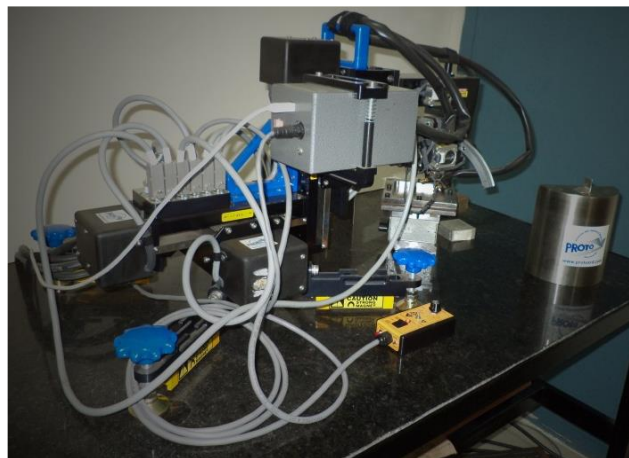


Figure 7.12. X-Ray Diffraction residual stress measurement setup.

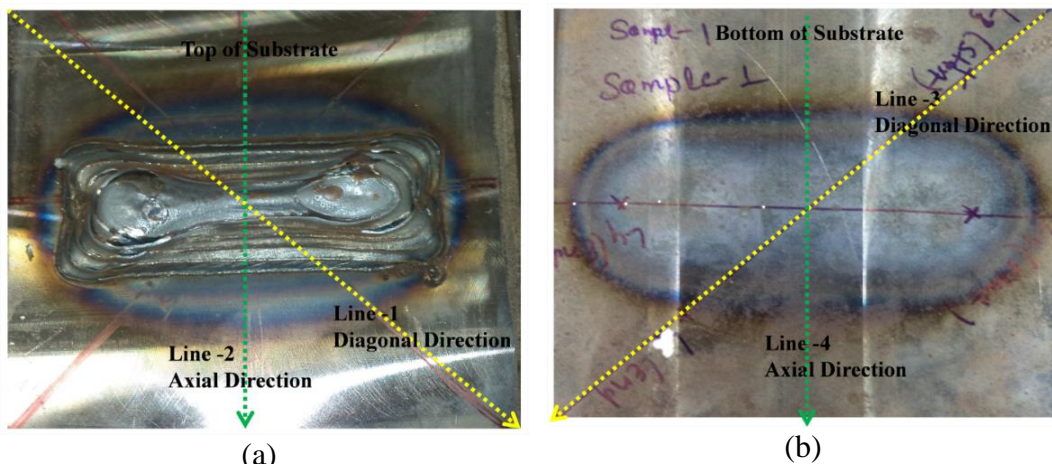


Figure 7.13. The profile for XRD measurements of residual stress (a) Top side (b) Bottom side of substrate (axial direction: green line; diagonal direction: yellow line).

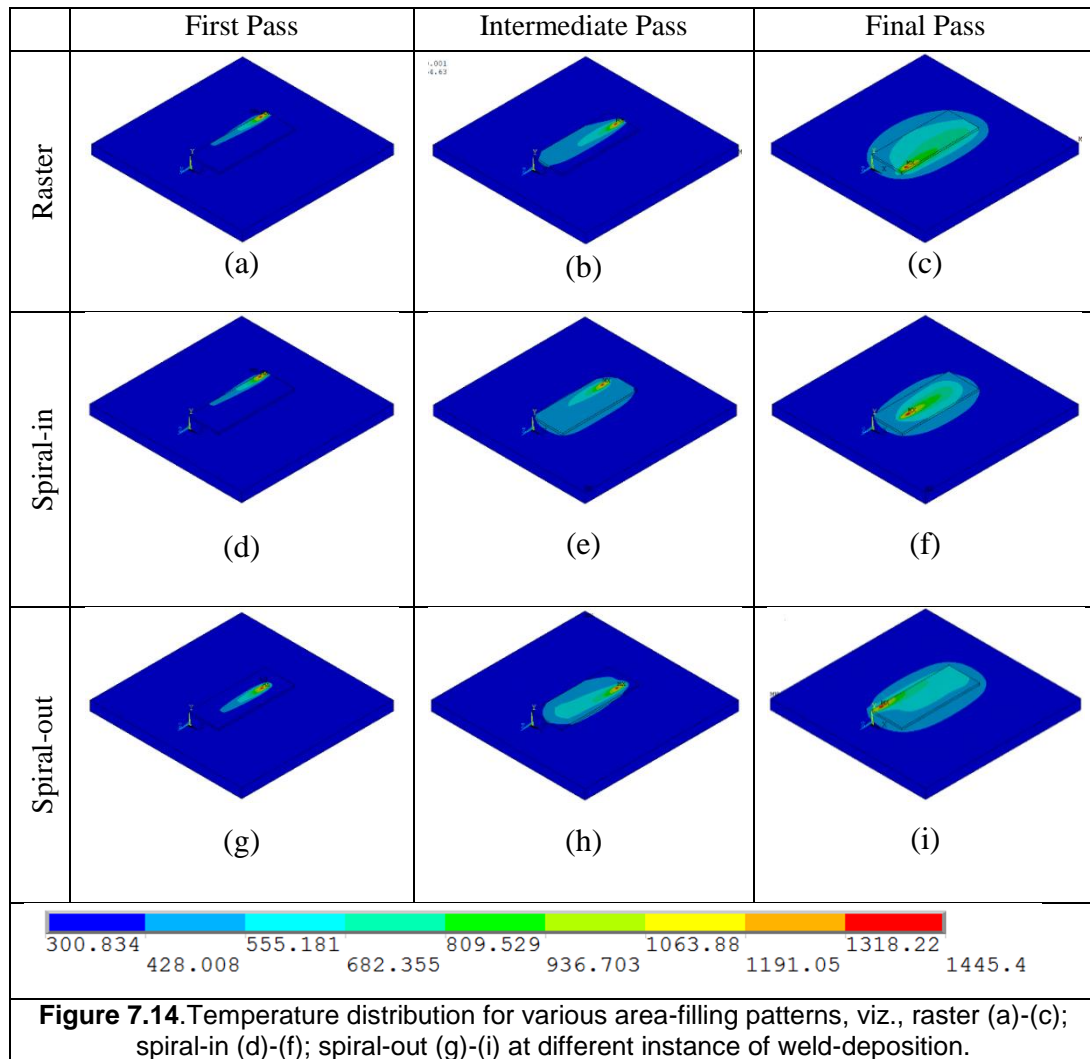
7.5 Results and discussion

In this section, the results for AM weld-deposition with various area-filling patterns from FE and experimental analysis are presented to gain insight into the role of fill pattern in the residual stress evolution. These results can be subdivided into two themes viz., thermal and structural as follows.

The temperature field distribution generated from the FE model for the weld-deposition over the substrate using a twin-wire moving heat source at various instances for raster, spiral-in and spiral-out are presented in Figure 7.14 (a)-(f). Even though the heat distribution for the twin-wire heat source is common for all the patterns, the activation sequence varies across different patterns. As a result, the temperature contours are different at different instance of deposition (as shown in Figure 7.14). However, the temperature profile at the end of final pass can be compared amongst the various patterns as it depicts the end of deposition (refer Figure 7.14 (c), (f) & (i)). Amongst these three, raster path shows a clear offset of temperature profile from the center of deposition, owing to the unidirectional propagation of the weld-passes. At the beginning of deposition due to lack of preheat conditions, the peak temperature increases rapidly from room temperature to around 800°C. Whereas, at later passes due to the assistance from preheat, peak temperature attains up to 1260°C without significant variation. However, the transition to peak temperature is a complex function dependent on pattern of deposition, conduction properties, time and position of weld- deposition under consideration and etc.

To gain more insight into the preheating and heat conduction from the earlier deposition, the time history of selected locations was analyzed subsequently. As marked in Figure 7.4 (b) nodes (1, 2 & 3) represent three locations along the axial line as shown in Figure 7.13. Nodes (1A, 2A, 3A) and (1B, 2B, 3B) correspond to the top and bottom of the substrate exactly below (1, 2, 3). The nodal temperature history for all the above 9 nodes are extracted. However, for brevity, the temperature history of nodes 2, 2A & 2B for the spiral-in pattern is presented in Figure 7.15 (a) as an

illustration. Figure 7.15 (b) plots the temperature mismatch between the deposition and the substrate at top and bottom respectively. The full activation history can provide a through insight into preheat. However, it is a heuristic task to obtain such a complete history. Hence, the focus has been restricted to these 9 nodes.



The temperature at node-2 is maintained at ambient temperature till it gets activated. In the Figure 7.15 (b), representing the spiral-in pattern, the activation of node-2 happens at $t=24s$ using element birth method (it also represents the end of deposition in all the three patterns). Once the node is activated by the acting of the twin-wire heat source, the temperature suddenly jumps to the fusion range. Subsequently, the deposited nodes and elements in its vicinity stays active and follows the heat transfer conditions. The temperature profile of the node-2A exhibits spiky fluctuations due to

the heat addition from the surrounding depositions and subsequent heat dispersion and dissipation due to conduction, convection and radiation. However, for the bottom surface (node-2B), the curve is much smoother compared to the top surface (node-2A) primarily due to remoteness from the fusion zone and secondly due to the predominant conduction.

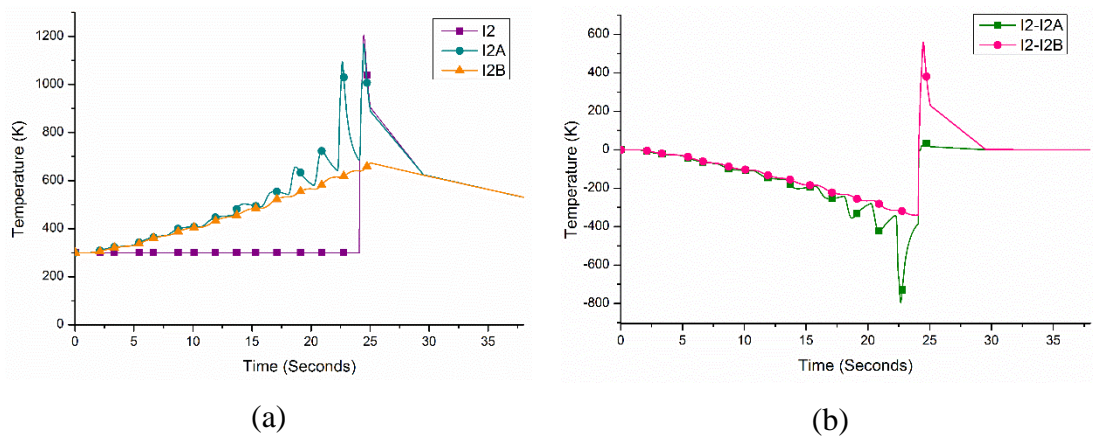


Figure 7.15. Temperature profile of spiral in pattern (a) Nodal temperature history (2, 2A, 2B); (b) Mismatch temperature between the deposition and the substrate (top (A) and bottom surface (B)).

Figure 7.15 (b) is a better representative to understand preheat before the activation and heat losses thereafter as compared to Figure 7.15 (a). In Figure 7.15 (b), the time at the peak represents the element activation time due to weld-deposition and the area under the left-side of the peak represents exclusively the preheat and right-side represents the heat losses thereafter. The area under the left-side of the curve is obtained to calculate the average mismatch in temperature of the substrate from deposition till the time of activation. This average mismatch temperature (hitherto referred as thermal mismatch) is the first-order metric to quantify preheat. However, different area-fill patterns leads to different activation times for the same node under consideration. A secant-mismatch temperature rate (hitherto referred as secant-rate) is also proposed to capture the lag as well as preheat gains and losses.

The temperature mismatch profile and the secant-mismatch temperature rate are obtained for the three area-fill patterns, viz., raster, spiral-in, spiral-out at all the 9 nodes mentioned earlier. These two metrics provide a foundation to compare results

across various area-fill patterns. Figure 7.16 (a)-(d) represents the average mismatch temperature at the top, bottom and the secant-mismatch temperature rate at the top and bottom surface of the substrate respectively. In the Figure 7.16 (a), the raster pattern exhibits a monotonically decreasing trend with the activation time. There is not much considerable decrease with the activation time and it stays constant around 100°C. However, in case of spiral patterns, there is a drastic increase in the average mismatch temperature with activation time. A low value of average mismatch temperature implies that preheat provides temperature of the range of fusion range, whereas, an increasing value implies considerably low substrate temperature from that of the fusion range. Hence, in Figure 7.16 (a), the raster pattern maintains a constant mismatch. The spiral patterns start with lower average mismatch at low activation times and drastically raise with increasing activation times. They also have a greater degree of variation across the activation times as compared to the raster. A similar behavior may be observed in the bottom surface (Figure 7.16 (b)) only differentiated by the reduced magnitude on account of comparatively high dispersion owing to the predominant role of conduction.

The trends in secant-rate as a function of activation times, can be broadly classified into the following three categories: A constant secant-rate implies a linear increase of preheat; a falling secant-rate implies reduction in preheat due to predominance of losses over heat gain as well as lag in the activation time; and vice versa. In Figure 7.16 (c), all the three patterns start with a high rate because of early activation. However, the decrease with the activation time implies the huge preheat losses resulting in mismatch between substrate temperatures at deposition from fusion range. Similarly, in Figure 7.16 (d), a similar behavior is observed with a reduced magnitude with the exception of spiral-out pattern which has a very low initial value. This may be attributed to the early exposure to activation thus leaving little time for heat transmission to the bottom of the substrate.

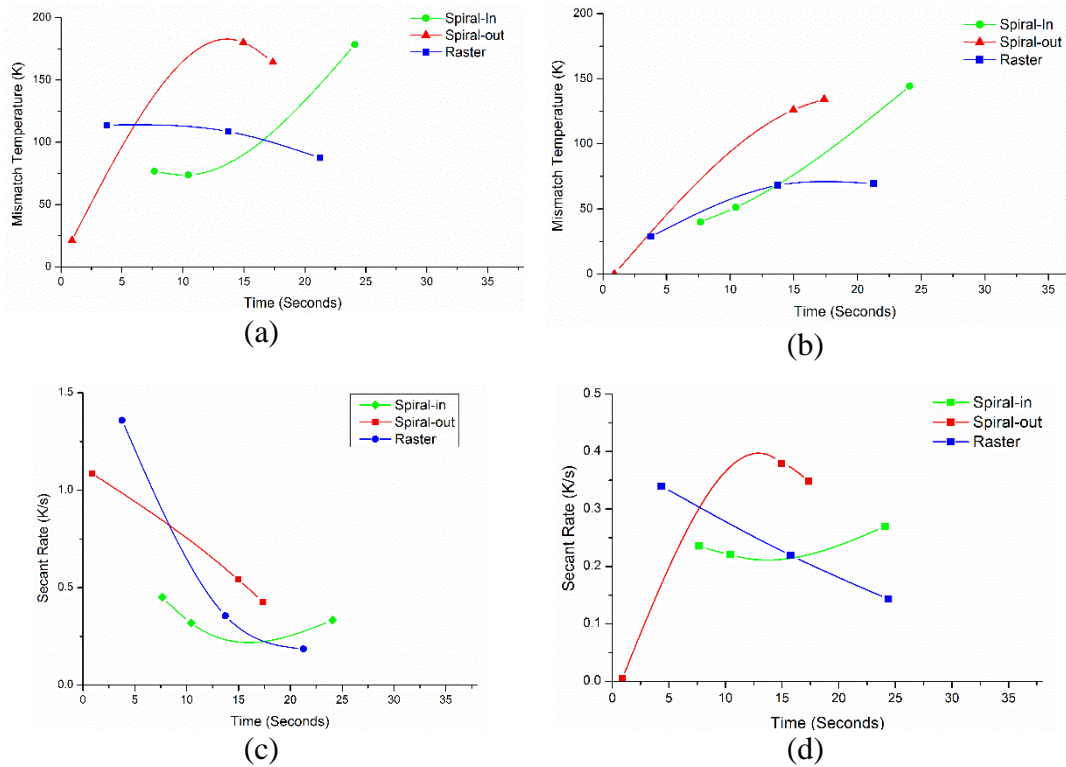
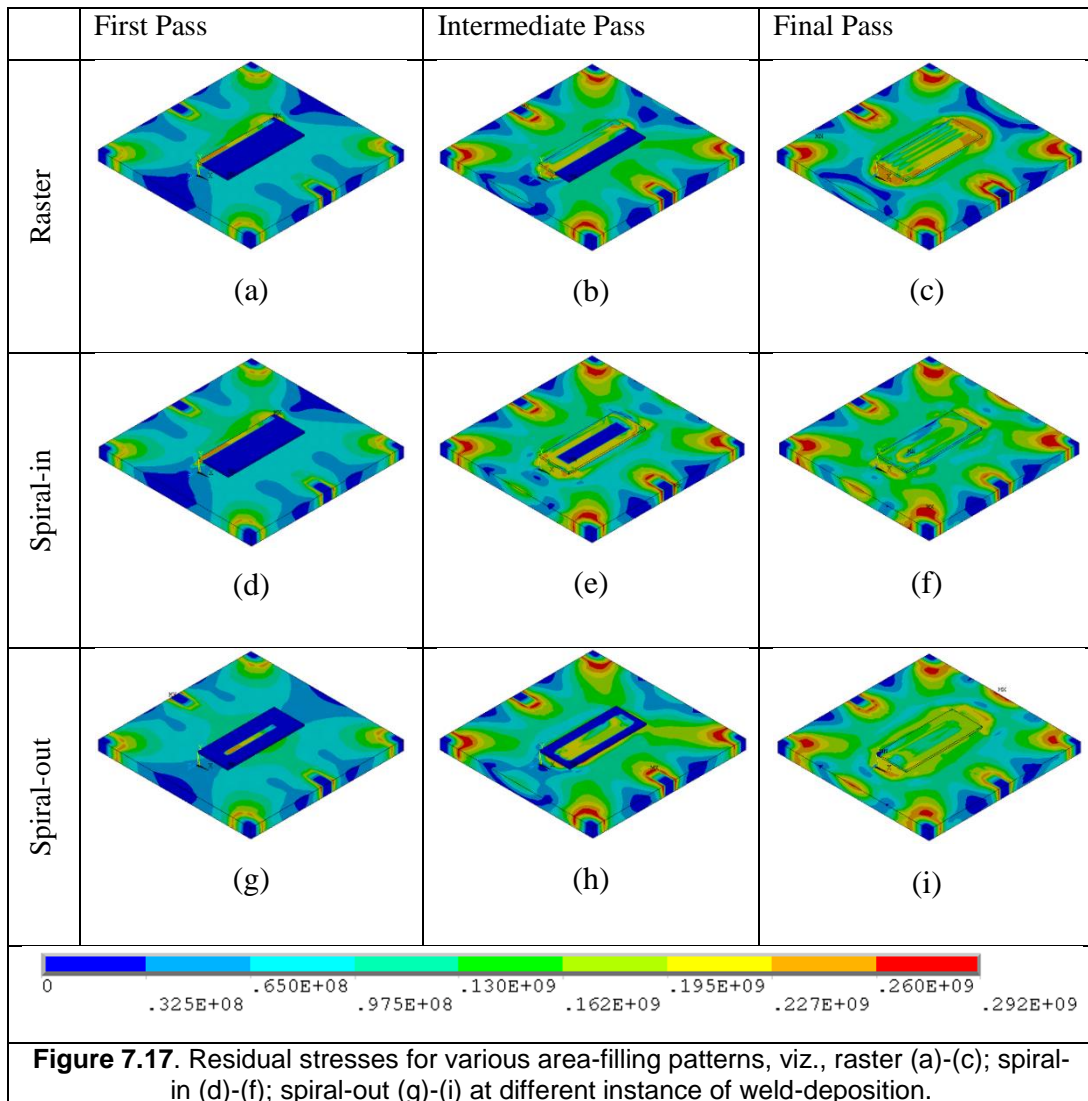


Figure 7.16. Average mismatch temperature at the (a) top and (b) bottom of substrate; Secant rate at the (c) top and (d) bottom of substrate.

Since the focus of simulations is on residual stresses, Von-Mises stress generated from the FE model for the weld-deposition over the substrate using a twin-wire moving heat source at various instances for raster, spiral-in and spiral-out and are presented in Figure 7.18 (a)-(f). Similar to the temperature distribution discussed earlier in Figure 7.14, the residual stresses at first and intermediate pass cannot be compared across different area patterns. However, the residual stresses at final pass as shown in Figure 7.18 (c), (f) & (i) can be compared as it represent an instance at the end of weld-deposition. Amongst these three, raster path Figure 7.18 (c) shows a clear concentration of residual stresses from the center of deposition, owing to the unidirectional propagation of the weld-passes. In all the three patterns the regions of high residual stress match with regions of high thermal gradations. In the structural simulations the substrate and deposit are loaded due to variation in the temperature distribution alone. Hence, it is evident that the temperature distribution plays a critical role in the evolution of the residual stresses during weld-deposition.



Further, to gain more insight into evolution of residual stress during different thermal loading phases such as preheating from the earlier deposition and heat conduction after activation, the time history of residual stresses at 9 selected locations (nodes shown in Figure 7.4 (b)) was analyzed subsequently. As discussed earlier, nodes (1, 2 & 3) represent three locations along the axial line, and the nodes (1A, 2A, & 3A) and (1B, 2B, & 3B) correspond to the top and bottom of the substrate exactly below (1, 2, & 3) respectively. For illustration purposes the residual stress history at nodes (2, 2A, & 2B) are presented for raster, spiral-in and spiral-out patterns in the Figure 7.18 (a-c) respectively. The temperature of the bottom surface are relatively cooler than the top of substrate surface as they are away from the fusion zone. The maximum temperature on the bottom side is of the order of 600-700K, while the top surface is

of the order of fusion range. Thus, the top surface is 3 times less stiff than the bottom surface (see Figure 7.6 (b)). With the end constraints to the components, the residual stress developed in the top of the substrate are less than the bottom, till deposition process is complete. As can be inferred from Figure 7.18 (a-c), at the later stages, i.e. during the cooling cycle, the bottom surface relaxes quickly as compared to the top surface. Consequence of which, there is change over in the order of residual stress on top and bottom of substrate.

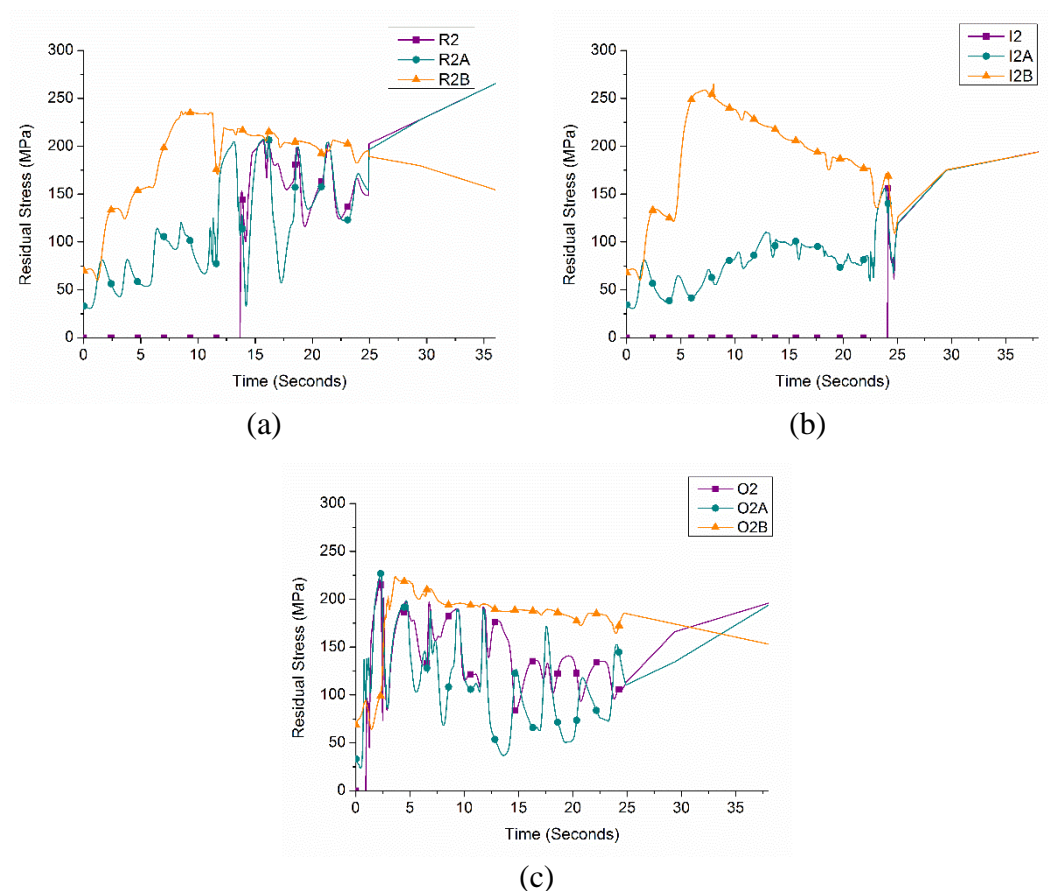


Figure 7.18. Residual stress history at Nodes (2, 2A, & 2B) for (a) Raster; (b) Spiral-in and (c) Spiral-out patterns.

The changeover of residual stresses of top and bottom of substrate is very significant in the raster pattern (see Figure 7.18 (a)), and intermediate in spiral-out pattern (see Figure 7.18 (c)). However, in the spiral-in pattern the top and bottom surfaces attains similar residual stresses (see Figure 7.18 (b)), but are substantially higher in value compared to that of raster pattern. Figure 7.19 (a)-(c) represents the bar charts of the residual stresses in the deposition at top and bottom of substrate at 9 selected locations

as discussed previously, for the raster, spiral-in and spiral-out pattern respectively. There is no significant difference in the residual stresses observed in the deposit and the top of the substrate at the end of cooling in all the three patterns (see Figure 7.19 (a-b)). However, at the bottom of the substrate the raster pattern exhibits very low residual stress over the two spiral patterns, as show in Figure 7.19 (c). Hence, the raster pattern stands out amongst other patterns in relaxing the residual stresses developed during the weld-deposition. In the rest, the spiral-in is less significant compared to spiral-out pattern in relaxing the residual stresses.

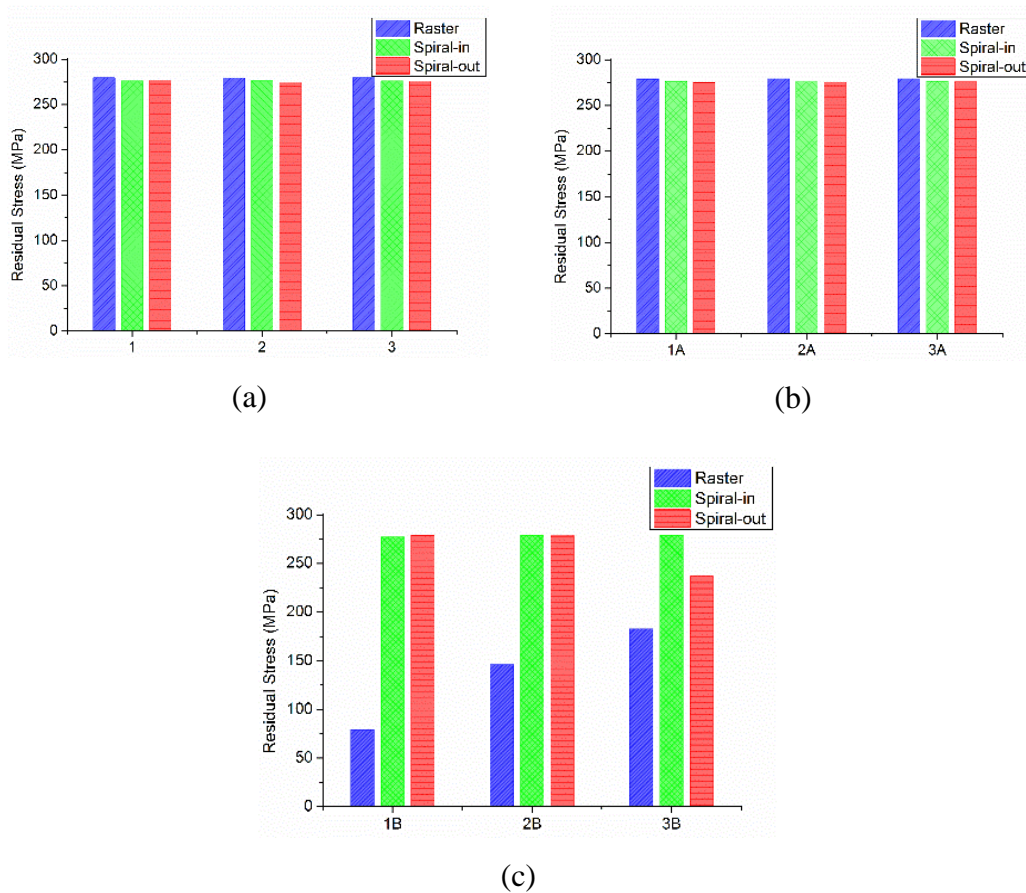
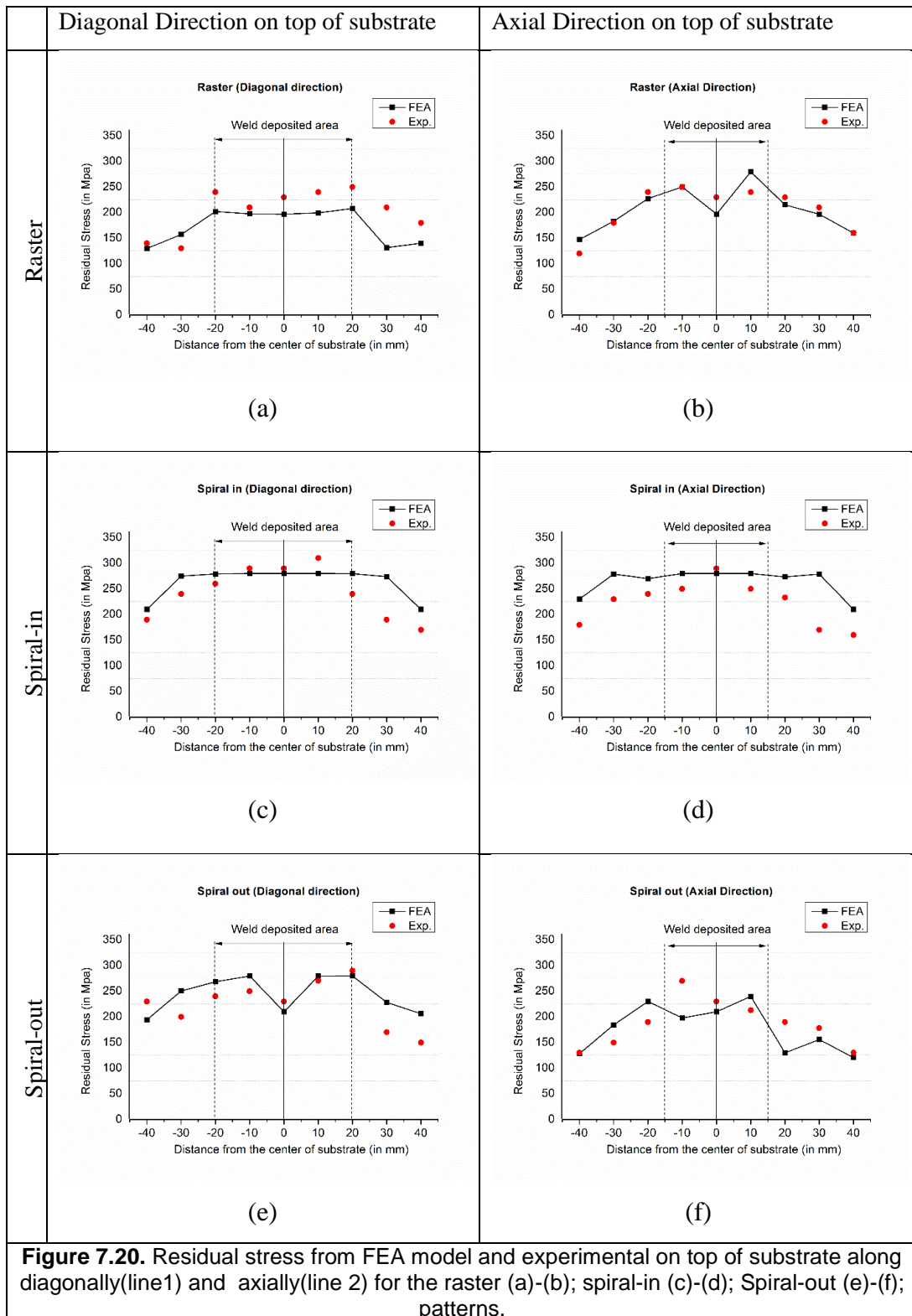


Figure 7.19. Residual stress at the end of cooling cycles at selected nodes on (a) The deposition (b) Top of Substrate (c) Bottom of substrate.

Residual stress with varying patterns is a complex problem as discussed earlier, the nodal residual stress evolution at selected nodes does not completely provide the variation in residual stress. Hence, the rest of this section, presents the distribution of residual stress over the two different profiles and their experimental validation.



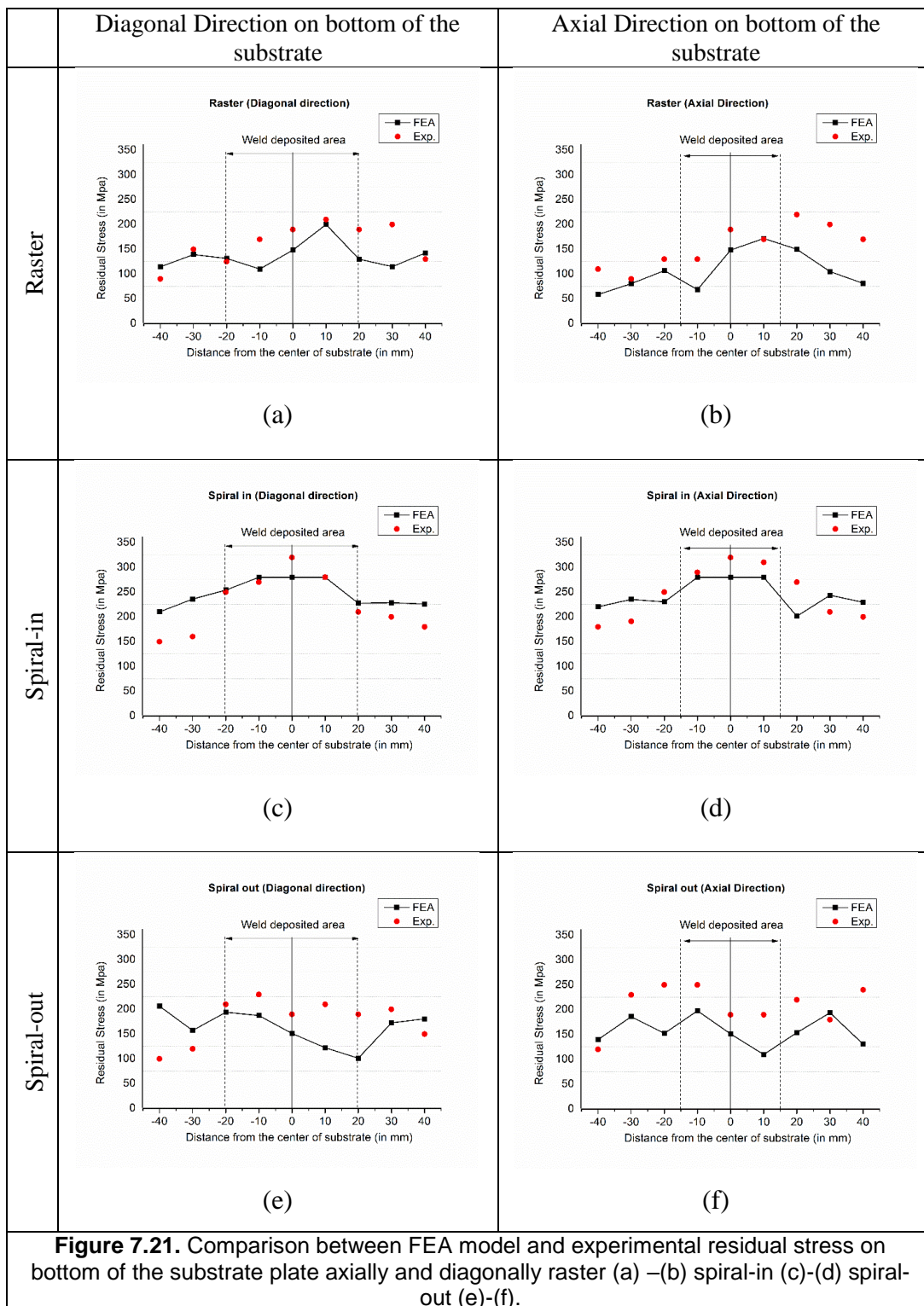
The residual stress values of the weld-deposited parts were obtained both from the FE simulations and experiments along two profile, viz., diagonally (line 1), axially (line

2) on top of substrate and bottom of the substrate (diagonally - line 3; axially- line 4) for all the three area patterns and are illustrated in the Figure 7.20 (a-f) & Figure 7.21 (a-f) respectively.

Figure 7.20 (a)-(b) illustrates the residual stress for raster pattern along the diagonal and axial on the top of the substrate, similarly Figure 7.20 (c)-(d) and Figure 7.20 (e)-(f) represents for the spiral-in and spiral-out patterns respectively. It is observed that in both diagonal and axial directions, the residual stress is lowest for the raster pattern, followed by the spiral-in and spiral-out. Although the total amount of heat input is same in all the three cases, the lower residual stress in raster case is due to lower mismatch temperature and secant-rates (see Figure 7.16) and subsequently quick relaxations (see Figure 7.19 (c)). This owes to the fact that amongst the three, the raster has minimal difference in the thermal mismatch pattern as the weld-deposition progresses.

Whereas, in the spiral paths, as a result of the circumferential nature of the path, the time lag between successive adjacent passes is continuously changing. Amongst the spiral-in and spiral-out patterns, the residual stresses are high in spiral-in because all the heat is accumulated inward as the weld progresses, whereas in spiral-out it is dispersed outward. This can be observed from the limited nodal histories plotted in the Figure 7.16 that the higher mismatch temperature are seen near the end of deposition in spiral-in pattern as compared to the spiral-out. Similar trend is observed in the residual stress distribution along the diagonal and axial directions on the bottom of the substrate (see Figure 7.21). However, the residual stresses on the bottom is less than the top of the substrate. The lower residual stresses are attributed to the lower mismatch temperature and secant-rate as shown in Figure 7.16.

In the Figure 7.20 & Figure 7.21, the black line represents the results obtained from the FE simulation, while the red dots are the corresponding data point obtained from XRD-experiments. On comparing the residual stresses from FE simulations and experiments it can be noted that the experimental values correlate with those from FE simulations only to the order and trend and not in accuracy of each point.



The main assumption in the current simulations as discussed earlier is that the residual stresses are majorly from the mismatch in the elastic properties due to thermal

gradation during the process of weld-deposition. Authors of this paper recommend that to capture the accurate values of the residual stresses, one has to perform a complete elasto-plastic analysis. However, as the focus of the current work is to understand the role of complex area-fill patterns on the residual stress evolution, rather than prediction of the residual stresses in itself, the work is restricted to elastic analysis. This also helps in maintaining the brevity by avoiding the convergence issues due to non-linearities in elasto-thermo-plastic analysis. This stands justified based on Figure 7.20 & Figure 7.21, where observed residual stresses are predominantly from the elastic part and the contributions from the plasticity is secondary in nature. These results presented from the elastic analysis itself give valuable insights into the evolution of residual stress from various area-fill patterns in AM.

7.6 Summary

A 3D finite element model was implemented to predict the residual stresses associated with multi-bead deposition of TWAM for different area-filling patterns viz., raster, spiral-in and spiral-out. Passively coupled thermo-mechanical FE analysis was carried out using ANSYS Mechanical APDL to obtain the temperature distributions and residual stresses on the deposit and the substrate. Residual stresses measured using X-ray diffraction were compared with those from the FE simulations. The key observations are as follows:

1. Temperature distribution plays a critical role in the evolution of the residual stresses during weld-deposition.
2. Temperature difference history between the deposit and top & bottom of substrate is obtained. Using this history two metrics were constructed:
 - a. Average thermal mismatch: to measure the net preheat
 - b. Secant-rate: to measure the lag and preheat gains/losses.
3. Amongst the three area-fill patterns, raster exhibited low thermal-mismatch and secant-rate owing to the unidirectional propagation of the weld-passes.
4. In all the area-fill patterns, temperature at the bottom of substrate is relatively lower than the top. This correlates with the low thermal mismatch and secant-

rate findings at the bottom of the substrate, as compared to top. They also exhibit faster cooling due to predominance of conduction.

5. Residual stresses from experiments are of the same order as those obtained from elastic-FE simulations, however, with a low accuracy of the prediction. Hence, these cannot be directly used for investigating the residual stresses developed. Nevertheless, for comparing the various area-fill patterns, these simulations can provide preliminary insights.
6. The residual stress developed at the top of the substrate are consistently lower than the bottom during the process of deposition for all the three patterns. However, after the completion of deposition a significant changeover in the order of residual stresses is observed.
7. Amongst the spiral-in and spiral-out patterns, the thermal-mismatch and residual stresses are high in spiral-in because the heat is accumulated inward as the weld progresses, whereas in spiral-out it is dispersed outward.
8. Raster pattern exhibited low residual stresses as compared to spiral patterns, owing to the lower thermal-mismatch and secant-rates. Hence, amongst the three area-fill patterns discussed, raster pattern stands out clearly and is recommended for TWAM applications.

As the analysis is carried out based on the heat distribution model, it fairly holds good for both the scenarios of similar and dissimilar filler wires being used in the process. The model is also capable of predicting the temperature gradient and thermally induced stress distribution resulting from weld-deposition. This can be useful in the selection of appropriate area-filling pattern for a given geometry ensuring lowest thermal stresses. The accuracy of the model can be further improved by adopting thermo-elasto-plastic structural analysis. Since, this will increase the computational time immensely, numerical approaches to the simplification of the FEA model may also have to be developed. This will also help in faster analysis for multiple layers.

Chapter 8

Conclusion and Future Scope

8.1 Conclusion

The driving force underlying this research is the opportunity that exists to design Twin-wire welding based additive manufacturing (TWAM) system for manufacturing of gradient objects, which tackle the need of various industrial applications. As such, the principle goal in this thesis is to design, manufacture, characterize and analyze a twin-wire weld-deposition process that provides a designer with the ability to specify the range of parameters, material gradient, morphology, structural and thermal properties for the product.

A detailed literature survey on the metallic AM processes has been presented. Amongst the laser, electron beam and arc based techniques for metallic AM, arc based processes have lower accuracy, but offer higher deposition rates along with low capital and operating costs. In the various AM processes for the manufacture of FGMs viz., laminated manufacturing, powder-bed and deposition techniques, localized and controlled material addition is possible only in the case of deposition techniques, making it ideally suited for fabrication of FGMs. Hence, the current work builds upon arc based deposition processes for realization of FGMs.

The above objective is achieved in the current work with the help of unique Twin-wire Welding based Additive Manufacturing (TWAM). A twin-wire setup comprising of two filler wires converging into a single torch has been used for the same. The use of dissimilar wires makes it possible to have a controlled weld-deposition of combination with varying material proportions. This weld-deposition torch is mounted on a robot interpolator for position control. The working principle of twin-wire weld-deposition process along with the individual attachments viz. welding torch, wire feeder and power source have been described. The robot programming syntax and methodology for simple movements and also for single and multi-bead deposition has also been described.

The experimental setup and its operational procedures provides the basis for the study of process parameters effecting the TWAM process. Two filler wires viz., ER70S-6 and ER110S-G, the former having lower hardness than the latter, were used for the experimentation. The operating range of the process parameters viz., current and torch speed for the three possible combinations of the filler wires have been determined and the feasible working region obtained from the same. Subsequently, the suitability of a parabolic profile model of the weld bead cross section has been studied and established. From this, it follows that the optimal step-over increment being two-third of the weld bead width. A second degree regression model for predicting weld bead width and height as a function of wire speed and torch speed was also obtained.

Criterion for adopting the twin-wire process from joining to metal deposition/cladding applications has also been studied. Although in dissimilar twin-wire welding, the leading and trailing may be different for forward and backward torch direction, it was found that the torch direction does not have any effect on the hardness of the weld-dead deposited. The number of overlap beads is observed to have an effect on the hardness with single beads having higher hardness than overlapping multiple beads. This is due to another phase of heating and partial-re-melting taking place when the next weld-deposition pass is made. Hardness variation in cross-section of weld bead along was measured. It was observed that there is variation in hardness between base plate and weld bead. However, there is less variation is occurred within the weld bead. Hence, hardness variation within bead is neglected. These preliminary studies on primary process parameters and secondary operating conditions will provide the basis for realising a gradient material matrix.

Subsequently, various experiments carried out to identify the suitable process parameters at a given location for a desired variation of hardness have been presented. These facilitate the fabrication of an actual FGM. It is found that the individual melting rate of the filler wires does not affect the hardness of the weld bead and it is only a function of the ratio of the amount of material of each deposited (and the wire speed).

Four types of sample parts were fabricated to demonstrate the concept of realizing FGMs through TWAM: (1) gradient in step-over direction: requires change in weld-deposition parameters across weld beads (2) gradient in weld-deposition direction: requires modification of process parameters for different sub-sections (3) gradient in both the X-Y directions: requires change in both 1&2 (4) gradient in X, Y and Z directions: demands variation to be carried across layers in addition to the earlier. The fabricated parts showed good match with the desired hardness values for a given location. Furthermore, to demonstrate the possible applications of TWAM, two illustrative examples were also fabricated.

Once the methodology for fabrication of FGMs has been established, characterization of objects fabricated through TWAM have been undertaken. Specimen made with five different combinations of filler wires (100%, 75%, 50%, 25%, 0% of filler wire ER70S-6 and vice versa of filler wire ER110S-G) were used for the analysis. These specimen were examined further by subjecting them to micro hardness, microstructural, X-Ray Fluorescence (XRF), Energy Dispersive X-ray analysis (EDAX) and X-Ray diffraction (XRD) analysis. In all these experiments, the properties were observed to be proportionate to the ratio of the respective filler wire ratios. This also correlates with the finding the earlier chapter where the hardness of the resultant weld bead assumed to be in the volumetric ratio of the filler wires used. This reinforces the hypothesis that the properties of the weld-deposited parts can be controlled in a localized manner by controlling the proportion of the filler wires.

Further on, the width of the transition region while switching over from one set of parameters to another was also investigated. This will help in assessing the best possible resolution of the gradient matrix possible. It was found that a minimum 8-11mm transition gap will can be encountered while moving from one parameter/functional value in the gradient matrix to another.

Modelling of the welding process is felt necessary to understand the evolution of the material properties and to better control the thermal and structural characteristics like

residual stresses resulting from the process. A 3D finite element model was implemented to predict the residual stresses associated with multi-bead deposition of TWAM for different area-filling patterns viz., raster, spiral-in and spiral-out. Passively coupled thermo-mechanical FE analysis was carried out using ANSYS Mechanical APDL to obtain the temperature distributions and residual stresses on the deposit and the substrate. Residual stresses measured using X-ray diffraction were compared with those from the FE simulations. Residual stresses from experiments are of the same order as those obtained from elastic-FE simulations, however, with a low accuracy of the prediction. Hence, these cannot be directly used for investigating the residual stresses developed. Nevertheless, for comparing the various area-fill patterns, these simulations can provide preliminary insights.

Amongst the spiral-in and spiral-out patterns, the residual stresses are high in spiral-in because the heat is accumulated inward as the weld progresses, whereas in spiral-out it is dispersed outward. Raster pattern exhibited low residual stresses as compared to spiral patterns, owing to the lower thermal-mismatch. Hence, amongst the three area-fill patterns discussed, raster pattern stands out clearly and is recommended for TWAM applications.

8.2 Significant Contributions

The following are some of the significant contributions emanating from the research:

- Setup of the TWAM process.
- Basic studies on the suitable set of filler materials and their operating range (in terms of wire and torch speeds).
- Study on effect of deposition alternatives like number of pre-heating passes, bead overlap, torch direction, vertical variation along cross section etc. on hardness.
- Predictive regression models for weld bead geometry and hardness.
- Experimental validation of the model along with their extension for gradient objects.
- Demonstration of the process by manufacture of 1D, 2D and 3D gradient objects.
- Characterization of the process through comparison of micro-hardness, XRD, XRF, microscopy data of five different combinations.

- Finite Element Modelling of twin-wire deposition process.
- Validation of the model by comparison of residual stresses for three area-filling paths.

8.3 Future scope

In the present work, the parameter study employs ER 70S-6 and ER110S-G combination as the filler wires. This makes a hardness range of approximately 200HV to 300HV possible. Examination of a wider set of filler wires could broaden this hardness range and thus the applications too. Relation to other mechanical properties like strength / toughness / wear can be explored.

The present work uses a *pixelated* form of gradient structure with a corresponding process parameters for each pixel to fabricate gradient objects. Future work on the can cover improving the resolution of the same, so that more gradual gradient can also be achieved. A deeper characterization analysis will also help in the same by throwing more light on the process physics.

Thermal management and residual stresses developed as a result of it are another concern in weld-deposited parts. Finite element modelling of the process to predict the residual stresses developed in the object will help in identification of optimize the parameters. The accuracy of the model can be further improved by adopting thermo-elasto-plastic structural analysis. Since, this will increase the computational time immensely, numerical approaches to the simplification of the FEA model may also have to be developed. This will also help in faster analysis for multiple layers.

References

- Abid, M, M Siddique, R A Mufti, Abid M and Nash D H, Abid M and Nash D H, Fukuoka T Takaki T, Bouzid A Derene M, et al. 2005. "Prediction of Welding Distortions and Residual Stresses in a Pipe-flange Joint Using the Finite Element Technique." *Modelling and Simulation in Materials Science and Engineering* 13 (3). IOP Publishing: 455–70. doi:10.1088/0965-0393/13/3/013.
- Adinarayanappa, Somashekara Makireddypalli, and Suryakumar Simhambhatla. 2014. "Determination of Process Parameter for Twin-Wire Weld-Deposition Based Additive Manufacturing." In *Volume 4: 19th Design for Manufacturing and the Life Cycle Conference; 8th International Conference on Micro- and Nanosystems*, V004T06A003. ASME. doi:10.1115/DETC2014-34658.
- Aiyiti, Wurikaixi, Wanhua Zhao, Bingheng Lu, and Yiping Tang. 2006. "Investigation of the Overlapping Parameters of MPAW-Based Rapid Prototyping." *Rapid Prototyping Journal* 12 (3): 165–72. doi:10.1108/13552540610670744.
- Akula, Sreenathbabu, and K.P. Karunakaran. 2006. "Hybrid Adaptive Layer Manufacturing: An Intelligent Art of Direct Metal Rapid Tooling Process." *Robotics and Computer-Integrated Manufacturing* 22 (2): 113–23. doi:10.1016/j.rcim.2005.02.006.
- Anca, Andrés, Alberto Cardona, José Risso, and Víctor D. Fachinotti. 2011. "Finite Element Modeling of Welding Processes." *Applied Mathematical Modelling* 35 (2): 688–707. doi:10.1016/j.apm.2010.07.026.
- ANSYS. 2015. "ANSYS Version 15. Mechanical APDL Theory Reference." *ANSYS Inc, Pennsylvania, US, 2015*.
- Arcam. 2015. "Arcam." <http://www.arcam.com/technology/electron-beam-melting/hardware/>.
- ASTM F2915. 2015. "ASTM F2915 - 12 Standard Specification for Additive Manufacturing File Format (AMF) Version 1.1 (Withdrawn 2013)." <http://www.astm.org/Standards/F2915.htm>.

- Bandyopadhyay, Amit, B. Krishna, Weichang Xue, and Susmita Bose. 2009. "Application of Laser Engineered Net Shaping (LENS) to Manufacture Porous and Functionally Graded Structures for Load Bearing Implants." *Journal of Materials Science: Materials in Medicine* 20 (0): 29–34. doi:10.1007/s10856-008-3478-2.
- Brickstad, B, and B L Josefson. 1998. "A Parametric Study of Residual Stresses in Multi-Pass Butt-Welded Stainless Steel Pipes." *International Journal of Pressure Vessels and Piping* 75 (1): 11–25. doi:10.1016/S0308-0161(97)00117-8.
- Cho, Dae-won, Woo-hyun Song, Min-hyun Cho, and Suck-joo Na. 2013. "Journal of Materials Processing Technology Analysis of Submerged Arc Welding Process by Three-Dimensional Computational Fluid Dynamics Simulations." *Journal of Materials Processing Tech.* 213 (12). Elsevier B.V.: 2278–91. doi:10.1016/j.jmatprotec.2013.06.017.
- Christiansen, N., V. Davies, and K. Gjermundsen. 1965. "Distribution of Temperatures in Arc Welding." *British Welding Journal* 12: 54–75.
- Chung, Haseung, and Suman Das. 2006. "Processing and Properties of Glass Bead Particulate-Filled Functionally Graded Nylon-11 Composites Produced by Selective Laser Sintering." *Materials Science and Engineering: A* 437 (2): 226–34. doi:10.1016/j.msea.2006.07.112.
- Deng, Dean, and Hidekazu Murakawa. 2006. "Numerical Simulation of Temperature Field and Residual Stress in Multi-Pass Welds in Stainless Steel Pipe and Comparison with Experimental Measurements." *Computational Materials Science* 37 (3): 269–77. doi:10.1016/j.commatsci.2005.07.007.
- Deng, Dean, Hidekazu Murakawa, and Wei Liang. 2008. "Numerical and Experimental Investigations on Welding Residual Stress in Multi-Pass Butt-Welded Austenitic Stainless Steel Pipe." *Computational Materials Science* 42 (2): 234–44. doi:10.1016/j.commatsci.2007.07.009.
- Digiacomio, G. 1969. "Residual Stresses in High-Strength Steel Weldments and Their Dimensional Stability during Welding and Stress Relieving." *Materials Science*

- and Engineering* 4 (May): 133–45. doi:10.1016/0025-5416(69)90053-6.
- Domack, M.S., and J.M. Baughman. 2005. “Development of Nickel-Titanium Graded Composition Components.” *Rapid Prototyping Journal* 11 (1): 41–51. doi:10.1108/13552540510573383.
- Feli, S., M. E. Aalami Aalegha, M. Foroutan, and E. Borzabadi Farahani. 2012. “Finite Element Simulation of Welding Sequences Effect on Residual Stresses in Multipass Butt-Welded Stainless Steel Pipes.” *Journal of Pressure Vessel Technology* 134 (1). American Society of Mechanical Engineers: 011209. doi:10.1115/1.4004571.
- Fessler, J, A Nickel, and G Link. 1997. “Functional Gradient Metallic Prototypes through Shape Deposition Manufacturing.” *Proceedings of the Solid Freeform Fabrication Symposium*, 521–28.
- Fronius. 2016. “Fronius USA LLC.” http://www.fronius.com/cps/rde/xchg/fronius_usa.
- Gery, D., H. Long, and P. Maropoulos. 2005. “Effects of Welding Speed, Energy Input and Heat Source Distribution on Temperature Variations in Butt Joint Welding.” *Journal of Materials Processing Technology* 167 (2-3): 393–401. doi:10.1016/j.jmatprotec.2005.06.018.
- Ghazvinloo, H R, and N Shadfar. 2010. “Effect of Arc Voltage , Welding Current and Welding Speed on Fatigue Life , Impact Energy and Bead Penetration of AA6061 Joints Produced by Robotic MIG Welding.” *Indian Journal of Science and Technology* 5356 (February): 156–62.
- Gibson, Ian, David W. Rosen, Brent Stucker, Ian Gibson, David W. Rosen, and Brent Stucker. 2010. “Development of Additive Manufacturing Technology.” In *Additive Manufacturing Technologies*, 17–39. Springer US.
- Goldak, John, Aditya Chakravarti, and Malcolm Bibby. 1984. “New Finite Element Model for Welding Heat Sources.” *Metallurgical Transactions. B, Process Metallurgy* 15 B (2): 299–305.
- Greasley, a., and S.G.W. Naylor. 1986. “Influence of Residual Welding Stresses on Fatigue Crack Growth under Compressive Loading.” *Engineering Fracture*

- Mechanics* 24 (5): 717–26. doi:10.1016/0013-7944(86)90244-4.
- Haseung, Chung, and Suman Das. 2008. “Functionally Graded Nylon-11/silica Nanocomposites Produced by Selective Laser Sintering.” *Materials Science and Engineering: A* 487 (1-2): 251–57. doi:10.1016/j.msea.2007.10.082.
- Hildenwall, B. 1979. “Prediction of the Residual Stresses Created during Quenching.” *Linkoping Studies in Science and Technology* Diss. No.: 39.
- Hinduja, Srichand, and Lin Li. 2013. “Laser Technology: Additive Manufacturing.” In *Proceedings of the 37th International MATADOR Conference*, edited by Srichand Hinduja and Lin Li, 337–91. Springer London.
- Hopkinson, Neil, Richard Hague, and Phill Dickens. 2006. “Introduction to Rapid Manufacturing.” In *Rapid Manufacturing*, edited by N. Hopkinson Lecturer, R. J. M. Hague Senior Lecturer, and P. M. Dickenson Director Associate Dean, 1–4. John Wiley & Sons, Ltd.
- Jandric, Z, M Labudovic, and R Kovacevic. 2004. “Effect of Heat Sink on Microstructure of Three-Dimensional Parts Built by Welding-Based Deposition.” *International Journal of Machine Tools and Manufacture* 44 (7-8): 785–96. doi:10.1016/j.ijmachtools.2004.01.009.
- Kalnay, Eugenia. 2003. *Atmospheric Modeling, Data Assimilation and Predictability*. Chapter-3, Cambridge university press.
- Karlsson, R. I., and B. L. Josefson. 1990. “Three-Dimensional Finite Element Analysis of Temperatures and Stresses in a Single-Pass Butt-Welded Pipe.” *Journal of Pressure Vessel Technology* 112 (1). American Society of Mechanical Engineers: 76.
<http://pressurevesseltech.asmedigitalcollection.asme.org/article.aspx?articleid=1456414>.
- Karunakaran, K. P., Alain Bernard, S. Suryakumar, Lucas Dembinski, and Georges Taillandier. 2012. “Rapid Manufacturing of Metallic Objects.” *Rapid Prototyping Journal* 18 (4): 264–80. doi:10.1108/13552541211231644.
- Karunakaran, K., S. Suryakumar, Vishal Pushpa, and Sreenathbabu Akula. 2009. “Retrofitment of a CNC Machine for Hybrid Layered Manufacturing.” *The*

- International Journal of Advanced Manufacturing Technology* 45 (7): 690–703.
doi:10.1007/s00170-009-2002-2.
- Karunakaran, K.P., S. Suryakumar, Vishal Pushpa, and Sreenathbabu Akula. 2010. “Low Cost Integration of Additive and Subtractive Processes for Hybrid Layered Manufacturing.” *Robotics and Computer-Integrated Manufacturing* 26 (5): 490–99. doi:10.1016/j.rcim.2010.03.008.
- Klingbeil, N. W., J. L. Beuth, R. K. Chin, and C. H. Amon. 2002. “Residual Stress-Induced Warping in Direct Metal Solid Freeform Fabrication.” *International Journal of Mechanical Sciences* 44 (1): 57–77. doi:10.1016/S0020-7403(01)00084-4.
- Klosterman, Donald, Richard Chartoff, George Graves, Nora Osborne, and Brian Priore. 1998. “Interfacial Characteristics of Composites Fabricated by Laminated Object Manufacturing.” *Composites Part A: Applied Science and Manufacturing* 29 (9-10): 1165–74. doi:10.1016/S1359-835X(98)00088-8.
- Kuka. 2016. “Kuka.” <http://www.kuka.com/>.
- Kumar, S. 2010. “Development of Functionally Graded Materials by Ultrasonic Consolidation.” *CIRP Journal of Manufacturing Science and Technology* 3 (1): 85–87. doi:10.1016/j.cirpj.2010.07.006.
- LAMP LAB. 2016. “Laser Aided Manufacturing Processes Laboratory.” <http://camt.mst.edu/research/facilities/laseraidedmanufacturingprocesseslaboratory/>.
- Lin, Y. C., and J. Y. Perng. 1997. “Effect of Welding Parameters on Residual Stress in Type 420 Martensitic Stainless Steel.” *Science and Technology of Welding and Joining* 138 (July): 22–27. doi:10.1179/136217197789815591.
- Lindgren, L.-E. 2006. “Numerical Modelling of Welding.” *Computer Methods in Applied Mechanics and Engineering* 195 (48-49): 6710–36. doi:10.1016/j.cma.2005.08.018.
- Liu, Weiping, and J.N. DuPont. 2003. “Fabrication of Functionally Graded TiC/Ti Composites by Laser Engineered Net Shaping.” *Scripta Materialia* 48 (9): 1337–42. doi:10.1016/S1359-6462(03)00020-4.

- Mazumder, J., D. Dutta, N. Kikuchi, and A. Ghosh. 2000. "Closed Loop Direct Metal Deposition: Art to Part." *Optics and Lasers in Engineering* 34 (4–6): 397–414. doi:10.1016/S0143-8166(00)00072-5.
- Meng, Q.G., H.Y. Fang, J.G. Yang, and S.D. Ji. 2005. "Analysis of Temperature and Stress Field in Al Alloy's Twin Wire Welding." *Theoretical and Applied Fracture Mechanics* 44 (2): 178–86. doi:10.1016/j.tafmec.2005.06.006.
- Merz, R, Prinz F B, Ramaswami K, Terk M, and Weiss L,E. 1994. "Shape Deposition Manufacturing." In *Proceedings of the Solid Freeform Fabrication Symposium*,. The University of Texas at Austin.
- Nakagawa, Takeo. 2000. "Advances in Prototype and Low Volume Sheet Forming and Tooling." *Journal of Materials Processing Technology* 98 (2): 244–50. doi:10.1016/S0924-0136(99)00205-8.
- Niino, Masayuki, Akio Suzuki, Toshio Hirai, Ryuzo Watanabe, Tohru Hirano, and Nobuhito Kuroishi. 1988. "Method of Producing a Functionally Gradient Material."
- Optomec. 2016. "Optomec." <http://www.optomec.com/>.
- Printers, 3D. 2015. "3D Printers, 3D Printing, 3D Parts and Rapid Prototyping | www.3dsystems.com." Accessed December 19. <http://www.3dsystems.com/>.
- Rosenthal D. 1946. "The Theory of Moving Sources of Heat and Its Application to Metal Treatments." *Trans ASME* 68: 849–69.
- Sandia National Lab. 2016. "Laser Engineered Net Shaping." 2016. Accessed January 1. <http://www.sandia.gov/mst/technologies/net-shaping.html>.
- Sharma, Abhay, Navneet Arora, and Bhanu K Mishra. 2008. "Mathematical Modeling of Flux Consumption during Twin-Wire Welding." *International Journal of Advanced Manufacturing Technology* 38 (11-12): 1114–24. doi:10.1007/s00170-007-1181-y.
- Sharma, Abhay, Ajay Kumar Chaudhary, Navneet Arora, and Bhanu K. Mishra. 2009. "Estimation of Heat Source Model Parameters for Twin-Wire Submerged Arc Welding." *The International Journal of Advanced Manufacturing Technology* 45

(11-12): 1096–1103. doi:10.1007/s00170-009-2046-3.

Sjostrom, S. 1982. “The Calculation of Quench Stresses in Steel.” *The Calculation of Quench Stresses in Steel* Diss. No.: 84.

Somashekara, Makireddypalli Adinarayanappa, and Simhambhatla Suryakumar. 2014. “Determination of Process Parameter for Twin-Wire Weld Deposition Based Additive Manufacturing.” In *Proceedings of the ASME 2014 International Design Engineering Technical Conferences & Computers and Information in Engineering Conference IDETC/CIE 2014 ,August 17-20*, 1–8. Buffalo, New York, USA: American Society of Mechanical Engineers.

Song, Yong-Ak, and Sehyung Park. 2006. “Experimental Investigations into Rapid Prototyping of Composites by Novel Hybrid Deposition Process.” *Journal of Materials Processing Technology* 171 (1): 35–40. doi:10.1016/j.jmatprotec.2005.06.062.

Song, Yong-Ak, Sehyung Park, and Soo-Won Chae. 2005. “3D Welding and Milling: Part II—optimization of the 3D Welding Process Using an Experimental Design Approach.” *International Journal of Machine Tools and Manufacture* 45 (9): 1063–69. doi:10.1016/j.ijmachtools.2004.11.022.

Song, Yong-Ak, Sehyung Park, Doosun Choi, and Haesung Jee. 2005. “3D Welding and Milling: Part I—a Direct Approach for Freeform Fabrication of Metallic Prototypes.” *International Journal of Machine Tools and Manufacture* 45 (9): 1057–62. doi:10.1016/j.ijmachtools.2004.11.021.

Spencer, J D, P M Dickens, and C M Wykes. 1998. “Rapid Prototyping of Metal Parts by Three-Dimensional Welding.” *Proceedings of the Institution of Mechanical Engineers, Part B: Journal of Engineering Manufacture* 212 (3): 175–82. doi:10.1243/0954405981515590.

Suryakumar, S., K.P. Karunakaran, Alain Bernard, U. Chandrasekhar, N. Raghavender, and Deepak Sharma. 2011. “Weld Bead Modeling and Process Optimization in Hybrid Layered Manufacturing.” *Computer-Aided Design* 43 (4): 331–44. doi:10.1016/j.cad.2011.01.006.

Taminger, Karen M., and Robert A. Hafley. 2006. “Electron Beam Freeform

- Fabrication for Cost Effective Near-Net Shape Manufacturing,” May.
- Teng, Tso Liang, Peng Hsiang Chang, and Wen Cheng Tseng. 2003. “Effect of Welding Sequences on Residual Stresses.” *Computers and Structures* 81 (5): 273–86. doi:10.1016/S0045-7949(02)00447-9.
- Thijs, Lore, Frederik Verhaeghe, Tom Craeghs, Jan Van Humbeeck, and Jean-Pierre Kruth. 2010. “A Study of the Microstructural Evolution during Selective Laser Melting of Ti–6Al–4V.” *Acta Materialia* 58 (9): 3303–12. doi:10.1016/j.actamat.2010.02.004.
- Tušek, J. 2004. “Mathematical Modelling of Melting Rate in Arc Welding with a Triple-Wire Electrode” 146: 415–23.
- Tušek, Janez. 2000. “Mathematical Modeling of Melting Rate in Twin-Wire Welding.” *Journal of Materials Processing Technology* 100 (1): 250–56. doi:10.1016/S0924-0136(99)00485-9.
- V. Pavelic, R. Tanbakuchi, O. A. Uyehara, and P. S. Myers. 1969. “Experimental and Computed Temperature Histories in Gas Tungsten Arc Welding of Thin Plates.” *Welding Journal Research Supplement* 48: 295s – 305s.
- Wang, Wei, and Xiaofeng Shang. 2009. “Functionally Gradient Material Laser Rapid Prototyping Technique.” *Tsinghua Science and Technology* 14 (S1). Tsinghua University Press: 192–99. doi:10.1016/S1007-0214(09)70091-4.
- Webster, G.a., and a.N. Ezeilo. 2001. “Residual Stress Distributions and Their Influence on Fatigue Lifetimes.” *International Journal of Fatigue* 23: 375–83. doi:10.1016/S0142-1123(01)00133-5.
- Wimpenny, D.I., B. Bryden, and I.R. Pashby. 2003. “Rapid Laminated Tooling.” *Journal of Materials Processing Technology* 138 (1-3): 214–18. doi:10.1016/S0924-0136(03)00074-8.
- Wohlers Associates. 2016. “Wohlers Associates.” <https://wohlersassociates.com/>.
- Xiong, Xinhong, Haiou Zhang, and Guilan Wang. 2009. “Metal Direct Prototyping by Using Hybrid Plasma Deposition and Milling.” *Journal of Materials Processing Technology* 209 (1): 124–30. doi:10.1016/j.jmatprotec.2008.01.059.

Zhang, Y, and Y K Chou. 2006. "Three-Dimensional Finite Element Analysis Simulations of the Fused Deposition Modelling Process." *Proceedings of the Institution of Mechanical Engineers, Part B: Journal of Engineering Manufacture* 220 (10): 1663–71. doi:10.1243/09544054JEM572.

Zhang, Yumin, Jiecai Han, Xinghong Zhang, Xiaodong He, Zhiqiang Li, and Shanyi Du. 2001. "Rapid Prototyping and Combustion Synthesis of TiC/Ni Functionally Gradient Materials." *Materials Science and Engineering: A* 299 (1–2): 218–24. doi:10.1016/S0921-5093(00)01377-0.

Publications based on This Thesis

Journal Publications

1. Suryakumar, Simhambhatla, K. P. Karunakaran, U. Chandrasekhar, and **M. A. Somashekara**. 2013. "A Study of the Mechanical Properties of Objects Built through Weld-deposition." Proceedings of the Institution of Mechanical Engineers, Part B: Journal of Engineering Manufacture 227 (8) (August 1): 1138–1147. doi:10.1177/0954405413482122.
2. **Somashekara M A** and Suryakumar S "Twin-wire Welding based Additive Manufacturing (TWAM): Manufacture of functionally gradient objects". (Recommended for publication with revision).
3. **Somashekara M A**, M Naveenkumar, Avinash K, C Viswanath and S Suryakumar "Investigations into effect of weld-deposition pattern on residual stress evolution for metallic additive manufacturing". (Recommended for publication with revision).
4. **Somashekara M A** and Suryakumar S "Preliminary study of welding of dissimilar materials in the additive manufacturing context". Under review.
5. **Somashekara M A** and Suryakumar S "Investigations into Functionally gradient objects deposited through Twin-wire Weld-deposition based Additive Manufacturing (TWAM)", in preparation for journal submission.
6. **Somashekara M A** and Suryakumar S "Study of microstructure and hardness gradient behavior in multi bead-deposition of Twin-wire Weld-deposition based Additive Manufacturing (TWAM)", in preparation for journal submission.

Conference Publications

1. **Somashekara M A** and Suryakumar S "Determination of Process Parameter for Twin-wire Weld-Deposition Based Additive Manufacturing., The ASME 2014 International Design and Engineering Technical Conferences & Computers and Information in Engineering Conference (IDETC/CIE 2014), August 17-20, 2014, The Buffalo Niagara Convention Center, Buffalo, New York.

2. **Somashekara M A** and Suryakumar S "Preliminary study of process parameters for weld-deposition using twin-wire system" An International Conference on 'Additive Manufacturing Technologies-AM 2013', October 7-8th, 2013, NIMHANS Convention Centre, Bangalore. INDIA. [**Third place in the best technical paper**].
3. Suryakumar S, and **Somashekara M A.**, "Manufacturing of Functionally Gradient Material by Using Weld-Deposition". Twenty Forth Annual International Solid Freeform Fabrication Symposium – An Additive Manufacturing Conference, August 12-14, 2013, The University of Texas, Austin, USA.
4. Suryakumar, S. and **Somashekara, M.A.** (2013): "Manufacturing of functionally gradient materials by using weld-deposition", IJS-JW 2013 (1st International Joint Symposium on Joining and Welding), November 6-8, Osaka University, Osaka, Japan.
5. **M A Somashekara** and S Suryakumar (2012) Manufacturing of Functionally Gradient Matrix through Weld-Deposition, Poster presentation at DST-JSPS Asian Academic Seminar 2012 Manufacturing, Design and innovation, December 3-8th, IIT Bombay, India.
6. **M A Somashekara** and S Suryakumar (2012) Manufacturing of Functionally Gradient Materials by Using Weld-Deposition, 1st International Conference on Thermo-Mechanically Graded Materials, pages 153-158, October 2012 Kassel, Germany. (Accepted).